THE ASTRONOMICAL JOURNAL, 172:139 (34pp), 2026 September https://doi.org/10.3847/1538-3881/ae7a4e

Characterizing Candidate Blazar Counterparts of the Ultra-high-energy Event KM3-230213A

O. Adriani[1,2], S. Aiello[3], A. Albert[4,5], A. R. Alhebsi[6], M. Alshamsi[7], S. Alves Garre[8], A. Ambrosone[9,10], F. Ameli[11], M. Andre[12], L. Aphecetche[13], M. Ardid[14], S. Ardid[14], J. Aublin[15], F. Badaracco[16,17], L. Bailly-Salins[18], Z. Bardačová[19,20], B. Baret[15], A. Bariego-Quintana[8], Y. Becherini[15], M. Bendahman[10], F. Benfenati Gualandi[21,22], M. Benhassi[10,23], M. Bennani[18], D. M. Benoit[24], E. Berbee[25], E. Berti[1], V. Bertin[7], P. Betti[1], S. Biagi[26], M. Boettcher[27], D. Bonanno[26], S. Bottai[1], A. B. Bouasla[28], J. Boumaaza[29], M. Bouta[7], M. Bouwhuis[25], C. Bozza[10,30], R. M. Bozza[9,10], H. Brânzaş[31], F. Bretaudeau[13], M. Breuhaus[7], R. Bruijn[25,32], J. Brunner[7], R. Bruno[3], E. Buis[25,33], R. Buompane[10,23], S. Buson[34,35], J. Busto[7], B. Caiffi[16], D. Calvo[8], A. Capone[11,36], F. Carenini[21,22], V. Carretero[25,32], T. Cartraud[15], P. Castaldi[22,37], V. Cecchini[8], S. Celli[11,36], L. Cerisy[7], M. Chabab[38], A. Chen[39], S. Cherubini[26,40], T. Chiarusi[22], M. Circella[41], R. Clark[42], R. Cocimano[26], J. A. B. Coelho[15], A. Coleiro[15], A. Condorelli[15], R. Coniglione[26], P. Coyle[7], A. Creusot[15], G. Cuttone[26], R. Dallier[13], A. De Benedittis[10], G. De Wasseige[42], V. Decoene[13], P. Deguire[7], I. Del Rosso[21,22], L. S. Di Mauro[26], I. Di Palma[11,36], A. F. Díaz[43], D. Diego-Tortosa[26], C. Distefano[26], A. Domi[44], C. Donzaud[15], D. Dornic[7], E. Drakopoulou[45], D. Drouhin[4,5], J.-G. Ducoin[7], P. Duverne[15], R. Dvornický[19], T. Eberl[44], E. Eckerová[19,20], A. Eddymaoui[29], T. van Eeden[25], M. Eff[15], D. van Eijk[25], I. El Bojaddaini[46], S. El Hedri[15], S. El Mentawi[7], V. Ellajosyula[16,17], A. Enzenhöfer[7], G. Ferrara[26,40], M. D. Filipović[47], F. Filippini[22], D. Franciotti[26], L. A. Fusco[10,30], T. Gal[44], J. García Méndez[14], A. Garcia Soto[8], C. Gatius Oliver[25], N. Geisselbrecht[44], E. Genton[42], H. Ghaddari[46], L. Gialanella[10,23], B. K. Gibson[24], E. Giorgio[26], I. Goos[15], P. Goswami[15], S. R. Gozzini[8], R. Gracia[44], C. Guidi[16,17], B. Guillon[18], M. Gutiérrez[48], C. Haack[44], H. van Haren[49], A. Heijboer[25], L. Hennig[44], J. J. Hernández-Rey[8], A. Idrissi[26], W. Idrissi Ibnsalih[10], G. Illuminati[22], O. Janik[44], D. Joly[7], M. de Jong[25,50], P. de Jong[25,32], B. J. Jung[25], P. Kalaczyński[51,52], G. Kalaitzidakis[53], J. Keegans[24], V. Kikvadze[54], G. Kistauri[54,55], C. Kopper[44], A. Kouchner[15,56], Yu. A. Kovalev[57,151], Y. Y. Kovalev[53], L. Krupa[20], V. Kueviakoe[25], V. Kulikovskiy[16], R. Kvatadze[55], M. Labalme[18], R. Lahmann[44], M. Lamoureux[42], G. Larosa[26], C. Lastoria[18], J. Lazar[42], A. Lazo[8], S. Le Stum[7], G. Lehaut[18], V. Lematre[42], E. Leonora[3], N. Lessing[8], G. Levi[21,22], M. Lincetto[35], M. Lindsey Clark[15], F. Longhitano[3], F. Magnani[7], J. Majumdar[25], L. Malerba[16,17], F. Mamedov[20], A. Manfreda[10], A. Manousakis[58], M. Marconi[16,17], A. Margiotta[21,22], A. Marinelli[9,10], C. Markou[45], L. Martin[13], M. Mastrodicasa[11,36], S. Mastroianni[10], J. Mauro[42], K. C. K. Mehta[52], A. Meskar[59], G. Miele[9,10], P. Migliozzi[10], E. Migneco[26], M. L. Mitsou[10,23], C. M. Mollo[10], L. Morales-Gallegos[10,23], N. Mori[1], A. Moussa[46], I. Mozun Mateo[18], R. Muller[22], M. R. Musone[10,23], M. Musumeci[26], S. Navas[48], A. Nayerhoda[41], C. A. Nicolau[11], B. Nkosi[39], B. Ó Fearraigh[16], V. Oliviero[9,10], A. Orlando[26], E. Oukacha[15], L. Pacini[1], D. Paesani[26], J. Palacios González[8], G. Papalashvili[41,54], P. Papini[1], V. Parisi[16,17], A. Parmar[18], E.J. Pastor Gomez[8], C. Pastore[41], A. M. Păun[31], G. E. Păvălaş[31], S. Peña Martínez[15], M. Perrin-Terrin[7], V. Pestel[18], R. Pestes[15], M. Petropavlova[20], L. Pfeiffer[35], P. Piattelli[26], A. Plavin[53,60], C. Poirè[10,30], V. Popa[31,152], T. Pradier[4], J. Prado[8], S. Pulvirenti[26], C.A. Quiroz-Rangel[14], N. Randazzo[3], A. Ratnani[61], S. Razzaque[62], I. C. Rea[10], D. Real[8], G. Riccobene[26], J. Robinson[27], A. Romanov[16,17,18], E. Ros[53], A. Šaina[8], F. Salesa Greus[8], D. F. E. Samtleben[25,50], A. Sánchez Losa[8], S. Sanfilippo[26], M. Sanguineti[16,17], D. Santonocito[26], P. Sapienza[26], M. Scaringella[1], M. Scarnera[15,42], J. Schnabel[44], J. Schumann[44], H. M. Schutte[27], J. Seneca[25], N. Sennan[46], P. A. Sevle Myhr[42], I. Sgura[41], R. Shanidze[54], A. Sharma[15], Y. Shitov[20], F. Šimkovic[19], A. Simonelli[10], A. Sinopoulou[3], B. Spisso[10], M. Spurio[21,22], O. Starodubtsev[1], D. Stavropoulos[45], I. Štekl[20], D. Stocco[13], M. Taiuti[16,17], G. Takadze[54], Y. Tayalati[29,61], H. Thiersen[27], S. Thoudam[6], I. Tosta e Melo[3,40], B. Trocmé[15], V. Tsourapis[45], S. V. Troitsky[57,63,151], E. Tzamariudaki[45], A. Ukleja[52,59], A. Vacheret[18], V. Valsecchi[26], V. Van Elewyck[15,56], G. Vannoye[7,16,17], E. Vannuccin[1], G. Vasileiadis[64], F. Vazquez de Sola[25], A. Veutro[11,36], S. Viola[26], D. Vivolo[10,23], A. van Vliet[6], E. de Wolf[25,32], I. Lhenry-Yvon[15], S. Zavatarelli[16], A. Zegarelli[11,36], D. Zito[26], J. D. Zornoza[8], J. Zúñiga[8], N. Zywucka[27]

KM3NeT Collaboration,

M. Lincetto[35], L. Pfeiffer[35], S. Buson[34,35], Jose Maria Sanchez Zaballa[35], A. Azzollini[35], A. Bremer[35]

MessMapp Group,

A. Acharyya[65], A. Adelfio[66], M. Ajello[67], L. Baldini[68], C. Bartolini[69,70], J. Becerra Gonzalez[71], R. Bellazzini[72], E. Bissaldi[69,73], R. D. Blandford[74], R. Bonino[75,76], P. Bruel[77], S. Buson[35], R. A. Cameron[74], R. Caputo[78], P. A. Caraveo[79], F. Casaburo[36,80,81], F. Casini[82], E. Cavazzuti[83], G. Chiaro[79], N. Cibrario[75,76], S. Ciprini[80,81], G. Cozzolongo[84,85], P. Cristarella Orestano[66,82], F. Cuna[69], S. Cutini[66], F. D'Ammando[86], D. Depalo[69], N. Di Lalla[74], A. Dinesh[87], L. Di Venere[69], A. Domínguez[87], S. J. Fegan[77], C. Fernández[88], A. Franckowiak[89], Y. Fukazawa[90], P. Fusco[69,73], F. Gargano[69], S. Garrappa[91], C. Gasbarra[80,92], D. Gasparrini[80,81], S. Germani[66,93], F. Giacchino[80,81], N. Giglietto[69,73], M. Giliberti[69,73], F. Giordano[69,73], M. Giroletti[86], I. A. Grenier[94], S. Guiriec[78,95], R. Gupta[78], M. Hashizume[90], E. Hays[78], J.W. Hewitt[96], A. Holzmann Airasca[69,70], D. Horan[77], X. Hou[97], T. Kayanoki[90], M. Kuss[72], S. Larsson[98,99], A. Laviron[77], T. Lewis[100], A. Liguori[69], J. Li[101,102], P. Loizzo[69,70], F. Longo[103,104], F. Loparco[69,73], L. Lorusso[69,73], M. N. Lovellette[105], P. Lubrano[66], S. Maldera[75], D. Malyshev[84], L. Marcotulli[67,106], G. Martí-Devesa[103], R. Martinelli[103,104], M. N. Mazziotta[69], I. Mereu[66,82],

M. Meyer[65], M. Michailidis[74], P. F. Michelson[74], T. Mizuno[107], P. Monti-Guarnieri[103,104], M. E. Monzani[74,108], A. Morselli[80], I. V. Moskalenko[74], M. Negro[109], N. Omodei[74], M. Orienti[86], E. Orlando[74,110], J. F. Ormes[111], D. Paneque[112], G. Panzarini[69,73], M. Persic[104,113], M. Pesce-Rollins[72], L. Pfeiffer[35], R. Pillera[69,73], T. A. Porter[74], G. Principe[86,103,104], J. L. Racusin[78], S. Rainò[69,73], R. Rando[114,115,116], B. Rani[78,117], S. Rani[118], M. Razzano[68], A. Reimer[119], O. Reimer[119], M. Rocamora Bernal[119], M. Sánchez-Conde[88,120], P. M. Saz Parkinson[121], D. Serini[69], C. Sgrò[72], V. Sharma[117,122,123], E. J. Siskind[124], P. Spinelli[69,73], D. J. Suson[125], H. Tajima[126,127], D. F. Torres[128,129], J. Valverde[78,117], P. Veres[89], K. Wood[130,153], G. Zaharijas[131], H. Zhang[78]

Fermi-LAT Collaboration,

A. C. S. Readhead[132], V. Pavlidou[133,134], J. A. Zensus[53], M.F. Aller[135], P. V. de la Parra[136], M. Hodges[132], T. Hovatta[137,138], S. Kiehlmann[134], I. Liodakis[134], W. Max-Moerbeck[139], B. Molina[136], T. J. Pearson[132], V. Ravi[132], R.A. Reeves[136], A. Synani[133,134], K. Tassis[133,134]

Owens Valley Radio Observatory 40-m Telescope Group,

and

A. Foisseau[15], A. Coleiro[15], F. Cangemi[15], D. Dornic[7], C. Lachaud[15], P. Maggi[140], D. Gotz[141], L. Xin[142], B. Cordier[141], O. Godet[143], A. Goldwurm[144], H. Goto[141], X. Han[142], N. Leroy[145], C. Plasse[141], Y. Qiu[142], J. Rodriguez[141], J. Wang[142], J. Wei[142]

SVOM Collaboration,

P. Baldini[146], J. Buchner[146], A. K. Erkenov[147,151], N. Globus[148], A. Merloni[146], A. Paggi[134], A. V. Popkov[57,149,151], D. Porquet[150], M. Salvato[146], Y. V. Sotnikova[57,147,151], and P. A. Voitsik[154]

[1] INFN, Sezione di Firenze, via Sansone 1, Sesto Fiorentino, 50019, Italy

[2] Università di Firenze, Dipartimento di Fisica e Astronomia, via Sansone 1, Sesto Fiorentino, 50019, Italy

[3] INFN, Sezione di Catania, (INFN-CT) Via Santa Sofia 64, Catania, 95123, Italy

[4] Université de Strasbourg, CNRS, IPHC UMR 7178, F-67000 Strasbourg, France

[5] Université de Haute Alsace, rue des Frères Lumière, 68093, Mulhouse Cedex, France

[6] Khalifa University of Science and Technology, Department of Physics, PO Box 127788, Abu Dhabi, UAE

[7] Aix Marseille Univ, CNRS/IN2P3, CPPM, Marseille, France

[8] IFIC—Instituto de Física Corpuscular (CSIC—Universitat de València), c/Catedrático José Beltrán, 2, 46980, Paterna, Valencia, Spain

[9] Università di Napoli "Federico II," Dip. Scienze Fisiche "E. Pancini," Complesso Universitario di Monte S. Angelo, Via Cintia ed. G, Napoli, 80126, Italy

[10] INFN, Sezione di Napoli, Complesso Universitario di Monte S. Angelo, Via Cintia ed. G, Napoli, 80126, Italy

[11] INFN, Sezione di Roma, Piazzale Aldo Moro 2, Roma, 00185, Italy

[12] Universitat Politècnica de Catalunya, Laboratori d'Aplicacions Bioacústiques, Centre Tecnològic de Vilanova i la Geltrú, Avda. Rambla Exposició, s/n, Vilanova i la Geltrú, 08800, Spain

[13] Subatech, IMT Atlantique, IN2P3-CNRS, Nantes Université, 4 rue Alfred Kastler - La Chantrerie, Nantes, BP 20722 44307, France

[14] Universitat Politècnica de València, Instituto de Investigación para la Gestión Integrada de las Zonas Costeras, C/ Paranimf, 1, Gandia, 46730, Spain

[15] Université Paris Cité, CNRS, Astroparticule et Cosmologie, F-75013 Paris, France

[16] INFN, Sezione di Genova, Via Dodecaneso 33, Genova, 16146, Italy

[17] Università di Genova, Via Dodecaneso 33, Genova, 16146, Italy

[18] LPC CAEN, Normandie Univ, ENSICAEN, UNICAEN, CNRS/IN2P3, 6 boulevard Maréchal Juin, Caen, 14050, France

[19] Comenius University in Bratislava, Department of Nuclear Physics and Biophysics, Mlynska dolina F1, Bratislava, 842 48, Slovak Republic

[20] Czech Technical University in Prague, Institute of Experimental and Applied Physics, Husova 240/5, Prague, 110 00, Czech Republic

[21] Università di Bologna, Dipartimento di Fisica e Astronomia, v.le C. Berti-Pichat, 6/2, Bologna, 40127, Italy

[22] INFN, Sezione di Bologna, v.le C. Berti-Pichat, 6/2, Bologna, 40127, Italy

[23] Università degli Studi della Campania "Luigi Vanvitelli," Dipartimento di Matematica e Fisica, viale Lincoln 5, Caserta, 81100, Italy

[24] E. A. Milne Centre for Astrophysics, University of Hull, Hull, HU6 7RX, UK

[25] Nikhef, National Institute for Subatomic Physics, PO Box 41882, Amsterdam, 1009 DB, The Netherlands

[26] INFN, Laboratori Nazionali del Sud, (LNS) Via S. Sofia 62, Catania, 95123, Italy

[27] North-West University, Centre for Space Research, Private Bag X6001, Potchefstroom, 2520, South Africa

[28] Université Badji Mokhtar, Département de Physique, Faculté des Sciences, Laboratoire de Physique des Rayonnements, B. P. 12, Annaba, 23000, Algeria

[29] University Mohammed V in Rabat, Faculty of Sciences, 4 av. Ibn Battouta, B.P. 1014, R.P. 10000 Rabat, Morocco

[30] Università di Salerno e INFN Gruppo Collegato di Salerno, Dipartimento di Fisica, Via Giovanni Paolo II 132, Fisciano, 84084, Italy

[31] Institute of Space Science—INFLPR Subsidiary, 409 Atomistilor Street, Magurele, Ilfov, 077125, Romania

[32] University of Amsterdam, Institute of Physics/IHEF, PO Box 94216, Amsterdam, 1090 GE, The Netherlands

[33] TNO, Technical Sciences, PO Box 155, Delft, 2600 AD, The Netherlands

[34] Deutsches Elektronen-Synchrotron DESY, Platanenallee 6, 15738 Zeuthen, Germany

[35] Julius-Maximilians-Universität Würzburg, Fakultät für Physik und Astronomie, Institut für Theoretische Physik und Astrophysik, Lehrstuhl für Astronomie, Emil-Fischer-Straße 31, 97074, Würzburg, Germany; massimiliano.lincetto@uni-wuerzburg.de, leonard.pfeiffer@uni-wuerzburg.de

[36] Università La Sapienza, Dipartimento di Fisica, Piazzale Aldo Moro 2, Roma, 00185, Italy

[37] Università di Bologna, Dipartimento di Ingegneria dell'Energia Elettrica e dell'Informazione "Guglielmo Marconi," Via dell'Università 50, Cesena, 47521, Italy

[38] Cadi Ayyad University, Physics Department, Faculty of Science Semlalia, Av. My Abdellah, P.O.B. 2390, Marrakech, 40000, Morocco

[39] University of the Witwatersrand, School of Physics, Private Bag 3, Johannesburg, Wits 2050, South Africa

[40] Università di Catania, Dipartimento di Fisica e Astronomia "Ettore Majorana," (INFN-CT) Via Santa Sofia 64, Catania, 95123, Italy

[41] INFN, Sezione di Bari, via Orabona, 4, Bari, 70125, Italy

[42] UCLouvain, Centre for Cosmology, Particle Physics and Phenomenology, Chemin du Cyclotron, 2, Louvain-la-Neuve, 1348, Belgium

[43] University of Granada, Department of Computer Engineering, Automation and Robotics/CITIC, 18071 Granada, Spain

[44] Friedrich-Alexander-Universität Erlangen-Nürnberg (FAU), Erlangen Centre for Astroparticle Physics, Nikolaus-Fiebiger-Straße 2, 91058 Erlangen, Germany

[45] NCSR Demokritos, Institute of Nuclear and Particle Physics, Ag. Paraskevi Attikis, Athens, 15310, Greece

[46] University Mohammed I, Faculty of Sciences, BV Mohammed VI, B.P. 717, R.P. 60000 Oujda, Morocco

[47] Western Sydney University, School of Computing, Engineering and Mathematics, Locked Bag 1797, Penrith, NSW 2751, Australia

[48] University of Granada, Dpto. de Física Teórica y del Cosmos & C.A.F.P.E., 18071 Granada, Spain

[49] NIOZ (Royal Netherlands Institute for Sea Research), PO Box 59, Den Burg, Texel, 1790 AB, The Netherlands

[50] Leiden University, Leiden Institute of Physics, PO Box 9504, Leiden, 2300 RA, The Netherlands

[51] AstroCeNT, Nicolaus Copernicus Astronomical Center, Polish Academy of Sciences, Rektorska 4, Warsaw, 00-614, Poland

[52] AGH University of Krakow, Al. Mickiewicza 30, 30-059 Krakow, Poland
[53] Max-Planck-Institut für Radioastronomie, Auf dem Hügel 69, 53121 Bonn, Germany; alexander@plav.in
[54] Tbilisi State University, Department of Physics, 3, Chavchavadze Ave., Tbilisi, 0179, Georgia
[55] The University of Georgia, Institute of Physics, Kostava str. 77, Tbilisi, 0171, Georgia
[56] Institut Universitaire de France, 1 rue Descartes, Paris, 75005, France
[57] Institute for Nuclear Research, Russian Academy of Sciences, 60th October Anniversary Prospect 7a, Moscow 117312, Russia
[58] University of Sharjah, Sharjah Academy for Astronomy, Space Sciences, and Technology, University Campus—POB 27272, Sharjah, UAE
[59] National Centre for Nuclear Research, 02-093 Warsaw, Poland
[60] Harvard University, Black Hole Initiative, 20 Garden Street, Cambridge, MA 02138, USA
[61] School of Applied and Engineering Physics, Mohammed VI Polytechnic University, Ben Guerir, 43150, Morocco
[62] University of Johannesburg, Department of Physics, PO Box 524, Auckland Park, 2006, South Africa
[63] Lomonosov Moscow State University, 1-2 Leninskie Gory, Moscow 119991, Russia
[64] Laboratoire Univers et Particules de Montpellier, Place Eugène Bataillon-CC 72, Montpellier Cédex 05, 34095, France
[65] Center for Cosmology and Particle Physics Phenomenology, University of Southern Denmark, Campusvej 55, DK-5230 Odense M, Denmark
[66] Istituto Nazionale di Fisica Nucleare, Sezione di Perugia, I-06123 Perugia, Italy
[67] Department of Physics and Astronomy, Clemson University, Kinard Lab of Physics, Clemson, SC 29634-0978, USA
[68] Università di Pisa and Istituto Nazionale di Fisica Nucleare, Sezione di Pisa I-56127 Pisa, Italy
[69] Istituto Nazionale di Fisica Nucleare, Sezione di Bari, I-70126 Bari, Italy
[70] Università degli studi di Trento, via Calepina 14, 38122 Trento, Italy
[71] Instituto de Astrofísica de Canarias and Universidad de La Laguna, Dpto. Astrofísica, 38200, La Laguna, Tenerife, Spain
[72] Istituto Nazionale di Fisica Nucleare, Sezione di Pisa, I-56127 Pisa, Italy
[73] Dipartimento di Fisica "M. Merlin" dell'Università e del Politecnico di Bari, via Amendola 173, I-70126 Bari, Italy
[74] W. W. Hansen Experimental Physics Laboratory, Kavli Institute for Particle Astrophysics and Cosmology, Department of Physics and SLAC National Accelerator Laboratory, Stanford University, Stanford, CA 94305, USA
[75] Istituto Nazionale di Fisica Nucleare, Sezione di Torino, I-10125 Torino, Italy
[76] Dipartimento di Fisica, Università degli Studi di Torino, I-10125 Torino, Italy
[77] Laboratoire Leprince-Ringuet, CNRS/IN2P3, École polytechnique, Institut Polytechnique de Paris, 91120 Palaiseau, France
[78] Astrophysics Science Division, NASA Goddard Space Flight Center, Greenbelt, MD 20771, USA
[79] INAF——Istituto di Astrofisica Spaziale e Fisica Cosmica Milano, via E. Bassini 15, I-20133 Milano, Italy
[80] Istituto Nazionale di Fisica Nucleare, Sezione di Roma "Tor Vergata," I-00133 Roma, Italy
[81] Space Science Data Center——Agenzia Spaziale Italiana, Via del Politecnico, snc, I-00133, Roma, Italy
[82] Dipartimento di Fisica, Università degli Studi di Perugia, I-06123 Perugia, Italy
[83] Italian Space Agency, Via del Politecnico snc, 00133 Roma, Italy
[84] Friedrich-Alexander Universität Erlangen-Nürnberg, Erlangen Centre for Astroparticle Physics, Erwin-Rommel-Str. 1, 91058 Erlangen, Germany
[85] Friedrich-Alexander-Universität, Erlangen-Nürnberg, Schlossplatz 4, 91054 Erlangen, Germany
[86] INAF Istituto di Radioastronomia, I-40129 Bologna, Italy
[87] Grupo de Altas Energías, Universidad Complutense de Madrid, E-28040 Madrid, Spain
[88] Instituto de Física Teórica UAM/CSIC, Universidad Autónoma de Madrid, E-28049 Madrid, Spain
[89] Ruhr University Bochum, Faculty of Physics and Astronomy, Astronomical Institute (AIRUB), 44780 Bochum, Germany
[90] Department of Physical Sciences, Hiroshima University, Higashi-Hiroshima, Hiroshima 739-8526, Japan
[91] Department of Particle Physics and Astrophysics, Weizmann Institute of Science, 76100 Rehovot, Israel
[92] Dipartimento di Fisica, Università di Roma "Tor Vergata," I-00133 Roma, Italy
[93] Dipartimento di Fisica e Geologia, Università degli Studi di Perugia, via Pascoli snc, I-06123 Perugia, Italy
[94] Université Paris Cité, Université Paris-Saclay, CEA, CNRS, AIM, F-91191 Gif-sur-Yvette, France
[95] The George Washington University, Department of Physics, 725 21st Street, NW, WA, DC 20052, USA
[96] University of North Florida, Department of Physics, 1 UNF Drive, Jacksonville, FL 32224, USA
[97] Yunnan Observatories, Chinese Academy of Sciences, Kunming 650216, People's Republic of China
[98] Department of Physics, KTH Royal Institute of Technology, AlbaNova, SE-106 91 Stockholm, Sweden
[99] The Oskar Klein Centre for Cosmoparticle Physics, AlbaNova, SE-106 91 Stockholm, Sweden
[100] Department of Physics & Earth, Planetary, and Space Science Institute, Michigan Technological University, Houghton, MI 49931, USA
[101] Department of Astronomy, University of Science and Technology of China, Hefei 230026, People's Republic of China
[102] School of Astronomy and Space Science, University of Science and Technology of China, Hefei 230026, People's Republic of China
[103] Dipartimento di Fisica, Università di Trieste, I-34127 Trieste, Italy
[104] Istituto Nazionale di Fisica Nucleare, Sezione di Trieste, I-34127 Trieste, Italy
[105] The Aerospace Corporation, 14745 Lee Rd, Chantilly, VA 20151, USA
[106] Department of Astronomy, Department of Physics and Yale Center for Astronomy and Astrophysics, Yale University, New Haven, CT 06520-8120, USA
[107] Hiroshima Astrophysical Science Center, Hiroshima University, Higashi-Hiroshima, Hiroshima 739-8526, Japan
[108] Vatican Observatory, Castel Gandolfo, V-00120, Vatican City State
[109] Department of Physics and Astronomy, Louisiana State University, Baton Rouge, LA 70803, USA
[110] Istituto Nazionale di Fisica Nucleare, Sezione di Trieste, and Università di Trieste, I-34127 Trieste, Italy
[111] Department of Physics and Astronomy, University of Denver, Denver, CO 80208, USA
[112] Max-Planck-Institut für Physik, D-80805 München, Germany
[113] INAF-Astronomical Observatory of Padova, Vicolo dell'Osservatorio 5, I-35122 Padova, Italy
[114] Dipartimento di Fisica e Astronomia "G. Galilei," Università di Padova, Via F. Marzolo, 8, I-35131 Padova, Italy
[115] Istituto Nazionale di Fisica Nucleare, Sezione di Padova, I-35131 Padova, Italy
[116] Center for Space Studies and Activities "G. Colombo," University of Padova, Via Venezia 15, I-35131 Padova, Italy
[117] Center for Space Science and Technology, University of Maryland Baltimore County, 1000 Hilltop Circle, Baltimore, MD 21250, USA
[118] Michigan Technological University, 1400 Townsend Drive, Houghton, MI 49931, USA
[119] Institut für Astro- und Teilchenphysik, Leopold-Franzens-Universität Innsbruck, A-6020 Innsbruck, Austria
[120] Departamento de Física Teórica, Universidad Autónoma de Madrid, 28049 Madrid, Spain
[121] Santa Cruz Institute for Particle Physics, Department of Physics and Department of Astronomy and Astrophysics, University of California at Santa Cruz, Santa Cruz, CA 95064, USA
[122] Astrophysics Science Division, NASA Goddard Space Flight Center, Mail Code 661, Greenbelt, MD 20771, USA
[123] Center for Research and Exploration in Space Science and Technology, NASA/GSFC, Greenbelt, MD 20771, USA
[124] NYCB Real-Time Computing Inc., Lattingtown, NY 11560-1025, USA
[125] Purdue University Northwest, Hammond, IN 46323, USA

[126] Nagoya University, Institute for Space-Earth Environmental Research, Furo-cho, Chikusa-ku, Nagoya 464-8601, Japan
[127] Kobayashi-Maskawa Institute for the Origin of Particles and the Universe, Nagoya University, Furo-cho, Chikusa-ku, Nagoya, Japan
[128] Institute of Space Sciences (ICE, CSIC), Campus UAB, Carrer de Magrans s/n, E-08193 Barcelona, Spain; and Institut d'Estudis Espacials de Catalunya (IEEC), E-08034 Barcelona, Spain
[129] Institució Catalana de Recerca i Estudis Avançats (ICREA), E-08010 Barcelona, Spain
[130] Praxis Inc., Alexandria, VA 22303, resident at Naval Research Laboratory, WA, DC 20375, USA
[131] Center for Astrophysics and Cosmology, University of Nova Gorica, Nova Gorica, Slovenia
[132] Owens Valley Radio Observatory, California Institute of Technology, Pasadena, CA 91125, USA
[133] Department of Physics and Institute of Theoretical and Computational Physics, University of Crete, 71003 Heraklion, Greece
[134] Institute of Astrophysics, Foundation for Research and Technology-Hellas, GR-71110 Heraklion, Greece
[135] Department of Astronomy, University of Michigan, 323 West Hall, 1085 S. University Avenue, Ann Arbor, MI 48109, USA
[136] CePIA, Astronomy Department, Universidad de Concepción, Casilla 160-C, Concepción, Chile
[137] Finnish Centre for Astronomy with ESO (FINCA), University of Turku, FI-20014 University of Turku, Finland
[138] Aalto University Metsähovi Radio Observatory, Metsähovintie 114, 02540, Kylmälä, Finland
[139] Departamento de Astronomía, Universidad de Chile, Camino El Observatorio 1515, Las Condes, Santiago, Chile
[140] Observatoire Astronomique de Strasbourg, Université de Strasbourg, CNRS, 11 rue de l'Université, F-67000 Strasbourg, France
[141] Université Paris-Saclay, Université Paris Cité, CEA, CNRS, AIM, 91191, Gif-sur-Yvette, France
[142] Key Laboratory of Space Astronomy and Technology, National Astronomical Observatories, Chinese Academy of Sciences, Beijing 100101, People's Republic of China
[143] IRAP, Université de Toulouse, CNRS, CNES, UPS, Toulouse, France
[144] Université Paris Cité, CNRS, CEA, Astroparticule et Cosmologie, F-75013 Paris, France
[145] Université Paris-Saclay, CNRS/IN2P3, IJCLab, 91405 Orsay, France
[146] Max-Planck-Institut für extraterrestrische Physik, Giessenbachstrasse 1, 85748 Garching, Germany
[147] Special Astrophysical Observatory of the Russian Academy of Sciences, Nizhny Arkhyz 369167, Russia
[148] Instituto de Astronomía, Universidad Nacional Autónoma de México, km 107 Carretera Tijuana-Ensenada, 22860, Ensenada, Baja California, Mexico
[149] Moscow Center for Advanced Studies, Kulakova str. 20, Moscow, 123592, Russia
[150] Aix Marseille Univ, CNRS, CNES, LAM, Marseille, FranceIndependent researcher.
Received 2025 March 7; revised 2026 June 1; accepted 2026 June 5; published 2026 August 5

Abstract

High-energy astrophysical neutrinos serve as crucial messengers for understanding hadronic acceleration processes and identifying the origins of cosmic rays, with blazars among the most promising neutrino sources. The KM3NeT experiment reported the detection of an ultrahigh-energy neutrino with an energy estimate of ∼220 PeV, the most energetic yet observed. The neutrino arrival direction has a 99% confidence region of 3° radius centered at R.A. 94°.3, decl. −7°.8 (J2000). In this work, 17 candidate blazars located within this region are identified. Comprehensive new observations and archival data analysis for these sources are presented. The study provides a complete multiwavelength coverage across radio, optical, X-ray, and gamma-ray bands, including proprietary data and dedicated follow-up observations. This study highlights flaring behavior in several candidate counterparts. One object exhibits a radio flare coinciding with the neutrino arrival time, with a pre-trial chance probability of 0.26%. Only for this object, the chance probability could be quantified in a robust way. Another candidate displays a rising trend in X-ray flux in a 1 yr window around the neutrino arrival time, while a third undergoes a gamma-ray flare during the same period. Based on the observational findings presented here, while none of these candidates can conclusively be linked to the neutrino, the implications of a possible blazar origin for the KM3NeT event are discussed.

Unified Astronomy Thesaurus concepts: Blazars (164); Neutrino telescopes (1105); Ultra-high-energy cosmic radiation (1733); Neutrino astronomy (1100); High energy astrophysics (739); Time domain astronomy (2109)

1. Introduction

The detection of an ultrahigh-energy (UHE; in the range of ∼50 PeV to EeV) neutrino by KM3NeT (S. Aiello et al. 2025a), the deep-sea neutrino observatory in the Mediterranean, marks a significant milestone in neutrino astrophysics. This event is far more energetic than any previously observed astrophysical neutrino, and challenges the current understanding of the cosmic neutrino spectrum, which exhibits a steep decline at the highest energies (R. Abbasi et al. 2022; KM3NeT Collaboration et al. 2025). The observation of astrophysical neutrinos in the high-energy (HE) range (in the range of TeV–PeV) and UHE range represents important progress in unraveling the origins of cosmic rays. As cosmic rays accelerate and propagate through space, they may interact with ambient matter or radiation fields, triggering hadronic processes that produce HE neutrinos. These neutrinos serve as unambiguous tracers of cosmic-ray acceleration, as their production is exclusively tied to hadronic interactions.

While the detection of an astrophysical diffuse neutrino flux is well established, the nature of the astrophysical sources dominating this emission remains a major open question (KM3NeT Collaboration et al. 2025; O. Adriani et al. 2026). The detection of the KM3NeT event could indicate the existence of a new class of extreme cosmic accelerators, distinct from those responsible for the bulk of the HE neutrino flux. It may also represent the first observation of a

[151] The shown author affiliations reflect their job contracts; the KM3NeT Collaboration has currently suspended all institutional relations with Russian science organizations.
[152] Deceased.
[153] Resident at Naval Research Laboratory, Washington, DC 20375
[154] Independent researcher.

cosmogenic neutrino (V. S. Berezinsky & G. T. Zatsepin 1969; O. Adriani et al. 2025a), produced in interactions between UHE cosmic rays and the cosmic radiation background. The observation of such an extreme event can be used to constrain fundamental physical quantities, such as the constancy of the speed of light (O. Adriani et al. 2025b).

Given the typical error region of neutrino events, chance spatial coincidences with one or more astrophysical objects may occur, requiring additional evidence for a definitive neutrino source association. For this reason, previous research has focused on population studies or variable behavior of candidate sources, in synergy with multiwavelength and time-domain astronomical observations, to identify potential associations.

Among the candidate sources of HE and UHE cosmic rays are blazars. Blazars are a subclass of active galactic nuclei (AGN) with highly collimated jets pointing almost directly toward Earth. They emit across the whole electromagnetic spectrum from radio frequencies to VHE ($\gtrsim$100 GeV) gamma rays (R. Blandford et al. 2019; M. Böttcher 2019; J. Jormanainen et al. 2023) and can display strong variability on timescales ranging from minutes to years. The first promising association between a HE neutrino event and a blazar was reported in 2017 with the detection of neutrino IceCube-170922A from the direction of the blazar TXS 0506+056, which was flaring in gamma rays (M. G. Aartsen et al. 2018). Since then, correlations between blazars and neutrino detections have been examined in many studies. They suggest a potential connection between the extremely HE processes in or near blazars and the production of neutrinos (F. Krauß et al. 2014; P. Padovani et al. 2019; A. Franckowiak et al. 2020; P. Giommi et al. 2020; T. Hovatta et al. 2021; S. Das et al. 2022; S. Buson et al. 2022b, 2023; R. Abbasi et al. 2023; C. Bellenghi et al. 2023; A. V. Plavin et al. 2023; A. Albert et al. 2024; S. Garrappa et al. 2024; P. M. Kouch et al. 2024). This evidence supports the hypothesis that blazars play a major role in the production of HE cosmic rays and neutrinos. However, definitive proof remains elusive.

Following this motivation, in this paper, a possible blazar origin for the KM3NeT event is investigated. Combining archival data, public and proprietary, and new observations, an improved identification of candidate counterparts is presented together with a detailed characterization of their multi-wavelength properties. Candidate blazars are identified through a combination of four methods: (i) a crossmatch of the first eROSITA catalog (eRASS1; A. Merloni et al. 2024) with the NRAO VLA Sky Survey (NVSS) catalog (at 1.4 GHz; J. J. Condon et al. 1998), further selected with infrared (IR) data from the Wide-field Infrared Survey Explorer (WISE; R. M. Cutri et al. 2021) (ii) very long baseline interferometry (VLBI), combining the Radio Fundamental Catalog (RFC; L. Y. Petrov & Y. Y. Kovalev 2025) with a dedicated observation of the field with the Very Long Baseline Array (VLBA) (iii) sources previously cataloged as blazars in the 5th edition of the Roma BZ Catalog (5BZCAT; E. Massaro et al. 2015) (iv) gamma-ray sources reported in the Fermi-LAT fourth source catalog (4FGL-DR4; S. Abdollahi et al. 2020; J. Ballet et al. 2023). The candidate blazars that are positionally consistent with KM3-230213A are studied over the full electromagnetic spectrum, from radio to gamma rays.

The paper is organized as follows. In Section 2, the properties of the event are briefly presented. In Section 3, a comprehensive summary of the archival data and new dedicated observations is provided, realizing the most complete observational coverage of these sources to date. In Section 4, the methodology adopted to pinpoint objects of likely blazar nature in the region of KM3-230213A is introduced. Further developing the initial search for counterparts reported in the previous study (S. Aiello et al. 2025a), which identified 12 blazar candidates, in this work, the sample is expanded to 17 potential blazar associations in the 99% confidence region of KM3-230213A using VLBI observations conducted with the VLBA. In Section 5.1, the properties and behavior of candidates exhibiting electromagnetic flaring in correspondence with the neutrino arrival time are highlighted. Finally, in Section 6, the consistency between these observational findings and the blazar–neutrino association hypothesis is discussed in light of current models of the HE emission in blazars. Section 7 summarizes the observational results and discusses potential strategies to narrow the source selection in future neutrino events.

2. The UHE Event KM3-230213A

The KM3NeT Collaboration is building two large-volume neutrino detectors in the depths of the Mediterranean Sea (S. Adrian-Martinez et al. 2016). The KM3NeT/ORCA detector, located near Toulon (France), will be equipped with 115 detector lines, with a geometry optimized for the detection of GeV–scale neutrinos and the study of atmospheric neutrino oscillations. The KM3NeT/ARCA detector is located near Portopalo di Capo Passero in Sicily (Italy) and will consist of two blocks of 115 detector lines, with larger spacings optimized for TeV–PeV astrophysical neutrinos (S. Aiello et al. 2024). Each detection line, anchored on the sea bed, comprises 18 digital optical modules (S. Aiello et al. 2022), containing 3180 mm photomultiplier tubes S. Aiello et al. (2025b).

On 2023 February 13, KM3NeT/ARCA detected an exceptionally HE muon, originating most likely in the interaction of a cosmic neutrino. The energy of the detected muon is estimated at 120^{+110}_{-60} PeV. Assuming an astrophysical E^{-2} flux, the best-fit neutrino energy is ∼220 PeV with a 90% confidence interval of 72 PeV–2.6 EeV. The event is designated KM3-230213A (S. Aiello et al. 2025a). This event was detected with the ARCA21 detector configuration (21 active lines). The J2000 equatorial coordinates of KM3-230213A are R. A. = $94\overset{\circ}{.}3$, decl. = $-7\overset{\circ}{.}8$ ($06^{h}17^{m}12^{s}$, $-07°48'\,00''$); the UTC date and time of the detection was 2023-02-13T01:16:47.703Z (MJD = 59988.0533299). The directional error region is largely dominated by the current systematic uncertainty in the absolute orientation of the detector. The containment radii for different confidence levels are: $R(68\%) = 1\overset{\circ}{.}5$, $R(90\%) = 2\overset{\circ}{.}2$, and $R(99\%) = 3\overset{\circ}{.}0$. In the near future, a recalibration of the detector elements will provide a significant improvement in the localization accuracy of KM3-230213A.

3. Observational Data

The majority of the electromagnetic emission from blazars is commonly attributed to leptonic processes, such as synchrotron emission of accelerated electrons and inverse Compton scattering. The two processes may be coupled, with emission resulting from a synchrotron self-Compton process. In lepto-hadronic models, accelerated ions interact with photons or protons, producing neutral pions, decaying into HE gamma rays, and charged pions, decaying into muons and neutrinos (K. Mannheim & P. L. Biermann 1989; K. Mannheim et al. 1992; T. Hovatta & E. Lindfors 2019). Protons can also produce electromagnetic radiation through other means, such as Bethe–Heitler pair production or synchrotron processes. Furthermore, depending on the density of the emission region, gamma rays may cascade down to lower energies in the MeV and/or X-ray bands. Different electromagnetic signatures can, therefore, be exploited to identify and characterize candidate blazar sources.

The purpose of this study is two-fold. First, to obtain a complete survey of the region of interest (ROI) of KM3-230213A, aimed at blazar-like objects, across the wavelengths where such a task is achievable. Second, to improve the selection of blazar candidates introduced in S. Aiello et al. (2025a) and present a comprehensive multiwavelength characterization of such objects. The collection of observational data analyzed for this aim is presented in this section.

3.1. Radio

VLBI. For the purpose of this work, the VLBA has been used to observe all radio objects detected by the VLA Sky Survey (VLASS; M. Lacy et al. 2020) with a (2−4) GHz flux density greater than 50 mJy within the ROI of KM3-230213A. The dedicated observation was conducted on 2024 November 25, achieving a deeper and complete survey of the parsec-scale properties of the radio objects in the region, complementing the existing VLBI archival data. The selection results in 42 objects. Notably, the observation did not target the previously identified object PMN J0618-0954, which is a likely blazar candidate. Almost all of its radio emission comes from parsec scales and has a rising spectrum, leading to a VLASS (2 −4 GHz) flux density <50 mJy while the VLBI (8 GHz) flux density is ⩾100 mJy. Lacking clear indications of strong variability, the difference between the two measurements is likely caused by the source emission spectrum. For the 42 observed objects, measurements at two center frequencies of 4.4 GHz and 7.6 GHz were obtained using the wide C-band receiver, with 4 Gbps total bandwidth, 128-MHz wide frequency channels, and two 6 minute scans per target. In the VLBA archive, this experiment is listed as BK257. Source positions for observations and correlations are taken from the RFC (L. Y. Petrov & Y. Y. Kovalev 2025) when available, or from VLASS if no RFC counterpart is present.

Results for sources observed within this VLBA program are presented in Table 1. The calibrated visibility and image FITS files of these observations are published in an electronic format. These measurements allow us to select highly luminous AGN jets with strong beaming. Sources where the parsec-scale radio emission (VLBI) is bright, dominates over larger scales (Very Large Array), and has a flat radio spectrum at parsec scales due to synchrotron opacity are identified as likely blazars, with the radio emission coming from jets aligned with the line of sight.

Sources are marked as primary candidate blazars in Table 1 when they meet all the following criteria: (i) detected on parsec scales with compactness $S_{\rm V\,LBA}^{5\,\rm GHz}/S_{\rm V\,LASS} > 0.5$, (ii) parsec-scale (5–8) GHz spectral index $\alpha_{\rm VLBA} > -0.5$, (iii) core brightness temperature $T_{\rm b} > 10^{10}$ K at either 5 GHz or 8 GHz. The observed flux densities at the end of 2024 are similar to historical averages (Table 1). In particular, no major flare was detected during this time.

Radio light curves. Light curves at 15 GHz obtained from the Owens Valley Radio Observatory (OVRO; J. L. Richards et al. 2011) and RATAN-600 observational campaigns (Appendices A.1.2, A.1.3) are exploited for the time-dependent study of the radio emission.

The calibrator source catalog of the Atacama Large Millimeter/submillimeter Array (ALMA[155]) is used for complementary variability information.

3.2. IR and Optical

IR observations are retrieved from public archival data of the WISE (E. L. Wright et al. 2010) and the Near-Earth Object Wide-field Infrared Survey Explorer (NEOWISE; A. Mainzer et al. 2011) programs. Public archival optical data are collected from the Asteroid Terrestrial-impact Last Alert System (ATLAS; A. N. Heinze et al. 2018; J. L. Tonry et al. 2018; K. W. Smith et al. 2020), the Catalina Real-Time Transient Survey (CRTS; A. J. Drake et al. 2009), the Zwicky Transient Facility (ZTF; F. J. Masci et al. 2018) ground-based telescopes, and the space-based Gaia mission (Gaia Collaboration et al. 2016, 2023; C. Babusiaux et al. 2023). See Appendix A.2.

3.3. X-Rays

For the purpose of this work, the Micro-channel X-ray Telescope (MXT) and ECLAIR instruments on board the Space Variable Objects Monitor (SVOM; J. Wei et al. 2016) were used to observe the 90% containment region in order to identify bright X-ray sources potentially associated with KM3-230213A. This survey complements the proprietary four-epoch data obtained from the eROSITA instrument on board the Spektrum-Roentgen-Gamma (SRG) observatory (P. Predehl et al. 2021), covering all AGN-like objects in the region. Target-of-opportunity observations were conducted in December 2024 with the Swift-X-Ray Telescope (XRT) on board the Neil Gehrels Swift Observatory (Swift; D. N. Burrows et al. 2005), for two sources identified as privileged candidates for a dedicated follow-up (in the Swift archive, these observations are listed as ObsIDs: 00018990001 and 00036371010).

For all the sources identified as candidate blazars in this work, public archival data were collected from Swift-XRT, the Chandra X-ray Observatory (Chandra; M. C. Weisskopf et al. 2000), and the ROentgen SATellite (ROSAT; T. Chlebowski et al. 1991). All the X-ray data were analyzed to estimate the intrinsic flux in the (0.2–2.3) keV band. A detailed summary of the estimated fluxes is provided in Table 2. The historical average of the available measurements for each source is further reported in Table 3.

SVOM-MXT *and* ECLAIR survey. The SVOM satellite was launched on 2024 June 22. At the time of the observations, between 2024-12-16T16:52:25.535Z UTC and 2024-12-17T13:53:34.693Z UTC (spanning 14 orbits), SVOM was in the commissioning and verification phase. SVOM observed the 90% neutrino error region using a Multi-Messenger Target of Opportunity (ToO-MM) program. ToO-MM allowed the narrow field-of-view (FoV) instruments on board SVOM, the MXT (D. Götz et al. 2023), operating in the soft 0.5–10 keV X-ray band with a 58×58 arcmin^2 FoV, and the Visible Telescope (VT; X. Fan et al. 2020), operating in the VT_B (400–650 nm) and VT_R (650–1000 nm) bands, with a FoV of

[155] https://almascience.nrao.edu/alma-data/calibrator-catalog

Table 1
Properties of Sources Observed with VLBA within 3° from the KM3-230213A Position

Blaz (1)	Name (J2000) (2)	Position J2000 R.A. and Decl. (3)	Sep (deg) (4)	z (5)	$S_{\rm VLASS}$ 2–4 GHz (mJy) (6)	$S_{\rm VLBA}$ Hist 8 GHz (mJy) (7)	$S_{\rm VLBA}$ 5 GHz (mJy) (8)	$S_{\rm VLBA}$ 8 GHz (mJy) (9)	$\alpha_{\rm VLBA}$ 5–8 GHz (10)	Core $T_{\rm b}$ 5 GHz (K) (11)	Core $T_{\rm b}$ 8 GHz (K) (12)
x	J0607−0834	06:07:59.699 −08:34:49.978*	2.4	0.87	3100	2067	2176 ± 220	2240 ± 226	0.05 ± 0.26	$10^{11.9\pm0.1}$	$10^{11.3\pm0.1}$
x	J0606−0724	06:06:43.546 −07:24:30.231*	2.6	1.227	461	309	379 ± 38	306 ± 31	−0.38 ± 0.26	$>10^{12.0}$	$10^{10.4\pm0.1}$
x	J0616−1041	06:16:41.808 −10:41:08.456*	2.9	⋯	197	185	215 ± 22	248 ± 25	0.26 ± 0.26	$>10^{10.4}$	$>10^{12.1}$
x	J0622−0656	06:22:58.046 −06:56:51.971*	1.7	⋯	101	103	111 ± 11	87 ± 9	−0.42 ± 0.26	$>10^{12.1}$	$>10^{10.9}$
x	J0610−0959	06:10:50.711 −09:59:33.958*	2.7	⋯	97	78	100 ± 10	94 ± 10	−0.11 ± 0.26	$>10^{12.1}$	$>10^{11.4}$
x	J0622−0846	06:22:37.999 −08:46:18.263*	1.7	⋯	61	74	93 ± 10	109 ± 12	0.28 ± 0.27	$>10^{12.2}$	$>10^{12.0}$
x	J0605−0759	06:05:26.187 −07:59:31.786*	2.9	⋯	149	74	76 ± 8	67 ± 7	−0.24 ± 0.27	$10^{9.9\pm0.1}$	$10^{10.2\pm0.1}$
x	J0614−0918	06:14:06.042 −09:18:37.911*	1.7	⋯	95	63	72 ± 7	55 ± 6	−0.46 ± 0.27	$10^{10.5\pm0.2}$	$>10^{9.8}$
x	J0612−0700	06:12:04.843 −07:00:22.853	1.5	⋯	63		54 ± 6	62 ± 7	0.24 ± 0.27	$10^{10.2\pm0.1}$	$>10^{11.0}$
x	J0612−0552	06:12:37.360 −05:52:44.418*	2.2	⋯	65	62	53 ± 6	45 ± 5	−0.29 ± 0.27	$10^{10.5\pm0.3}$	$>10^{10.0}$
	J0609−0615	06:09:39.974 −06:15:05.858*	2.4	2.219	83	39	70 ± 7	48 ± 5	−0.66 ± 0.27	$10^{9.8\pm0.1}$	$10^{9.5\pm0.1}$
	J0615−0934	06:15:35.497 −09:34:27.996*	1.8	⋯	105	30	67 ± 7	39 ± 4	−0.97 ± 0.27	$10^{9.9\pm0.1}$	$10^{9.0\pm0.1}$
	J0620−1036	06:20:27.542 −10:36:22.106*	2.9	⋯	172	39	63 ± 7	43 ± 5	−0.66 ± 0.27	$10^{9.6\pm0.1}$	$10^{9.2\pm0.1}$
	J0624−0735	06:24:55.342 −07:35:37.194	1.9	⋯	110	⋯	58 ± 6	50 ± 5	−0.25 ± 0.27	$10^{9.9\pm0.1}$	$10^{9.2\pm0.1}$
	J0622−0723	06:22:44.911 −07:23:34.839	1.4	⋯	94	⋯	53 ± 6	32 ± 4	−0.86 ± 0.28	$10^{9.1\pm0.1}$	$>10^{9.8}$
	J0621−0609	06:21:10.364 −06:09:54.206*	1.9	⋯	132	65	49 ± 7	44 ± 5	−0.18 ± 0.31	$>10^{9.9}$	$>10^{10.6}$
	J0620−0638	06:20:42.818 −06:38:24.334*	1.5	⋯	101	26[c]	25 ± 3	18 ± 2	−0.55 ± 0.30	$>10^{10.4}$	$>10^{9.8}$
	J0608−0727	06:08:04.370 −07:27:32.822*	2.3	⋯	356	19	23 ± 3	22 ± 3	−0.09 ± 0.30	$>10^{10.9}$	$>10^{10.6}$
	J0623−0609	06:23:23.723 −06:09:22.673	2.3	⋯	53	⋯	20 ± 2	23 ± 3	0.23 ± 0.31	$>10^{10.7}$	$>10^{10.3}$
	J0616−0648	06:16:33.667 −06:48:03.289	1.0	⋯	52	⋯	19 ± 2	18 ± 2	−0.04 ± 0.31	$>10^{9.7}$	$>10^{9.9}$
	J0611−0800	06:11:58.357 −08:00:11.217*	1.3	⋯	88	14	17 ± 2	18 ± 2	0.14 ± 0.28	$>10^{10.3}$	$>10^{10.1}$
	J0624−0826	06:24:30.354 −08:26:38.949	1.9	⋯	56	⋯	13 ± 2	17 ± 2	0.41 ± 0.37	$>10^{9.5}$	$>10^{8.4}$
	J0617−0515	06:17:50.307 −05:15:07.396	2.6	⋯	98	⋯	28 ± 3	>16	⋯	$10^{7.6\pm0.1}$	$10^{6.7\pm0.4}$
	J0605−0757	06:05:10.018 −07:57:50.331	3.0	⋯	53	⋯	>26	⋯	⋯	$>10^{6.7}$	⋯
	J0616−0525	06:16:31.146 −05:25:32.225	2.4	⋯	77	⋯	>9	>9	⋯	$>10^{8.6}$	$>10^{7.3}$
	J0610−0725	06:10:02.513 −07:25:12.715	1.8	⋯	57	⋯	>7	>10	⋯	$>10^{6.6}$	$>10^{7.6}$
	J0613−0955	06:13:39.450 −09:55:34.713	2.3	⋯	75	⋯	⋯	>9	⋯	⋯	$>10^{7.7}$
	J0608−0843	06:08:28.480 −08:43:53.539	2.4	⋯	69	⋯	<6		⋯	⋯	⋯
	J0613−0655	06:13:40.138 −06:55:34.607	1.2		123	<12	<6		⋯	⋯	⋯
	J0619−0731	06:19:06.739 −07:31:07.183	0.6	⋯	51	⋯	<6		⋯	⋯	⋯
	J0605−0716	06:05:27.091 −07:16:23.639	3.0	⋯	50	⋯	<6		⋯	⋯	⋯
	J0607−0610	06:07:16.721 −06:10:29.815	2.9	⋯	71	<20	<6		⋯	⋯	⋯
	J0608−0738	06:08:03.661 −07:38:31.374	2.3	⋯	192	<12	<6		⋯	⋯	⋯
	J0608−0700	06:08:36.934 −07:00:01.723	2.3	⋯	93	<20	<6		⋯	⋯	
	J0610−0559	06:10:09.582 −05:59:51.932	2.5	⋯	67	<20	<6		⋯	⋯	⋯
	J0610−0611	06:10:50.604 −06:11:49.999	2.2	⋯	111	<20	<6		⋯	⋯	⋯
	J0614−1038	06:14:45.393 −10:38:04.475	2.9	⋯	81	⋯	<6		⋯	⋯	⋯
	J0615−0644	06:15:47.557 −06:44:47.652	1.1	⋯	78	⋯	<6		⋯	⋯	⋯
	J0618−0719	06:18:47.839 −07:19:15.503	0.6	⋯	59	⋯	<6		⋯	⋯	⋯
	J0624−0721	06:24:14.681 −07:21:05.721	1.8	⋯	57	⋯	<6		⋯	⋯	⋯
	J0625−0904	06:25:18.204 −09:04:35.619	2.4	⋯	64	⋯	<6		⋯	⋯	⋯
	J0625−0703	06:25:29.624 −07:03:37.547	2.2	⋯	60	⋯	<6		⋯	⋯	⋯

Note. Column (1): "x" denotes a primary blazar candidate, see the details in Appendix A.1.1. Column (2): J2000 source name. Column (3): J2000 source positions, R.A. and decl.; asterisk "*" denotes VLBI-astrometry positions from RFC, the rest of the coordinates are taken from the VLASS. Column (4): separation between the KM3-230213A position and the source position in degrees. Column (5): redshift as reported by the NASA Extragalactic Database. Column (6): flux density at (2−4) GHz measured within the VLASS. Column (7): historic total VLBI flux density from the RFC database at 8 GHz; in case the 5 GHz VLBI flux density is available instead, it is marked by the note "c". Columns (8) and (9): total VLBI flux density at 5 and 8 GHz with its 1σ uncertainty, measured by the VLBA observations on 2024 November 25, respectively. Column (10): VLBA total spectral index between 5 and 8 GHz α ($S \propto \nu^{\alpha}$). Columns (11) and (12): brightness temperature of the core at 5 and 8 GHz with 1σ uncertainty, respectively. Uncertainties of the VLBI flux scale are about or less than 10%; this uncertainty is accounted for in the measurements presented in this table.

Table 2
Fluxes Derived from the Available X-Ray Data in the 0.2–2.3 keV Band, Given in Units of 10^{-13} erg cm^{-2} s^{-1}

Source	Instrument	MJD	Flux
#1 MRC 0614-083	ROSAT[a]	48150	$1.39^{+0.82}_{-0.82}$
	eROSITA	58945	$3.56^{+0.98}_{-0.79}$
	eROSITA	59132	$3.94^{+1.49}_{-1.06}$
	eROSITA	59308	$6.43^{+1.15}_{-1.05}$
	eROSITA	59492	$7.97^{+1.27}_{-1.11}$
	Swift-XRT	60666	$10.2^{+1.61}_{-1.43}$
#3 PMN J0622-0657	eROSITA	58945	$\leqslant 0.69$[b]
	eROSITA	59132	$1.02^{+1.94}_{-0.75}$
	eROSITA	59308	$1.46^{+2.62}_{-0.79}$
	eROSITA	59492	$\leqslant 0.65$[b]
#4 NVSS J062455-073536	eROSITA	58945	$\leqslant 2.50$[b]
	eROSITA	59132	$1.49^{+1.98}_{-0.82}$
	eROSITA	59308	$\leqslant 2.00$[b]
	eROSITA	59492	$\leqslant 0.81$[b]
#6 0605-085	ROSAT[c]	48147	$2.32^{+1.00}_{-1.00}$
	Chandra-ACIS-S	52031	$9.04^{+0.70}_{-0.64}$
	Swift-XRT	54214	$8.32^{+13.52}_{-7.26}$
	Swift-XRT	54235	$10.40^{+3.02}_{-1.85}$
	Swift-XRT	54321	$12.50^{+5.10}_{-3.26}$
	Swift-XRT	54323	$24.60^{+102.13}_{-13.90}$
	Swift-XRT	54682	$16.30^{+8.80}_{-5.24}$
	Swift-XRT	54684	$19.00^{+5.50}_{-3.90}$
	Swift-XRT	54687	$17.40^{+2.01}_{-1.73}$
	Swift-XRT	54787	$16.10^{+7.81}_{-4.42}$
	Chandra-ACIS-S	55179	$18.70^{+0.72}_{-0.63}$
	Chandra-ACIS-S	55182	$18.20^{+0.70}_{-0.63}$
	eROSITA	58945	$5.20^{+1.26}_{-1.06}$
	eROSITA	59132	$4.24^{+1.12}_{-0.97}$
	eROSITA	59308	$2.82^{+1.17}_{-0.83}$
	eROSITA	59492	$4.97^{+1.24}_{-1.07}$
	Swift-XRT	60670	$7.52^{+1.39}_{-1.19}$
#7 PMN J0609-0615	Swift-XRT	55571	$\leqslant 25.00$[b]
#8 PMN J0606-0724	eROSITA	58945	$\leqslant 0.71$[b]
	eROSITA	59132	$\leqslant 0.63$[b]
	eROSITA	59308	$0.36^{+0.43}_{-0.24}$
	eROSITA	59492	$\leqslant 0.35$
#9 PMN J0616-1040	eROSITA	58945	$4.40^{+1.09}_{-0.93}$
	eROSITA	59132	$1.68^{+0.64}_{-0.51}$
	eROSITA	59308	$5.18^{+4.02}_{-2.14}$
	eROSITA	59492	$\leqslant 0.26$[b]
#10 NVSS J060639-063421	ROSAT	49244	$0.77^{+0.23}_{-0.18}$
	eROSITA	58945	$\leqslant 0.72$[b]
	eROSITA	59132	$0.36^{+0.34}_{-0.26}$
	eROSITA	59308	$\leqslant 1.32$[b]
	eROSITA	59492	$\leqslant 0.65$[b]
#11 PMN J0605-0759	eROSITA	58945	$1.47^{+1.22}_{-0.66}$
	eROSITA	59132	$0.75^{+0.77}_{-0.40}$
	eROSITA	59308	$2.13^{+0.86}_{-0.68}$
	eROSITA	59492	$3.62^{+1.33}_{-0.95}$
#12 NVSS J060509-075747	eROSITA	58945	$3.11^{+3.48}_{-1.48}$
	eROSITA	59132	$0.92^{+1.55}_{-0.58}$
	eROSITA	59308	$1.29^{+1.62}_{-0.72}$
	eROSITA	59492	$2.38^{+1.13}_{-0.75}$

Table 2
(Continued)

Source	Instrument	MJD	Flux
#13 PMN J0612-0700	eROSITA	58945	$\leqslant 0.29$[b]
	eROSITA	59132	$\leqslant 0.72$[b]
	eROSITA	59308	$\leqslant 1.81$[b]
	eROSITA	59492	$\leqslant 1.10$[b]
#17 NVSS J061050-095934	eROSITA	58945	$\leqslant 1.35$[b]
	eROSITA	59132	$\leqslant 0.25$[b]
	eROSITA	59308	$\leqslant 0.76$[b]
	eROSITA	59492	$0.77^{+0.64}_{-0.38}$

Notes. Uncertainties are reported at the 1σ confidence level.
[a] Derived flux in the (0.1–2.4) keV energy range.
[b] Upper limits.
[c] Derived flux in the (0.2–2.0) keV energy range.

26′ diameter, to perform tiled observations of the error region with exposure times ranging from 400 to 2350s. A total of 21 tiles were observed with an average exposure time of 1218.9 s. SVOM-MXT data were processed with its dedicated analysis pipeline. No soft X-ray source was detected in the 90% neutrino error region. Consequently, 3σ upper limits on the 0.5–10 keV energy flux were computed at the center of each tile following R. P. Kraft et al. (1991). The variability of the upper limit across the tiled region is primarily driven by differences in exposure time for each tile. The tiling pattern and the corresponding MXT energy flux upper limits for each tile are shown in Figure 1. None of the candidate blazars listed in Table 3 and lying in the 90% neutrino error region were located in the VT FoV.

In addition, the coded mask instrument SVOM-ECLAIRs (O. Godet et al. 2014), with its wide FoV of 2sr, observed the entire error region over the 4–150 keV energy range during the total ToO exposure of 25.6 ks. No source was detected. For each of the 17 blazars listed in Table 3, 3σ upper limits over different energy bands were derived from the ECLAIRs variance maps produced by the ECPI data processing pipeline v1.14.4 and assuming a power-law spectral model with $\Gamma = 2$. They are summarized in Figure 2.

3.4. Gamma Rays

The data from the Large Area Telescope (LAT) on board the Fermi Gamma-ray Space Telescope, providing continuous observations of the full sky in the 0.1–1000 GeV energy range, are analyzed (Fermi-LAT; W. B. Atwood et al. 2009). The aim is to characterize the gamma-ray emission at the best-fit neutrino position of the KM3NeT event, search for potential new point sources in the uncertainty region, and characterize all sources, whether previously cataloged or not, positionally consistent with KM3-230213A.

To check for previously undetected sources, an iterative procedure using a test statistic (TS) map is applied. The TS is defined as $2\log(L/L_0)$, where L is the likelihood of the model with a point source at a given position, and L_0 is the likelihood without the source. A TS value of 25 corresponds to a statistical significance of $\gtrsim 4.0\sigma$ (as adopted in S. Abdollahi et al. 2020; J. R. Mattox et al. 1996). A TS map is generated by inserting a putative point source at each pixel and evaluating its significance relative to the current best-fit model. The test source is modeled with a power-law spectrum, allowing only

Table 3
Candidate Blazars Identified Using the Methods Described in Section 4, Located within the 99% Confidence Region of KM3-230213A

Source	Names	Sep. (deg)	R.A. (deg) (J2000)	Decl. (deg) (J2000)	z	Methods	VLBI (mJy)	X-ray $[10^{-13}\frac{\mathrm{erg}}{\mathrm{cm}^2\,\mathrm{s}}]$
#1	**MRC 0614-083** NVSS J061703-082225 VLASS1QLCIR J061702.97-082229.2 WISE J061702.95-082229.5 1eRASS J061702.8-082230 WIBRaLS J0617-0822	0.6	94.2623	−8.3749	⋯	1	⋯	$5.58^{+1.16}_{-0.99}$ (R, e, S)
#2	**4FGL J0616.2-0653**	0.9	94.06	−6.90	⋯	4	⋯	$\leqslant 0.89$ (e)
#3	**PMN J0622-0657** NVSS J062258-065652 VLASS1QLCIR J062258.04-065651.9 RFC J0622-0656 WISEA J062258.02-065652.0 eRASSU J062257.8-065654	1.7	95.7419	−6.9478	⋯	2	87 ± 9	$0.62^{+1.48}_{-0.39}$ (e)
#4	**NVSS J062455-073536** VLASS1QLCIR J062455.34-073536.9 eRASSU J062454.9-073541 4FGL J0624.8-0735	1.9	96.2306	−7.5936	⋯	4	50 ± 5	$0.37^{+1.82}_{-0.21}$ (e)
#5	**PMN J0618-0954** NVSS J061820-095426 VLASS1QLCIR J061820.67-095425.3 RFC J0618-0954	2.1	94.5861	−9.9071	⋯	2	100	$\leqslant 0.93$ (e)
#6	**0605-085** NVSS J060759-083450 VLASS1QLCIR J060759.69-083450.3 RFC J0607-0834 WISE J060759.61-083451.6 1eRASS J060759.7-083448 (H) 4FGL J0608.0-0835 CGRaBS J0607-0834 BZQ J0607-0834	2.4	91.9987	−8.5805	0.87	1, 2, 3, 4	2240 ± 226	$11.6^{+9.25}_{-2.89}$ (R, C, S, e)
#7	**PMN J0609-0615** NVSS J060940-061505 VLASS1QLCIR J060939.98-061505.6 RFC J0609-0615 WISEA J060939.96-061506.0 BZQ J0609-0615	2.4	92.41656	−6.25163	2.219	3	48 ± 5	$\leqslant 1.47$ (e)
#8	**PMN J0606-0724** NVSS J060643-072430 VLASS1QLCIR J060643.54-072430.3 RFC J0606-0724 WISEA J060643.53-072430.1 1eRASS J060643.3-072429 CGRaBS J0606-0724 BZQ J0606-0724	2.6	91.68144	−7.40840	1.277	1, 2, 3	306 ± 31	$0.09^{+0.53}_{-0.06}$ (e)
#9	**PMN J0616-1040** NVSS J061641-104108 VLASS1QLCIR J061641.80-104108.5 RFC J0616-1041 WISE J061641.80-104108.4 1eRASS J061641.5-104107 4FGL J0616.7-1049 CGRaBS J0616-1041 WIBRaLS J061641.80-104108.4	2.9	94.17420	−10.68568	⋯	1, 2, 4	248 ± 25	$2.82^{+1.5}_{-0.89}$ (e)
#10	**NVSS J060639-063421** VLASS1QLCIR J060640.01-063419.3 WISEA J060640.00-063419.6	2.9	91.6667	−6.5721	⋯	1	⋯	$0.23^{+0.65}_{-0.09}$ (R, e)

Table 3
(Continued)

Source	Names	Sep. (deg)	R.A. (deg) (J2000)	Decl. (deg) (J2000)	z	Methods	VLBI (mJy)	X-ray $[10^{-13} \frac{erg}{cm^2 s}]$
	1eRASS J060640.2-063424							
#11	**PMN J0605-0759** NVSS J060526-075928 VLASS1QLCIR J060526.19-075931.9 RFC J0605-0759 WISE J060526.16-075931.7 1eRASS J060527.0-075925 WIBRaLS J0605-0759	2.9	91.35911	−7.99216	⋯	1, 2a	67 ± 7	$1.99^{+1.04}_{-0.67}$ (e)
#12	**NVSS J060509-075747** VLASS1QLCIR J060508.92-075747.4 WISEA J060509.22-075747.1 1eRASS J060509.0-075739	3.0	91.28843	−7.96308	⋯	1	⋯	$1.93^{+1.94}_{-0.88}$ (e)
#13	**PMN J0612-0700** NVSS J061204-070022 VLASS1QLCIR J061204.84-070022.8 eRASSU J930117.21-070019	1.5	93.02018	−7.00635	⋯	2a	62 ± 7	$\leqslant$0.98 (e)
#14	**PMN J0614-0918** NVSS J061406-091837 VLASS1QLCIR J061406.04-091837.8 RFC J0614-0918	1.7	93.52517	−9.31053	⋯	2a	55 ± 6	$\leqslant$0.85 (e)
#15	**PMN J0622-0846** NVSS J062237-084617 VLASS1QLCIR J062238.00-084618.2 RFC J0622-0846	1.7	95.65833	−8.77174	⋯	2a	109 ± 12	$\leqslant$1.13 (e)
#16	**NVSS J061237-055244** VLASS1QLCIR J061237.35-055244.4 RFC J0612-0552 SSTSL2 J061237.36-055244.4	2.2	93.15567	−5.87900	⋯	2a	45 ± 5	$\leqslant$1.17 (e)
#17	**NVSS J061050-095934** VLASS1QLCIR J061050.71-095933.8 RFC J0610-0959 WISEA J061050.70-095933.8 eRASSU J061051.1-095936	2.7	92.71130	−9.99277	⋯	2a	94 ± 10	$0.19^{+0.75}_{-0.09}$ (e)

Note. Positions are provided in equatorial (J2000) coordinates, with the primary name (in bold) of each source corresponding to either a common name or the name in the first survey reporting the object. Associated sources across different wavelengths are reported, emphasizing the surveys and catalogs relevant to each selection method. For completeness, the counterparts from catalogs considered in this work are indicated regardless of the selection method. The listed coordinates prioritize counterparts in the following order: RFC (VLBI), IR surveys, VLASS, and Fermi-LAT analysis for the single gamma-ray-only detection. In the Methods column, the selection methods are reported (see Section 4): 1 (X-ray, radio, IR crossmatch), 2 (VLBI from RFC), 2a (VLBI from VLBA observation), 3 (5BZCAT), 4 (4FGL). Radio fluxes (8 GHz) and intrinsic, time-averaged X-ray fluxes in the (0.2–2.3) keV band are reported in the respective columns. The X-ray instruments from which the average has been calculated are indicated with a single letter: R (ROSAT), e (eROSITA), S (Swift-XRT), and C (Chandra). Details on the data origin are provided in Appendices A.1.1 and A.3. For one object, not detected by WISE, the IR association in the Spitzer (SEIP) source list (SSTSL2; Spitzer Science Center (SSC) & Infrared Science Archive (IRSA) 2021) is reported.

the normalization to vary while keeping the photon index fixed at 2.0. A search for peaks with TS > 25 and a minimum separation of $0\overset{\circ}{.}5$ from existing sources is performed. When a significant peak is found, a new point source is added to the model at that position, refitting the ROI and generating a new TS map. This process is iterated until no more significant excesses are found. The details of the adopted maximum-likelihood analysis and produced TS maps are given in Appendix A.4.

To search for transient and variable gamma-ray emission on intermediate timescales in the LAT data, the same method is applied to 1 day and 1 month intervals prior to the detection of KM3-230213A. No new significant ($>5\sigma$) excess emission is found within the 90% confidence localization of KM3-230213A. A 95% confidence upper limit for the 0.1 GeV flux is determined at the neutrino position: $<2.6 \times 10^{-10}$ ph cm^{-2} s^{-1} for the ∼16 yr integration, and $<1.75 \times 10^{-8}$ ($<1.7 \times 10^{-6}$) ph cm^{-2} s^{-1} for the 1 month (1 day) integration time. Over these timescales, none of the candidate objects exhibit significant flux enhancements that would suggest flaring behavior or spectral change at gamma rays.

Since the target is close to the Galactic plane, the analysis is repeated using a more restrictive lower energy threshold of $\geqslant$1 GeV to reduce contamination from bright galactic emission. This approach also takes advantage of the improved

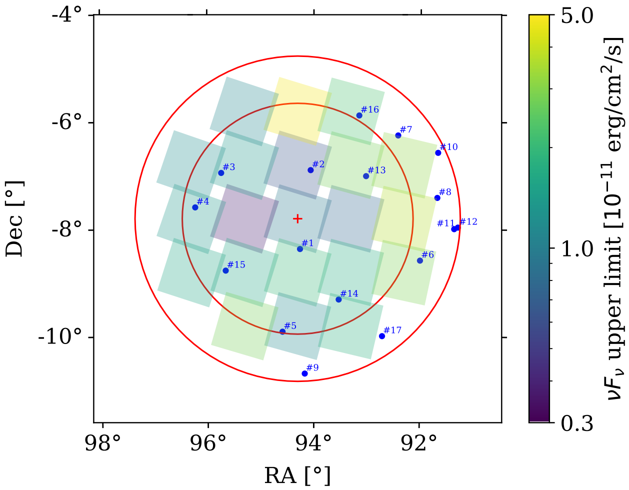

Figure 1. 3σ upper limits derived from the tiling of the neutrino error region with SVOM-MXT over the 0.5–10 keV energy band. The concentric red circles indicate the 90% and 99% error regions of KM3-230213A, respectively. The numbers refer to the candidate blazars listed in Table 3.

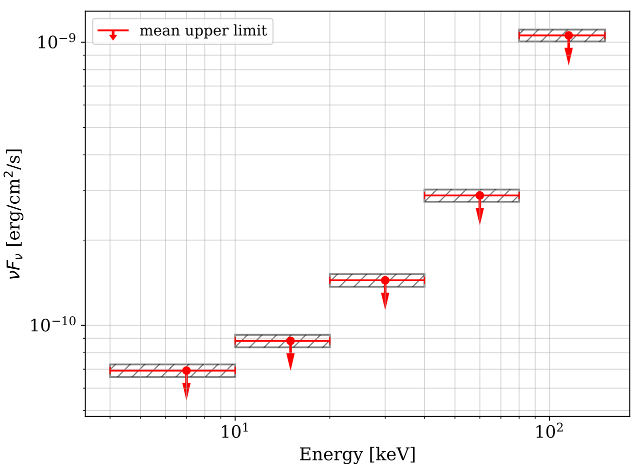

Figure 2. SVOM-ECLAIRs 3σ upper limits on the energy flux in different energy ranges for the candidate blazars listed in Table 3. The average upper limits for the 17 targets are shown with red markers. The horizontal hatched bands cover the interval between the minimum and maximum upper limits for the candidate sample.

LAT point-spread function (PSF) at higher energies. The results remain consistent with those obtained from the full energy range analysis.

4. Candidate Blazar Counterparts

As part of the initial study of KM3-230213A (S. Aiello et al. 2025a), multiwavelength archival data were explored to compile a census of potential blazar companions within the 99% confidence region of the event. In this work, while maintaining the original four selection methods, the sample is expanded from 12 to 17 candidates thanks to VLBI observations conducted with the VLBA see Appendix A.1.1). The updated selection methods are the following:

1. Method 1: This strategy relies on the distinctive X-ray, radio, and IR properties of blazars. By crossmatching the first eROSITA catalog (eRASS1; A. Merloni et al. 2024) with the NVSS catalog (at 1.4 GHz; J. J. Condon et al. 1998), eighteen sources with radio fluxes exceeding 10mJy are identified. The sources are positionally crossmatched with WISE (R. M. Cutri et al. 2021). The measured WISE colors of these objects are used to select those that populate the "WISE blazar strip" (F. Massaro et al. 2012), narrowing the list of likely blazar candidates to seven objects (see Appendix A.2.1). Consistent results are found when crossmatching the eROSITA dataset with the DESI Legacy Survey DR10 (A. Dey et al. 2019) using the Bayesian tool NWAY (M. Salvato et al. 2018) combined with machine learning, as described in M. Salvato et al. (2022).
2. Method 2: radio blazars are selected on the basis of their parsec-scale flux measured by VLBI, as motivated by population studies (M. L. Lister et al. 2019) and previous works (e.g., blazars/ANTARES studies; A. Albert et al. 2024). Following the approach suggested in A. V. Plavin et al. (2023), VLBI measurements from RFC version 2024c (L. Y. Petrov & Y. Y. Kovalev 2025) are used. The catalog is complete down to a cutoff level of 100 mJy at 8 GHz. Objects above this threshold are selected, resulting in five objects with median VLBI flux density ranging from 0.1 to 2 Jy. In addition to RFC cataloged sources, six objects are pinpointed on the basis of their VLBI properties from the dedicated VLBA observation (see Appendix A.1.1). These are marked with the indication "2a" under "method" in Table 3.
3. Method 3: 5BZCAT (E. Massaro et al. 2015), a compilation of 3561 blazars, has been previously used to investigate the possible neutrino-blazar connection (S. Aiello et al. 2025a; S. Buson et al. 2022a, 2022b, 2023). Three objects in this catalog are located within the 99% confidence region.
4. Method 4: The 4FGL-DR4 (S. Abdollahi et al. 2020; J. Ballet et al. 2023) provides the most recent census of gamma-ray sources in the 50 MeV–1 TeV energy range. Four 4FGL-DR4 objects are found within the 99% confidence region of KM3-230213A. The Fermi Long-Term Transient Sources Catalog (L. Baldini et al. 2021), and the incremental version iFLT[156] are also considered. No iFLT sources are found within the uncertainty of the neutrino direction.

In total, 17 blazar candidates were pinpointed through the methods described above, with four sources selected through more than one method. The final list of objects is provided in Table 3, which includes their spatial distance from the KM3-230213A best-fit position, redshift (when available), associated electromagnetic counterparts, VLBI radio and X-ray flux measurements. The positions of these sources relative to the KM3-230213A confidence region are shown in Figure 3. With the exception of 4FGL J0616.2-0653 (#2), which is only detected through gamma rays, further discussed in Section 5.2, all the other sources are detected in radio.

Spectroscopic classifications and redshift determinations are available only for the three sources reported in the 5BZCAT. They are classified as flat-spectrum radio quasars based on the presence of broad emission lines in their optical spectra (E. Massaro et al. 2015). Object 0605-085 (#6, 5BZQ J0607-0834) is one of the 50 brightest radio blazars in the sky.

[156] https://www.ssdc.asi.it/fermi_iflt/

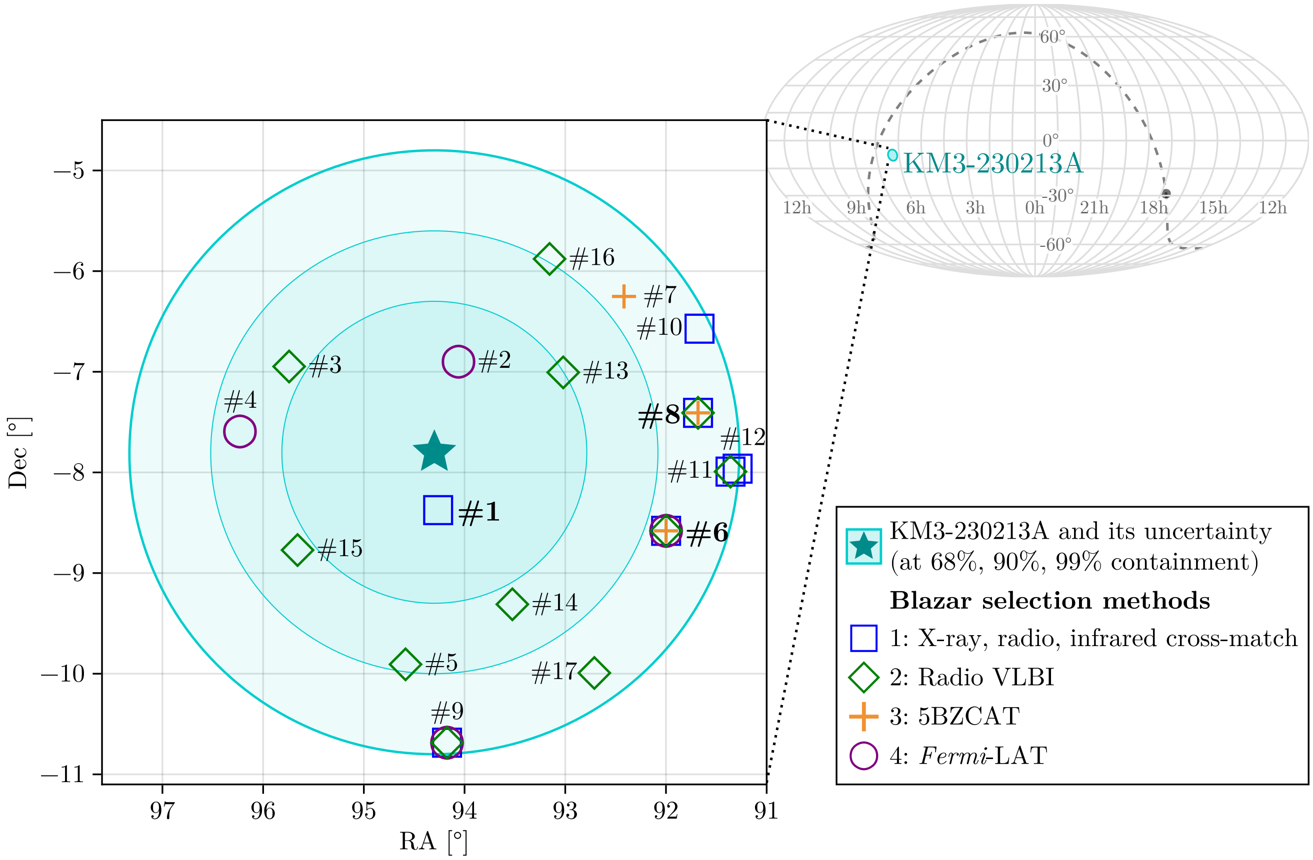

Figure 3. Summary of KM3-230213A and its candidate blazar counterparts selected in Section 4. Both the location of the KM3NeT event in equatorial coordinates (J2000) and its uncertainty regions are shown. The markers indicate the criteria used for the inclusion in the list of candidates as presented in Section 4. Source numbers refer to Table 3; the three blazars discussed in Section 6 are labeled in bold here: #1 (MRC 0614-083), #6 (0605-085), #8 (PMN J0606-0724).

Observations with the Hobby–Eberley Telescope detect the Hβ and Mg II emission lines, enabling a redshift estimate of $z = 0.870$ (M. S. Shaw et al. 2012). PMN J0609-0615 (#7, 5BZQ J0609-0615) is observed with the New Technology Telescope, revealing a broad C IV emission line corresponding to a redshift of $z = 2.219$ (M. S. Shaw et al. 2012). PMN J0606-0724 (#8, 5BZQ J0606-0724) appears in the Candidate Gamma-Ray Blazar Survey (CGRaBS) catalog (S. E. Healey et al. 2008) and has a spectroscopically measured redshift of $z = 1.227$.

Some of the candidate sources are recorded in existing catalogs of candidate blazars. Three objects (#6, #8, and #9) are reported in CGRaBS. Similarly, three objects (#1, #9, and #11) appear in WIBRaLS (R. D'Abrusco et al. 2014), a catalog of radio-loud candidate gamma-ray emitting blazars selected through the WISE mid-IR colors, with a strategy similar to the blazar strip selection adopted in Method 1 of Section 4. The corresponding identifiers are indicated as associations in Table 3. A third-party study of Fermi-LAT data focusing on subthreshold sources identifies two additional objects within the ROI (A. Sherman et al. 2026). The study highlights the Fermi object J0621.1-0610 as a candidate blazar, associated with a VLBI source already reported in the RFC. It did not meet the selection criteria of this work due to the lack of an X-ray counterpart, a VLBI flux density below 100 mJy and below 50% of the VLASS-measured (2–4) GHz flux of the source. It is, however, one of the targets of the VLBA observations reported in Table 1 (J0621-0609) and shows blazar-like properties.

5. Multiwavelength Properties of KM3-230213A Candidate Counterparts

The multiwavelength investigation reported in the following sections has two main goals. First, to characterize the electromagnetic properties of the 17 candidate counterparts. Second, to reduce the degeneracy in the potential associations by exploiting multiwavelength and time-domain information.

5.1. Variable or Flaring Behaviors

The remaining sample of candidate counterparts does not provide compelling evidence for a specific association due to the number of blazars within the 3° footprint. Brightness, spectrum, and time variability information are used to identify additional observational signatures that can reasonably be expected from a powerful neutrino source.

The 3° radius localization region of KM3-230213A contains 17 astronomical sources that are likely blazars (Section 4). Ten of them show strong radio emission on the parsec and subparsec scales (Section 4, Table 1), indicating strong jet beaming effects.

In addition, the temporal correlation between major flares and the neutrino arrival time has been analyzed as a key observable that can help select source associations. This observational approach was used in earlier studies, comparing radio flares with neutrino detections from IceCube, ANTARES, and Baikal-GVD (M. G. Aartsen et al. 2018; A. Plavin et al. 2020; T. Hovatta et al. 2021; A. Albert et al. 2024; V. A. Allakhverdyan et al. 2024; P. M. Kouch et al. 2024). There is growing evidence for neutrinos being produced during large electromagnetic flares.

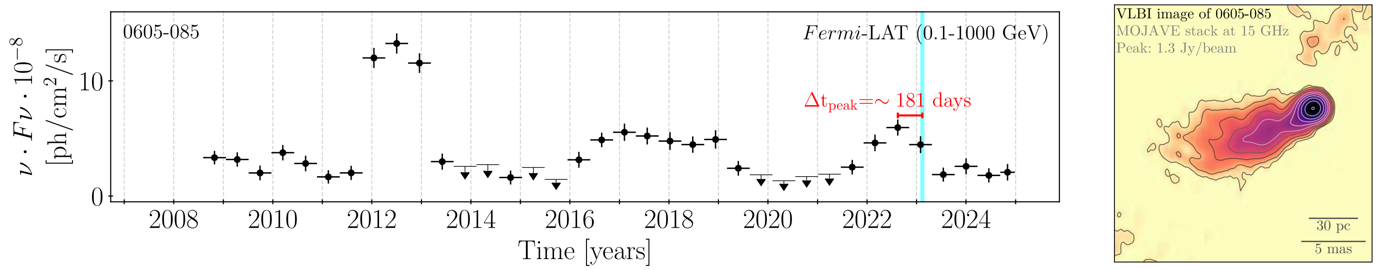

(a) The *Fermi*-LAT light curve and a VLBI image of 0605-085 (#6): the brightest radio source in the neutrino localization region that experiences a gamma-ray flaring activity around the neutrino arrival (Section 5.1.1). Δt_{peak} highlights the time difference of $\sim$ 181 days between the flare peak and the neutrino arrival time.

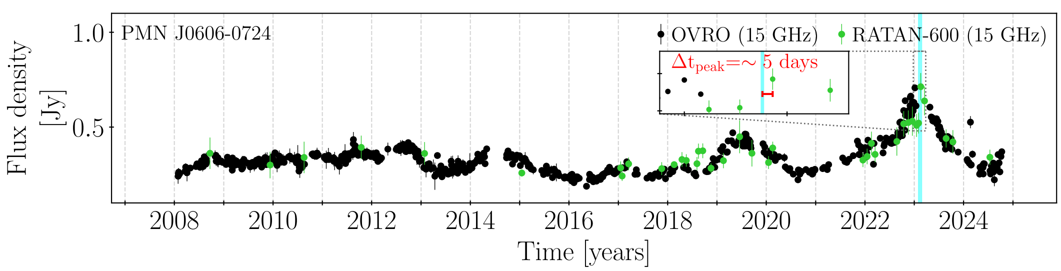

(b) The radio light curve for PMN J0606-0724 (#8) that experiences a major flare in close coincidence to the neutrino arrival (Section 5.1.2). Δt_{peak} highlights the time difference of $\sim$ 5 days between the flare peak and the neutrino arrival time.

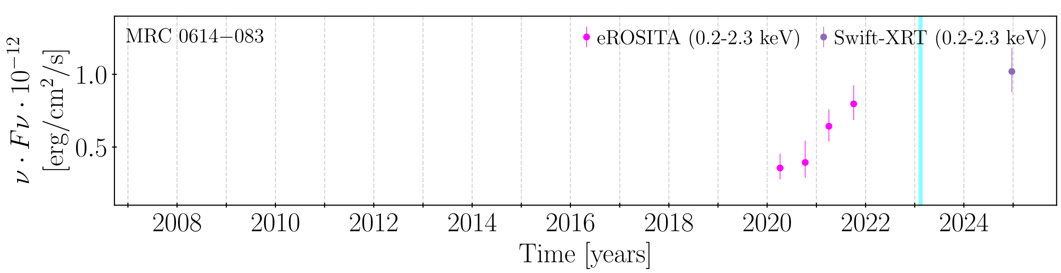

(c) The X-ray light curve for MRC 0614-083 (#1) that indicates a flaring activity around the neutrino arrival (Section 5.1.3).

Figure 4. Summary of observational properties related to the three most promising blazars associated with the KM3-230213A event. The cyan line highlights the arrival time of KM3-230213A in each light curve. The astronomical coordinates of these blazars are given in Table 3 and shown in Figure 3. Details on the observational data, along with multiwavelength light curves, are reported in Appendix A and Appendix C.

The most important results of the multiwavelength variability study are discussed in the following sections. While not unequivocal proof, highly variable electromagnetic emission could indicate a higher probability that the neutrino is associated with a specific source. In the following sections, three sources exhibiting flaring behavior are examined. Their properties in the electromagnetic band involved are summarized in Figure 4.

5.1.1. Source 0605-085: Brightest in Radio, Experiences Gamma-Ray Flaring Activity

Four known Fermi-LAT cataloged objects lie within the 90% confidence region of KM3-230213A. Among these, 0605-085 (#6) exhibits enhanced gamma-ray activity around the time of the detection of KM3-230213A (see Figure 4(a) and Appendix C), with a time difference of 181 days between the peak of the flare and the neutrino arrival time. The observed year-long flux enhancement exhibits a gradual increase and decrease in emission. Gamma-ray flaring activity has been previously used to pinpoint promising neutrino counterparts (M. G. Aartsen et al. 2018), but it may not be unusual for such trends to coincide with a neutrino event by chance.

The blazar 0605-085 is among the 50 brightest radio objects in the whole sky in terms of the VLBI flux density, indicating a high degree of relativistic beaming. The object's X-ray activity remains unconstrained due to a sparse observational coverage (see also Appendix A.3). The recent Swift-XRT ToO observation measured a flux consistent with historical values. At optical wavelengths, a high flux state is observed, temporally consistent with the gamma-ray flare. However, this has to be interpreted with caution, since the blazar is about 4″ away from a foreground star. Although the optical light curve for this blazar was constructed using data from ZTF and Gaia, which provide sufficient resolution to disentangle point sources separated by such distances, the possibility of residual contamination from the star affecting the optical light curve of the blazar should be further investigated. Theoretical modeling of the blazar jet suggests that 0605-085 multiwavelength features make it a viable source of UHE neutrinos (X. Rodrigues et al. 2026).

5.1.2. Major Radio Flare from PMN J0606-0724

Among the 17 candidate blazars, there are three radio-bright sources in the OVRO CGRaBS sample with dense uniformly sampled radio light curves (OVRO + RATAN; Appendix B). One of them, PMN J0606-0724 (#8), experiences a large radio flare very close in time to the KM3-230213A event, with a time difference of 5 days, see Figure 4(b) . In this scenario, a neutrino such as KM3-230213A could be produced by photohadronic interactions in the radio core of the blazar, without a significant associated gamma-ray signal (P. Kivokurtseva & S. Troitsky 2025). Such a coincidence is relatively uncommon. Thanks to the coverage of monitoring programs at OVRO and RATAN, a statistical evaluation of its chance probability is possible. The analysis is performed in Appendix B, and results in a pre-trial p-value of $p = 0.26\%$. This finding can be considered a hint of a possible association, consistent with a number of studies that find such associations in blazars (A. Plavin et al. 2020; T. Hovatta et al. 2021; R. Abbasi et al. 2023; A. Albert et al. 2024; P. M. Kouch et al. 2024). Given the a posteriori nature of this analysis, the exact probability should be interpreted with caution, as discussed in Section 6. This concerns the observed time delay of the radio peak coming five days after the neutrino arrival as well.

Another source, PMN J0616-1040, shows persistent rapid radio variability , indicative of a very compact ($\sim$10 μas) and bright structure probed by scattering of radio waves (J. Y. Koay et al. 2019). The corresponding light curves at radio and other available wavelengths are presented in Appendix C.

5.1.3. X-Ray Flaring Activity of MRC 0614-083

The X-ray band represents a valuable tracer of neutrino production in both jetted and non-jetted AGN. Previous studies have proposed an observable connection between neutrinos and X-ray emission in uniform samples of blazars and in individual sources such as TXS 0506+056 and NGC 1068 (V. S. Paliya et al. 2020; R. Abbasi et al. 2025; E. Kun et al. 2024; A. V. Plavin et al. 2024). Likewise, the potential of the X-ray band to reveal hadronic components in the spectral energy distribution of blazars has been previously shown in the study of the blazar 5BZB J0630-2406 (G. Fichet de Clairfontaine et al. 2023; J. M. Sanchez Zaballa et al. 2025, in preparation).

Of the 17 objects listed in Table 3, nine are detected at X-ray energies. The X-ray fluxes are integrated in the 0.2 −2.3 keV energy band, so that measurements across different facilities can be readily compared in the light curves. The eROSITA observations consist of four epochs in the period MJD 58677–59500 ($\sim$2 yr). Upon inspection of the eROSITA X-ray data for the candidate counterparts, only two objects are found to be variable: MRC 0614-083 (#1) and PMN J0616-1040 (#9). In addition, publicly available archival Swift-XRT observations suggest long-term variability for 0605-085 (#6).

ToO observations with Swift-XRT are performed for objects #1 and #6, on MJD 60666 and MJD 60669, respectively. The primary goal is to investigate X-ray year-long variability, albeit in a coarse manner, since nearly 2 yr have passed since the observation of KM3-230213A. The choice of the timescale is dictated, in this case, by data availability. The eROSITA sample only extends to $\sim$488 days before KM3-230213A, leaving a $\sim$3.2 yr gap between it and the new Swift-XRT observations.

Object #6 and object #9 show no remarkable X-ray flux enhancements at the observation epochs closest to the KM3NeT event. MRC 0614-083 (#1), which is the closest to the best-fit neutrino localization, displays X-ray activity that increases steadily in the years leading up to the KM3NeT event (see Figure 4(c) and Appendix C). The recent Swift follow-up indicates that the high X-ray state of the object persists. This suggests the intriguing possibility that KM3-230213A occurs while the object is undergoing an X-ray enhancement. Theoretical modeling of the multiwavelength behavior of this source across the optical, IR, and X-ray bands suggests that a super-Eddington accretion flare may be at the origin of the KM3NeT event (C. Yuan et al. 2026).

5.2. The Nature of 4FGL J0616.2-0653: Pointlike Source or Extended Diffuse Emission?

The unidentified, cataloged object 4FGL J0616.2-0653 (#2) lacks a confident counterpart at other wavelengths. The Fermi-LAT analysis of the region reveals other mild excess gamma-ray emission, most of which appears to be extended and diffuse. The best-fit coordinates of 4FGL J0616.2-0653 are R.A. = $94\overset{\circ}{.}06$, decl. = $-6\overset{\circ}{.}90$ (J2000). Within the 95% gamma-ray error region of $0\overset{\circ}{.}09$, no counterparts are found. The closest radio source, NVSS J061633-064804, is $0\overset{\circ}{.}12$ from the best-fit position of the Fermi-LAT object, outside of the 95% error region. While the radio object is one of the targets of the VLBA observation (J0616-0648, Table 1), with an indication of a blazar nature, it is not included in the selection of candidates due to its relatively low radio flux density and low estimate of the lower limit of the brightness temperature. The 4FGL-DR4 catalog reports a tentative association of 4FGL J0616.2-0653 with an object that appears in the third EGRET catalog (R. C. Hartman et al. 1999). The EGRET source, 3EG J0616−0720, is located at R.A., decl. = (94.16, −7.35), with a positional uncertainty of $0\overset{\circ}{.}91$ (95% positional error). With a separation of $0\overset{\circ}{.}46$, 3EG J0616-0720, classified as an unidentified object, is positionally consistent with 4FGL J0616.2-0653. J. M. Casandjian & I. A. Grenier (2008) excluded 3EG J0616-0720 from the EGRET Revised source list due to additional structure observed in the interstellar medium. The lack of convincing counterparts at different wavelengths (radio, IR, optical, and X-ray) does not support the hypothesis of a pointlike origin for 4FGL J0616.2-0653. Furthermore, the excess emission does not appear to be isolated, but rather part of a larger continuous region with an arc-like morphology associated with the Orion molecular clouds (M. Ackermann et al. 2012), as evident from the TS map of the ROI (see Appendix A.4). Based on these results, mismodeled diffuse emission may explain the observed gamma-ray excess.

6. Discussion

Due to the size of the neutrino direction uncertainty region, comprising 17 candidate blazars, it is not possible to conclusively associate the neutrino with a specific source. The temporal correlations reported in Section 5.1 and Figure 4 could arise by chance as well. While blazars are here considered the most promising sources for neutrinos at these energies, the broader population of AGN may harbor other candidate counterparts. A radio survey conducted with ASKAP and VLASS highlights three nonblazar radio sources in the region, among which is an AGN (M. D. Filipović et al. 2025). The event may also originate from a cosmological population of transients, such as gamma-ray bursts (O. Adriani et al. 2026). A Galactic origin for KM3-230213A is, on the other hand, unlikely (O. Adriani et al. 2026a).

Among the temporal correlations that have been examined, only the chance probability for the major radio flare in PMN J0606-0724 is quantifiable in a robust way (Section 5.1.2). The observed close coincidence of such a flare with the neutrino (within five days) can arise by chance with the probability of $p = 0.26\%$. This correlation can be considered a hint of a possible association, especially in light of earlier studies on the blazar flare–neutrino connection. Flaring activity at gamma-ray and X-ray bands is observed in 0605-08 and MRC 0614-083, respectively; these coincidences are more common by chance, and their probabilities are not quantified here. Considering the a posteriori nature of the flare investigation, and the look-elsewhere effect arising from the exploration of time variability across multiple wavelengths, the p-value for the radio flare is interpreted as pre-trial. It serves the purpose of demonstrating that such a close coincidence by chance is rare, but far from impossible. These findings are not claimed as a statistically significant association.

The three cases of flaring sources discussed above do not exhibit strong and unequivocal correlations across different electromagnetic bands. However, if the neutrino was associated with one of such flares, the lack of correlated activity in other wavelengths would still be consistent with previous findings. As introduced in Section 4, the multiwavelength signatures of hadronic processes in blazars can be diverse. In the case of TXS 0506+056, while a single neutrino above 100 TeV was detected in the direction of the source while it was flaring in gamma rays, an additional neutrino excess at lower energies was observed during a gamma-ray quiet state (M. G. Aartsen et al. 2018; S. Garrappa et al. 2019). Theoretical efforts have addressed neutrino production under both flaring and nonflaring gamma-ray states (P. Padovani et al. 2019; M. Petropoulou et al. 2020; W. Winter et al. 2020).

From a phenomenological standpoint, the conditions required for a blazar to be the source of a muon neutrino with energy 72 PeV $\lesssim E_\nu \lesssim$ 2600 PeV can be evaluated. These neutrinos originate in the collisions of ultrarelativistic ions with protons at rest, or photons of sufficient energy. In both cases, the minimum energy required for a single proton is $E_p \sim 20 E_\nu \gtrsim 1.5$ EeV (E. Roulet & F. Vissani 2021). Such an energy is still significantly lower than the highest energies observed for cosmic-ray particles, ~300 EeV (D. J. Bird et al. 1995; Telescope Array Collaboration et al. 2023), for which the jets of AGN have already been proposed as possible sources (F. M. Rieger 2022). Assuming a rate of detected neutrino events from a single source at these energies is T^{-1}, the luminosity and the minimum jet power can be estimated. The effective area of ARCA with 21 lines at the most likely neutrino energy $E_\nu \simeq 220$ PeV is $A_{\rm eff} \sim 400\,{\rm m}^2$ (S. Aiello et al. 2025a). The likely counterparts with known redshift are located at $z \approx 1$ (Table 3; luminosity distance $d_L \approx 7$ Gpc), and these distances are also expected for neutrino associations from pure volume arguments. The emission can be enhanced with beaming effects by $f_{\rm beam}$—the beaming factor. For example, $f_{\rm beam} = 1$ for isotropic emission and $f_{\rm beam} \approx 10^3$ when the emission is concentrated within 4° around the jet direction. The latter is common for electromagnetic emission of blazars as shown by population studies (M. L. Lister et al. 2019). Together, this implies the source luminosity of

$$L_\nu = \frac{\Phi \cdot 4\pi d_L^2}{f_{\rm beam}} = \frac{E_\nu \cdot 4\pi d_L^2}{A \cdot T \cdot f_{\rm beam}} \approx \frac{1.5 \cdot 10^{49}\ {\rm erg\ s^{-1}}}{\frac{T}{yr} \cdot f_{\rm beam}}. \tag{1}$$

Following the energetics evaluations of O. Gottlieb & N. Globus (2021), the required power of the jet is at least

$$L_p \approx 5 L_\nu \approx \frac{7.5 \cdot 10^{49}\ {\rm erg\ s^{-1}}}{\frac{T}{\rm yr} \cdot f_{\rm beam}}. \tag{2}$$

The maximum feasible neutrino flux and rate for the power available in blazar jets can be estimated. Bright blazars are typically associated with the total jet power of $\sim 10^{45}\ {\rm erg\ s^{-1}}$. If most of this power is carried by protons, $L_p \sim 10^{45}\ {\rm erg\ s^{-1}}$, and $f_{\rm beam} = 10^3$, a neutrino of this energy could be detected by KM3NeT every $T = 75$ yr. For less pronounced beaming, the minimal T estimate would be higher. Note that this analysis is very optimistic: it only accounts for protons with this specific energy, ignoring the contribution of the remaining spectrum to L_p. Furthermore, not every proton at these energies produces a neutrino, as the efficiency depends on the target photon or proton field density. The observation of a single event has a very limited constraining power. If more neutrinos with these energies are detected from a single source in a time frame of years or decades, even the minimum power requirements would exceed those normally associated with blazars.

Alternatively, such neutrinos can come from many individual sources over the sky; these sources are likely to be at redshift $z \sim 1$ by the same volume arguments. The proton luminosity density associated with them can be estimated as

$$\mathcal{L}_p \sim 2 \cdot 10^{39}\ {\rm erg\ s^{-1}\ Mpc^{-3}} \tau^{-1}({\rm yr}), \tag{3}$$

where τ^{-1} is the total detection rate of neutrinos with these energies at KM3NeT. The isotropic flux of $\Phi^{1f}_{\rm sky} = 7.5 \times 10^{-10}\ {\rm GeV\ cm^{-2}\ s^{-1}\ sr^{-1}}$ estimated in KM3NeT Collaboration et al. (2025) corresponds to one event every $\tau = 62$ yr. This rate requires the luminosity density of $\mathcal{L}_p \sim 3 \cdot 10^{37}\ {\rm erg\ s^{-1}\ Mpc^{-3}}$. Such a $\mathcal{L}_p$ constitutes a fraction of a percent of the total AGN luminosity density, consistent with blazars being the sources of UHE neutrinos. This scenario is supported by a companion study showing that a population of blazars could power a diffuse flux compatible with the observation of the KM3NeT UHE event (O. Adriani et al. 2026b).

Another consideration is whether a blazar can accelerate particles to such high energies at all. A generic argument can be used to place another lower bound on the jet power required to accelerate a proton to an energy E_p (R. D. Blandford 2000, Globus and Blandford, ARAA submitted). Before creating the neutrino, the proton must have traversed a potential difference

$\gtrsim E_p/q = E_p$ (eV)$^{-1}$ V where q is its charge. In most models of acceleration, the effective impedance Z is a fraction of the impedance of vacuum, or $Z \sim 30\Omega$. This implies a minimum power requirement of $L_{\rm jet} > (E_p/q)^2 Z^{-1}$; for the neutrino energy in the hundreds of PeV, the requirement is $L_{\rm jet} > 10^{42}$ erg s^{-1}. Accelerating a small number of protons that can produce UHE neutrinos is not as challenging as accelerating to the highest observed cosmic-ray energy, ∼300 EeV. The acceleration timescale at these high energies will always be shorter than the light-crossing time across the jet and, in some scenarios, like relativistic magnetic reconnection, could be much shorter. Definite association of UHE neutrino events with fast flares in future observations would be more prescriptive.

7. Summary

In this paper, a multiwavelength observational study of blazar candidates as possible associations of the KM3NeT event KM3-230213A (S. Aiello et al. 2025a) is presented. Our work combines new dedicated observations with archival data across the electromagnetic spectrum to provide the most complete dataset available for these sources. In total, 17 likely blazar candidate sources are found within the 99% uncertainty region. Among them, the three most interesting candidates are highlighted in Figures 3 and 4:

1. Object MRC 0614-083 is the closest object, located 0°.6 away from the best-fit neutrino position, with indications of X-ray activity during the relevant period.
2. Object 0605-085 is among the 50 brightest blazars in the sky on parsec scales. Our data reveal a long-term gamma-ray flare peaking before the neutrino arrival.
3. Object PMN J0606-0724 exhibits a major radio flare, peaking at 15 GHz within 5 days of the neutrino arrival time. The pre-trial chance coincidence probability is estimated as 0.26%.

Based on these findings, the KM3NeT event KM3-230213A cannot be conclusively associated with enhanced multiwavelength emission from any single blazar. However, the hypothesis that the event originates from a blazar remains viable, with several blazar-like cataloged objects identified as potential counterparts in the neutrino field. Additionally, the event could potentially be associated with a population of faint and/or remote sources not individually resolved.

Improvements in the calibration of the KM3NeT telescope are expected to decrease systematic uncertainties in the directional reconstruction of KM3-230213A, thereby reducing the degeneracy in identifying possible counterparts. The comprehensive multiwavelength observational data presented in this work will be crucial for reliable candidate selection in future analyses, providing an essential baseline for understanding the electromagnetic behavior of these sources.

Acknowledgments

This work was supported by the European Research Council, ERC Starting grant MessMapp (PI: S.B.) under contract No. 949555. This work was funded by the European Union (ERC MuSES project No 101142396). The authors acknowledge the financial support of: KM3NeT-INFRADEV2 project, funded by the European Union Horizon Europe Research and Innovation Programme under grant agreement No 101079679; Funds for Scientific Research (FRS-FNRS), Francqui foundation, BAEF foundation. Czech Science Foundation (GACR 24-12702S); Agence Nationale de la Recherche (contract ANR-15-CE31-0020), Centre National de la Recherche Scientifique (CNRS), Commission Européenne (FEDER fund and Marie Curie Program), LabEx UnivEarthS (ANR-10-LABX-0023 and ANR-18-IDEX-0001), Paris I^le-de-France Region, Normandy Region (Alpha, Blue-waves and Neptune), France, The Provence-Alpes-Côte d'Azur Delegation for Research and Innovation (DRARI), the Provence-Alpes-Côte d'Azur region, the Bouches-du-Rhône Departmental Council, the Metropolis of Aix-Marseille Provence and the City of Marseille through the CPER 2021-2027 NEUMED project, The CNRS Institut National de Physique Nucléaire et de Physique des Particules (IN2P3); Shota Rustaveli National Science Foundation of Georgia (SRNSFG, FR-22-13708), Georgia;

The General Secretariat of Research and Innovation (GSRI), Greece; Istituto Nazionale de Fisica Nucleare (INFN) and Ministero dell'Università e della Ricerca (MUR), through PRIN 2022 program (Grant PANTHEON 2022E2J4RK, Next Generation EU) and PON R&I program (Avviso n. 424 del 28 febbraio 2018, Progetto PACK-PIR01 00021), Italy; IDMAR project Po-Fesr Sicilian Region az. 1.5.1; A. De Benedittis, W. Idrissi Ibnsalih, M. Bendahman, A. Nayerhoda, G. Papalashvili, I. C. Rea, A. Simonelli have been supported by the Italian Ministero dell'Università e della Ricerca (MUR), Progetto CIR01 00021 (Avviso n. 2595 del 24 dicembre 2019); KM3NeT4RR MUR Project National Recovery and Resilience Plan (NRRP), Mission 4 Component 2 Investment 3.1, Funded by the European Union—NextGenerationEU,CUP I57G21000040001, Concession Decree MUR No. n. Prot. 123 del 21/06/2022; Ministry of Higher Education, Scientific Research and Innovation, Morocco, and the Arab Fund for Economic and Social Development, Kuwait; Nederlandse organisatie voor Wetenschappelijk Onderzoek (NWO), the Netherlands; The grant "AstroCeNT: Particle Astrophysics Science and Technology Centre", carried out within the International Research Agendas program of the Foundation for Polish Science financed by the European Union under the European Regional Development Fund; The program: "Excellence initiative-research university" for the AGH University in Krakow; The ARTIQ project: UMO-2021/01/2/ST6/00004 and ARTIQ/0004/2021; Ministry of Research, Innovation and Digitalisation, Romania; Slovak Research and Development Agency under Contract No. APVV-22-0413; Ministry of Education, Research, Development and Youth of the Slovak Republic; MCIN for PID2021-124591NB-C41, -C42, -C43 and PDC2023-145913-I00 funded by MCIN/AEI/10.13039/501100011033 and by "ERDF A way of making Europe", for ASFAE/2022/014 and ASFAE/2022 /023 with funding from the EU NextGenerationEU (PRTR-C17.I01) and Generalitat Valenciana, for Grant AST22_6.2 with funding from Consejería de Universidad, Investigación e Innovación and Gobierno de España and European Union—NextGenerationEU, for CSIC-INFRA23013 and for CNS2023-144099, Generalitat Valenciana for CIDEGENT/2018/034, /2019/043, /2020/049, /2021/23, for CIDEIG/2023/20, for CIPROM/2023/51 and for GRISOLIAP/2021/192 and EU for MSC/101025085, Spain; Khalifa University internal grants (ESIG-2023-008, RIG-2023-070 and RIG-2024-047), United Arab Emirates; The European Union's Horizon 2020 Research and Innovation Programme

(ChETEC-INFRA—project No. 101008324). Views and opinions expressed are those of the author(s) only and do not necessarily reflect those of the European Union or the European Research Council. Neither the European Union nor the granting authority can be held responsible for them.

This work is supported by NSF grants AST2407603 and AST2407604. We thank the California Institute of Technology and the Max Planck Institute for Radio Astronomy for supporting the OVRO 40 m program under extremely difficult circumstances over the last 8 yr in the absence of agency funding. Without this private support, these observations could not have been made. We also thank all the volunteers who have enabled this work to be carried out. Prior to 2016, the OVRO program was supported by NASA grants NNG06GG1G, NNX08AW31G, NNX11A043G, and NNX13AQ89G from 2006 to 2016 and NSF grants AST-0808050 and AST-1109911 from 2008 to 2014.

K.T. acknowledges support from the European Research Council (ERC) under the European Union's Horizon 2020 research and innovation program under grant agreement No. 771282.

I.L, S.K., and AP were funded by the European Union under grants ERC-2022-STG–BOOTES-101076343.

W.M., R.R., B.M., and P.V.d.l.P. acknowledge support from ANID BASAL FB210003 (CATA). R.R., B.M., and P.V.d.l.P. acknowledge support from Núcleo Milenio TITANs (NCN2023_002). R.B. and N.G. acknowledge support by a grant from the Simons Foundation (00001470, R.B., N.G.). P.V.d.l.P. also acknowledges support by the National Agency for Research and Development (ANID)/Scholarship Program/Doctorado Nacional/2023–21232103.

T.H. acknowledges support from the Academy of Finland project Nos. 317383, 320085, 322535, and 345899.

The work by A.V. Popkov, Y.A.K., S.V.T., A.K.E, Y.V.S, and P.A.V. is supported in the framework of the State project “Science” by the Ministry of Science and Higher Education of the Russian Federation under the contract 075-15-2024-541.

A.V. Plavin is a postdoctoral fellow at the Black Hole Initiative, which is funded by grants from the John Templeton Foundation (grants 60477, 61479, 62286) and the Gordon and Betty Moore Foundation (grant GBMF-8273).

This research has made use of data and/or software provided by the High Energy Astrophysics Science Archive Research Center (HEASARC), which is a service of the Astrophysics Science Division at NASA/GSFC.

This research has made use of the NASA/IPAC Extragalactic Database, which is funded by the National Aeronautics and Space Administration and operated by the California Institute of Technology. Part of this work is based on archival data, software, or online services provided by the Space Science Data Center–ASI.

This work made use of the Swinburne University of Technology software correlator, developed as part of the Australian Major National Research Facilities Programme and operated under license (A. T. Deller et al. 2011).

This work is partly based on the data obtained with the RATAN-600 radio telescope at the Special Astrophysical Observatory of the Russian Academy of Sciences (SAO RAS).

The National Radio Astronomy Observatory is a facility of the National Science Foundation operated under cooperative agreement by Associated Universities, Inc.

This research has made use of data from the Radio Fundamental Catalog (RFC; 10.25966/dhrk-zh08, L. Y. Petrov & Y. Y. Kovalev 2025).

This research has made use of data from the MOJAVE database that is maintained by the MOJAVE team (M. L. Lister et al. 2018). This paper makes use of the following ALMA data: ADS/JAO.ALMA#2011.0.00001.CAL. ALMA is a partnership of ESO (representing its member states), NSF (USA) and NINS (Japan), together with NRC (Canada), NSTC and ASIAA (Taiwan), and KASI (Republic of Korea), in cooperation with the Republic of Chile. The Joint ALMA Observatory is operated by ESO, AUI/NRAO, and NAOJ. This publication makes use of data products from the WISE, which is a joint project of the University of California, Los Angeles, and the Jet Propulsion Laboratory/California Institute of Technology, funded by the National Aeronautics and Space Administration.

This work presents results from the European Space Agency (ESA) space mission Gaia. Gaia data are being processed by the Gaia Data Processing and Analysis Consortium (DPAC). Funding for the DPAC is provided by national institutions, in particular the institutions participating in the Gaia MultiLateral Agreement (MLA). The Gaia mission website is https://www.cosmos.esa.int/gaia. The Gaia archive website is https://archives.esac.esa.int/gaia.

This work has made use of data from the Asteroid Terrestrial-impact Last Alert System (ATLAS) project. The Asteroid Terrestrial-impact Last Alert System (ATLAS) project is primarily funded to search for near-earth asteroids through NASA grants NN12AR55G, 80NSSC18K0284, and 80NSSC18K1575; by-products of the NEO search include images and catalogs from the survey area. This work was partially funded by Kepler/K2 grant J1944/80NSSC19K0112 and HST GO-15889, and STFC grants ST/T000198/1 and ST/S006109/1. The ATLAS science products have been made possible through the contributions of the University of Hawaii Institute for Astronomy, Queen’s University Belfast, the Space Telescope Science Institute, the South African Astronomical Observatory, and The Millennium Institute of Astrophysics (MAS), Chile.

This work is based on observations obtained with the Samuel Oschin Telescope 48 inch and the 60 inch Telescope at the Palomar Observatory as part of the ZTF project. ZTF is supported by the National Science Foundation under grant No. AST-2034437 and a collaboration including Caltech, IPAC, the Weizmann Institute for Science, the Oskar Klein Center at Stockholm University, the University of Maryland, Deutsches Elektronen–Synchrotron and Humboldt University, the TANGO Consortium of Taiwan, the University of Wisconsin at Milwaukee, Trinity College Dublin, Lawrence Livermore National Laboratories, and IN2P3, France. Operations are conducted by COO, IPAC, and UW.

We acknowledge the use of public data from the Catalina Real-Time Transient Survey.

This work is partly based on data from eROSITA, the soft X-ray instrument aboard SRG, a joint Russian-German science mission supported by the Russian Space Agency (Roskosmos), in the interests of the Russian Academy of Sciences represented by its Space Research Institute (IKI), and the Deutsches Zentrum für Luft- und Raumfahrt (DLR). The SRG spacecraft was built by Lavochkin Association (NPOL) and its subcontractors, and is operated by NPOL with support from the Max Planck Institute for Extraterrestrial Physics (MPE). The development and construction of the eROSITA X-ray instrument was led by MPE, with contributions from the Dr. Karl Remeis Observatory Bamberg & ECAP (FAU Erlangen-Nuernberg), the University of Hamburg Observatory, the Leibniz Institute for Astrophysics Potsdam (AIP), and the Institute for Astronomy and Astrophysics of the University of Tübingen, with the support of DLR and the Max Planck Society. The Argelander Institute for Astronomy of the University of Bonn and the Ludwig Maximilians Universität Munich also participated in the science preparation for eROSITA. The eROSITA data shown here were processed using the eSASS software system developed by the German eROSITA consortium. We thank the Swift PI, the Observation Duty Scientists, and the science planners for promptly approving and executing our Swift observations (ObsID: 18990, ObsID: 36371). We acknowledge the use of public data from the Neil Gehrels Swift Observatory data archive.

This research has made use of data obtained from the Chandra Data Archive and the Chandra Source Catalog, both provided by the Chandra X-ray Center (CXC). This paper employs a list of Chandra datasets, obtained by the Chandra X-ray Observatory, contained in the Chandra Data Collection doi: 10.25574/cdc.447."

We acknowledge the use of public data from the ROSAT survey. The ROSAT project is supported by the German Bundesministerium für Bildung, Wissenschaft, Forschung und Technologie (BMBF/DARA) and the Max-Planck-Society.

This work was supported by CNES, focused on SVOM. The SVOM is a China-France joint mission led by the Chinese National Space Administration (CNSA), French Space Agency (CNES), and the Chinese Academy of Sciences (CAS), which is dedicated to observing gamma-ray bursts and other transient phenomena in the energetic universe.

The Fermi-LAT Collaboration acknowledges generous ongoing support from a number of agencies and institutes that have supported both the development and the operation of the LAT as well as scientific data analysis. These include the National Aeronautics and Space Administration and the Department of Energy in the United States, the Commissariat à l'Energie Atomique and the Centre National de la Recherche Scientifique/Institut National de Physique Nucléaire et de Physique des Particules in France, the Agenzia Spaziale Italiana and the Istituto Nazionale di Fisica Nucleare in Italy, the Ministry of Education, Culture, Sports, Science and Technology (MEXT), High Energy Accelerator Research Organization (KEK) and Japan Aerospace Exploration Agency (JAXA) in Japan, and the K. A. Wallenberg Foundation, the Swedish Research Council and the Swedish National Space Board in Sweden. Additional support for science analysis during the operations phase is gratefully acknowledged from the Istituto Nazionale di Astrofisica in Italy and the Centre National d'Études Spatiales in France. This work was performed in part under DOE contract DE-AC02-76SF00515.

Facilities: KM3NeT:ARCA, VLA, VLBA, RATAN, OVRO:40m, Swift, Fermi, eROSITA, Gaia, SO:Schmidt, ATLAS, PO:1.2m, WISE, NEOWISE, CXO, ROSAT.

Appendix A Multiwavelength Data

In the following sections, the analysis procedures for the different collected data are described.

A.1. Radio Data

A.1.1. VLBI and Parsec-scale AGN Jets

This paper utilizes both archival and new dedicated VLBI observations. Archival measurements are used in Section 4 in the form of the RFC (L. Y. Petrov & Y. Y. Kovalev 2025) that catalogs a complete uniform all-sky sample of VLBI-bright sources, dominated by blazars. Further, a VLBI image from the MOJAVE (Monitoring Of Jets in AGN with VLBA Experiments; M. L. Lister et al. 2018) is used for illustration of the parsec-scale structure in Figure 4.

VLBA data analysis procedure. A priori amplitude, phase, and bandpass calibration are performed in `AIPS` (E. W. Greisen 2003). For comparison, an independent a priori calibration using `rPicard/CASA` (M. Janssen et al. 2019) is performed, obtaining consistent results, with `rPicard`-calibrated correlated flux densities being systematically 12% lower. Radio frequency interference partially affects the data in the 7.6 GHz sub-band, which is marked manually in `AIPS` and automatically in `rPicard`. The `PIMA` software (L. Petrov et al. 2011) is used to evaluate the probability of false positives and the detection sensitivity. The detection limit is found to be about 6 mJy, which is in agreement with the expectations from thermal noise.

Automated hybrid imaging is performed, applying self-calibration and CLEAN imaging to the `AIPS`-calibrated data in `difmap` (M. C. Shepherd 1997; T. J. Pearson & A. C. S. Readhead 1984). The phase self-calibration solution interval is limited to 12 s to avoid creating a "fake" signal from noise, following A. V. Popkov et al. (2021). Most of the sources are slightly resolved, and the properties of their structure are measured by fitting the source structure with two circular Gaussian components directly to the self-calibrated visibility data. The resulting primary blazar candidates among the observed VLBA targets within the KM3-230213A localization region are shown, in addition to RFC-selected objects, in Figure A1.

A.1.2. OVRO 40 m

The OVRO 40 m Telescope has been dedicated to monitoring a carefully selected sample of 1158 blazars on a (3–4) day cadence since 2008 January, using symmetrical off-axis dual-beam optics in double switching mode to minimize atmospheric effects. The details of the observing method, data reduction, and observations are given in A. C. S. Readhead et al. (1989) and J. L. Richards et al. (2011). The cryogenic receiver is centered at 15 with a 2 GHz equivalent noise bandwidth.

The quasar 3C 286 is used for absolute flux density calibration, with an assumed value of 3.44 Jy (J. W. M. Baars et al. 1977). Occasionally, the molecular cloud DR 21 is used, calibrated relative to 3C 286 using early OVRO 40 m data. A temperature-stabilized noise diode is used to compensate for gain drifts.

The sample of OVRO sources used for the temporal analysis in Appendix B is the CGRaBS sample north of decl. -20° (S. E. Healey et al. 2008). CGRaBS is a catalog of AGN with radio and X-ray properties similar to EGRET gamma-ray blazars, selected from a parent population of flat-spectrum radio sources ($\alpha > -0.5$) with 4.8 GHz flux density >65 mJy. After removing J1310+3233, a faint target that suffers from

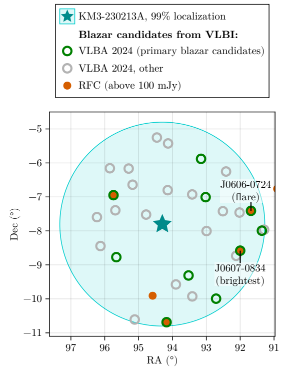

Figure A1. Likely blazar candidates within the KM3-230213A 99% localization area, based on their parsec-scale radio emission properties. See Table 3 and Appendix A.1.1 for details. Two blazars are labeled in the plot: PMN J0606-0724 exhibits the strongest temporal correlation of radio flares to the neutrino arrival (analyzed in Appendix B); 0605-085 is the brightest in terms of parsec-scale emission.

confusion with a bright nearby source, the sample used in this paper is reduced to 1157 objects.

A.1.3. RATAN-600

The RATAN-600[156] observations of broadband radio spectra in the meridian transit mode are used. They cover six frequency bands: 0.96/1.2, 2.3, 4.7, 7.7/8.2, 11, and 22 GHz, quasi-simultaneously across the different bands, within 3–5 minutes (Y. N. Parijskij 1993). Ten flux density calibrators are used to construct multifrequency calibration curves covering the decl. range between −35° and +45°: J0025 −26, J0137+33, J0240−23, J0521+16, J0627−05, J1154 −35, J1331+30 (3C 286), J1347+12, J2039+42 (DR 21), and J2107+42 (NGC 2027) (J. W. M. Baars et al. 1977; M. Ott et al. 1994; K. D. Aliakberov et al. 1985; R. A. Perley & B. J. Butler 2013, 2017). Details of the RATAN-600 antenna, radiometers, and data reduction are presented in Y. Y. Kovalev et al. (1999); P. G. Tsybulev (2011), R. Y. Udovitskiy et al. (2016), P. G. Tsybulev et al. (2018), Y. V. Sotnikova (2020). RATAN-600 performs long-term monitoring of a complete sample of about 600 AGN with VLBI correlated flux density > 400 mJy at 8 GHz from the RFC catalog at a cadence of about 3 months.

In this work, the quasi-simultaneous multifrequency RATAN-600 data are interpolated to 15 GHz for use in the time-dependent analysis together with OVRO 15 GHz measurements. The interpolation uses a power law between 22 GHz and the nearest of the lower RATAN-600 frequencies (11, 8, or 5 GHz) for each observation epoch. The correction for different amplitude scales between telescopes is performed by normalizing the interpolated RATAN-600 fluxes by their median ratio to the OVRO measurements. The correction factor is within ∼10% for all sources. For use in the analysis, the RATAN-600 data *are restricted* to the time period from 2008 January to be consistent with the OVRO light-curve coverage (Appendix A.1.2).

A.1.4. ALMA

The calibrator source catalog of ALMA is a comprehensive database of astronomical measurements of calibrator sources frequently observed for calibration purposes. The catalog includes observations for three sources, with data available across three receiver bands (Bands 3, 6, and 7, corresponding to 84–116 GHz, 211–275 GHz, 275–373 GHz), providing additional variability information.

A.1.5. University of Michigan Radio Astronomy Observatory

Data from the University of Michigan Radio Astronomy Observatory (UMRAO; H. D. Aller et al. 1985; M. F. Aller et al. 2014) are provided by M. Aller (private communication), supplementary to the 15 GHz data for 0605-085 (#6) from OVRO and RATAN-600.

A.2. IR and Optical Data

Archival data in optical and IR wavelengths are collected for the sources highlighted in Table 3. In the IR, observations performed with WISE (E. L. Wright et al. 2010) and the reactivated mission NEOWISE (A. Mainzer et al. 2011) between 2009 and 2024 are used. Both missions observe magnitudes in the W1 (3.4 μm) and W2 (4.6 μm) bands for all sources with WISE counterparts in Table 3. As some sources are observed multiple times per day, the weighted mean of the magnitudes is taken for further processing on each observation day. Magnitudes are then transformed to flux units using the corresponding filter curves and zero-points (T. H. Jarrett et al. 2011). Similarly, optical light curves are gathered for multiple sources using publicly available data from various facilities. The Asteroid Terrestrial-impact Last Alert System (ATLAS; J. L. Tonry et al. 2018; K. W. Smith et al. 2020; A. N. Heinze et al. 2018) observes the cyan (c) and orange (o) filter bands. The 5σ limiting magnitudes are at $m = 19.7$. The filter specifications and zero-points are provided by the Spanish Virtual Observatory (SVO) Filter Profile Service (C. Rodrigo et al. 2012; C. Rodrigo & E. Solano 2020), in addition to the mission publications. The Catalina Realtime Transient Survey (CRTS; A. J. Drake et al. 2009) observed the sky region at this decl. with two out of three telescopes, Catalina Sky Survey (CSS) and Siding Spring Survey (SSS). Both provide magnitudes close to the *V*-band (UBV photometric system) with magnitude limits of $m = 19.5$ (CSS) and $m = 19.0$ (SSS). For times between 2014 and 2017, Gaia (Gaia Collaboration et al. 2016, 2023; C. Babusiaux et al. 2023) provides observations in three custom filters. The filter information and zero-points for the G, $G_{\rm BP,}$ and $G_{\rm RP}$ bands are available in M. Riello et al. (2021). Lastly, observations taken with the ZTF (F. J. Masci et al. 2018) are available in the red (r) and the green (g) band, with filter information available in SVO. Note that all magnitudes are corrected for galactic extinction using the source-dependent $E(B - V)$ value from E. F. Schlafly & D. P. Finkbeiner (2011) and following the extinction law of E. L. Fitzpatrick (1999) before the conversion to flux units.

A.2.1. WISE "Blazar Strip" Selection

The population of gamma-ray blazars has been shown to follow a specific distribution in its IR observable properties (F. Massaro et al. 2012). In particular, the infrared color–color diagrams evaluated from all four WISE observation bands are used to build a selection of blazar-like candidates. Given W1, W2, W3, and W4, the WISE bands at 3.4, 4.6, 12, and 22 μm, respectively, the selection is performed in the three-dimensional space where the axes are defined by the colors: W1–W2,

[156] in Russian, РАТАН-600——радиоастрономический телескоп Академии наук, Radio Telescope of the Academy of Sciences.

W2–W3, W3–W4. This classification is statistical in nature. Since the selection adopted in this work is enhanced by the detection of an X-ray counterpart, a 40% extension of the contour area has been applied to select the candidates reported in Table 3.

A.3. X-Ray Observations

Publicly available archival data for the sources in the sample are collected. Of the 17 candidate sources, five (sources #1, #6, #7, #10, and #17) have archival data from the Neil Gehrels Swift Observatory (Swift), Chandra X-ray Observatory (Chandra), and/or ROSAT. In particular, 0605-085 #6 has been observed most extensively, with data from 1990 to 2008 from all of the above instruments. In addition, proprietary data from the SRG observatory, in particular from the eROSITA instrument, are collected and analyzed for the available sources. In addition to the archival observations, a ToO request with Swift was submitted to observe sources #1 and #6. The SVOM satellite has been used to observe the 90% uncertainty region using a tiling pattern. The procedures used to estimate the flux for each instrument, as well as the pipeline used for data analysis, are illustrated in the following sections. For all observations, the intrinsic flux is calculated assuming a power-law model with galactic absorption, unless stated differently. The estimated fluxes are shown in Table 2.

A.3.1. ROSAT

ROSAT performed the first imaging X-ray survey of the entire sky between 1990 and 1991. In the following years, until 1999, ROSAT entered the pointed observing phase, during which more than 100,000 sources were cataloged (W. Voges et al. 1999). Among the sample of 17 blazar-like candidate sources, NVSS J061703−082225 (1RXS J061702.4−08222; 8″.2 offset from optical coordinates) and RFC J0607−0834 (1RXS J060758.7−08344; 14″.9 offset from optical coordinates) have been included in the ROSAT All-Sky Survey Faint Source Catalog (W. Voges et al. 2000). With count rates of $(1.16 \pm 0.57) \times 10^{-2}\,\mathrm{s}^{-1}$ and $(1.71 \pm 0.68) \times 10^{-2}\,\mathrm{s}^{-1}$, and hardness ratios of 0.68 ± 0.73 and 1.00 ± 0.44, for NVSS J061703−082225 and RFC J0607−0834, respectively, the intrinsic flux in the (0.1–2.0) keV band is estimated. This is done using the count rate-to-energy flux conversion formula presented in the literature (J. H. M. M. Schmitt et al. 1995).

NVSS J060639-063421 (#10) has been cataloged in WGACAT, a comprehensive catalog derived from all ROSAT position sensitive proportional counter pointed observations (N. E. White et al. 2000). The source is designated 1WGA J0606.6−0633, located at 28″.9 from the optical coordinates, with a count rate of $(2.99 \pm 0.76) \times 10^{-2}\,\mathrm{s}^{-1}$. WGACAT provides a variety of processed data products for each source, including smoothed intensity images, timing images, light-curve plots, and both source and background spectra. For this object, the available source spectrum is extracted using an optimized box size, along with an additional response file generated using the `pcarf` software (J. K. Blackburn 1995). The corresponding response matrix, background spectrum, and ancillary response file are processed with `XSPEC` to estimate the flux in the (0.2–2.3) keV band.

A.3.2. Swift-XRT

As mentioned above, some of the candidates were previously observed with the Swift observatory (N. Gehrels et al. 2004) in addition to the requested observations. The X-ray data from Swift-XRT (D. N. Burrows et al. 2005) are processed using `FTOOLS`, part of the `HEASoft` package (v6.33), designed for manipulating and analyzing FITS files. For this analysis, all Swift-XRT observations were performed in photon counting mode. The event files are cleaned and calibrated using standard filtering criteria via the `xrtpipeline` task, using the latest files from the Swift`CALDB` provided by `HEASARC`.

The spectral extraction for events in the (0.3–10.0) keV energy range is performed using the `XSELECT` tool. The source signal was extracted from a circular region with a radius of 20 pixels (47″), corresponding to about 90% of the XRT PSF, after visually centering the extraction region at the coordinates of the radio counterpart. The background spectrum was derived from an annular region centered on the optical coordinates of the source, with an inner radius of 40 pixels (∼1′.5) and an outer radius of 80 pixels (∼3′.1). For proper spectral modeling, the binning is set to at least 1 count per spectral channel, which allows the use of C-statistics (W. Cash 1979) in `XSPEC`.

A.3.3. eROSITA

The SRG observatory (R. Sunyaev et al. 2021) is equipped with two main instruments: eROSITA and ART-XC. eROSITA is a groundbreaking instrument for surveying the entire sky in soft X-rays, operating at energies between 0.2 and 8 keV. It offers significant advancements compared to earlier facilities like ROSAT, with improvements in parameters such as effective area, vignetting function, and PSF (P. Predehl et al. 2021).

Using the SRG/eROSITA all-sky survey, an investigation was conducted within a $6 \times 6\,\mathrm{deg}^2$ error box around KM3-230213A, focusing only on X-ray point sources. By analyzing the list of potential HE counterparts to the neutrino event and matching them to within 15″ of the eROSITA positions, 11 out of 17 sources align.

For these sources, spectra are extracted from the pipeline-processed eROSITA event files (version 020). Events from all seven telescope modules of eROSITA and from all four completed eROSITA All Sky Survey iterations (eRASS:4) are combined. The SRCTOOL task of the eROSITA Science Analysis Software System (eSASS) is used to produce source and background spectra, ancillary response files (ARFs), and response matrix files (RMFs). This is done by extracting source counts from circular regions with radii of 60″ and background counts from large and nearby regions. For the remaining counterparts to the neutrino event that did not match a point source with eROSITA, the upper limits were extracted from the work in D. Tubín-Arenas et al. (2024).

The eRASS:4 spectra were analyzed with the Bayesian X-ray Analysis software version 4.1.2 (J. Buchner et al. 2014), which connects the nested sampling algorithm `UltraNest` (J. Buchner 2019, 2021) with the fitting environment `CIAO/Sherpa` (A. Fruscione et al. 2006). Spectra were fit using an unbinned approach and the C-statistic. The fitting procedure included a principal component analysis-based background model (C. Simmonds et al. 2018) derived from a large sample of eROSITA background spectra. For all spectra, a power-law model (`powerlaw`) is fitted, including the contribution of Galactic absorption through the component TBABS, using the Galactic column density estimated by the HI4PI Collaboration (HI4PI Collaboration et al. 2016).

Variability across different eROSITA epochs is examined by comparing the cataloged (0.2−2.3) keV flux values of the individual eRASS surveys (eRASS1 to 4; A. Merloni et al. 2024). To identify variable sources, the maximum amplitude variability and its significance are evaluated following the definitions of T. Boller et al. (2016). Two sources are identified as variable between eRASS surveys with a significance $>2\sigma$ (MRC 0614-083 and PMN J0616-1040). For these, a time-resolved spectral analysis is performed by applying the same prescriptions as above to the individual eRASS surveys.

A.3.4. Chandra

From the sample of candidates, the blazar 0605-085 (#6) stands out for its three observations with Chandra. These were made with the Advanced CCD Imaging Spectrometer (ACIS-S) spectroscopic array between 2001 and 2009 (M. C. Weisskopf et al. 2000). These observations are analyzed using the `chandra_repro` script within the `CIAO` data analysis system (A. Fruscione et al. 2006), version 4.16, along with the Chandra `CALDB` version 4.11.5. The spectra are extracted using the `specextract` tool provided in the `CIAO` software suite. In particular, a visual analysis of the reprocessed imaging event file was done to select the region for both the source and the background. For the background, an annular area was utilized, centered on the given coordinates, with an inner radius of 6″ and an outer radius of 20″. Conversely, a circular region of approximately 5″ was selected for the source, deliberately positioned to exclude the nearby foreground star from being included in the selection. As with the rest of the observations, the spectra are binned to ensure one count per bin to be further modeled with `XSPEC`.

A.4. Gamma-Ray Data from Fermi-LAT

Available Fermi-LAT data are analyzed using the Python package `fermipy` (M. Wood et al. 2017). The ROI is centered at the best-fit position of KM3-230213A and selected photons from the `Pass 8 SOURCE` class (W. Atwood et al. 2013; P. Bruel et al. 2018) within a $10° \times 10°$ square ROI. The analysis covered the period from 2008 August 4 to 2025 January 11 (MJD 54682 – 60357).

To minimize contamination from gamma rays produced in the Earth's upper atmosphere, a zenith angle cut of $\theta < 90°$ is applied. The standard data quality cuts (DATA_QUAL > 0) $\&\&$(LAT_CONFIG $==$ 1) are applied, and periods coinciding with solar flares and gamma-ray bursts detected by Fermi-LAT are excluded. The ROI model included all 4FGL Data Release 4 catalog sources (4FGL-DR4; J. Ballet et al. 2023) located within 15° of the ROI center, as well as galactic and isotropic diffuse emission models[157] (`gll_iem_v07.fits` and `iso_P8R3_SOURCE_V2_v1.txt`).

A binned likelihood analysis over the (0.1−1000) GeV energy range is performed, using 10 bins per decade in energy and 0°.1 spatial bins. The `P8R3_SOURCE_V3` instrumental response functions (IRFs) are adopted.

[157] LAT Background Models

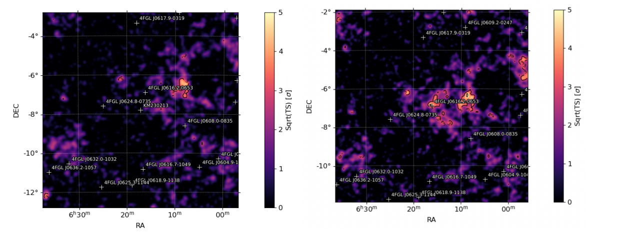

Figure A2. Fermi-LAT TS map (> 0.1 GeV) of the ROI, integrating ∼16 yr of observations. Left: The ROI analysis is centered on the best-fit position of KM3-230213A, and includes all 4FGL-DR4 cataloged sources present in the ROI. Right: the ROI analysis is centered on the position of 4FGL J0616.2-0653, where the source is excluded from the model of the region, to better visualize the excess emission associated with it. A mild excess of gamma-ray emission is visible in the ROI, most of which appears to be extended and diffuse. The observed larger continuous region with an arc-like morphology may originate from the mismodeled diffuse emission of the Orion molecular clouds. See also Section 5.2.

To model a putative point source at the KM3-230213A best-fit position, a power-law spectrum with a fixed index of 2.0 is used. In the fit, the spectral shapes and parameters reported in the 4FGL-DR4 catalog for all sources in the ROI are adopted. First, a fit of the ROI is performed by means of the `fermipy` method "optimize" to ensure that all spectral parameters are close to their global likelihood maxima. This is done by iteratively optimizing the components of the ROI model in sequential steps, starting from the largest components.[158] As discussed in Sections 3.4 and 5.2, the maximum-likelihood analysis of the Fermi-LAT data includes the generation of TS maps to identify previously uncataloged sources and to investigate the origin of the observed gamma-ray excess. The resulting TS maps are presented in Figure A2.

A.4.1. Gamma-Ray Analysis of KM3-230213A Candidate Counterparts

For each object listed in Table 3, the analysis described in the previous section is performed. In addition, to characterize their variability properties, Fermi-LAT light curves are generated with 6 month bins. For the likelihood fits of the time bins, the best-fit ROI model obtained from the full time interval analysis is adopted.

First, a fit is attempted by allowing variations in the normalization of the target source, all sources within the inner 3° of the ROI, and the diffuse components. If the fit does not converge, the number of free parameters is iteratively restricted until a successful fit is obtained. This procedure begins by fixing the sources in the ROI that are most weakly detected, starting at TS <4. Next, sources with TS <9 are fixed, followed by sources up to 1° from the ROI center and those with TS <25. Finally, all parameters except the normalization of the target source are fixed.

The target source is considered as detected if TS >9 in the corresponding time bin. If this condition is not met, a 95% confidence limit is reported, denoted by down-pointing arrows in the gamma-ray light curves.

Appendix B
Neutrino-radio Flare Association Probability

A statistical analysis to test the association between neutrino arrival times and major blazar radio flares is performed in this

[158] https://fermipy.readthedocs.io/en/latest/fitting.html

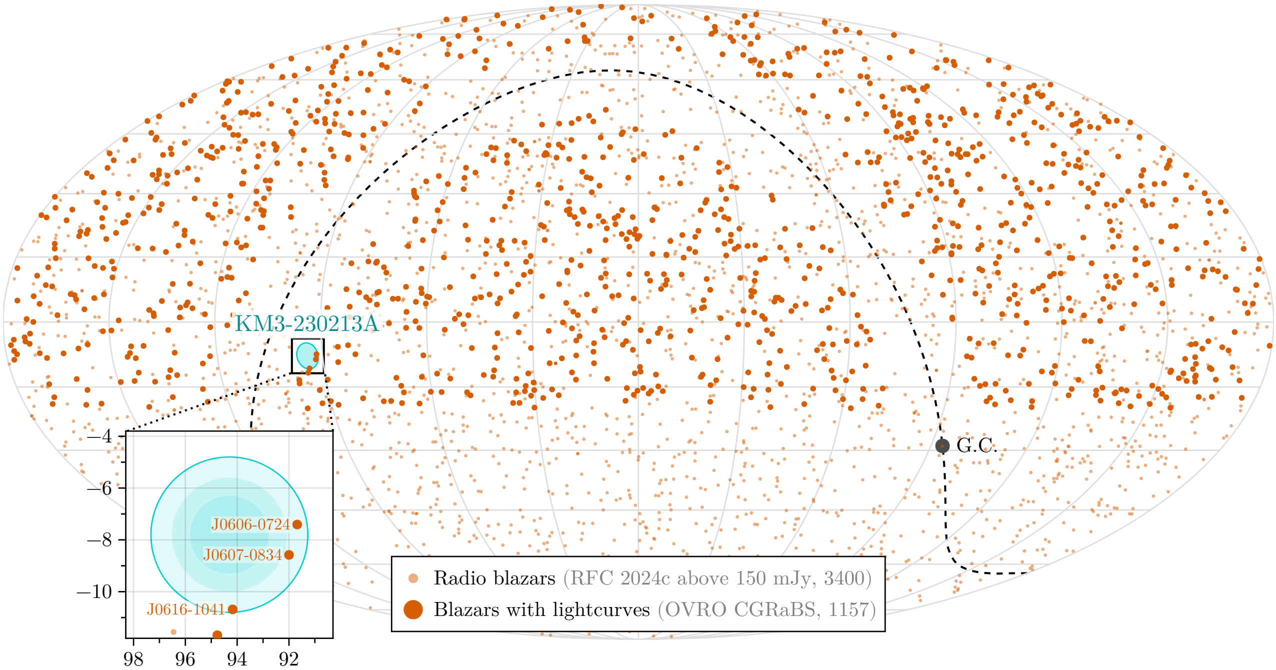

Figure B1. The KM3-230213A localization in the sky (68%, 90%, and 99% containment areas shaded in cyan) together with the RFC bright (above 150 mJy) sources (A.1.1), displayed along with the sources monitored by the OVRO program (A.1.2). The direction of the event is close to the boundary of the OVRO monitoring area, ±10° from the Galactic plane (dashed black line). All bright radio blazars in this region are in the CGRaBS sample and have radio light curves available.

section. This consists of an evaluation of the chance probability of finding, in a 3° circular region, a blazar with a time correlation as strong as the one observed in the data (Section 5.1.2). For this purpose, only blazars in the OVRO CGRaBS monitoring programs are considered: for them, a dense continuous radio coverage is available. As seen in Figure B1, the KM3NeT event is relatively close to the Galactic plane (11°), at the edge of the CGRaBS coverage. Still, all bright (above 150 mJy) radio blazars within the neutrino localization region are covered by the OVRO monitoring program as seen from the lack of other radio sources from the RFC there. Combined OVRO + RATAN light curves are used, see Appendix A.1.2 and Appendix A.1.3 for details.

The aim of the statistical test is to evaluate two hypotheses:

1. Null hypothesis: The neutrino is unrelated to major blazar flares, either not connected to blazars entirely or not preferring times of major flares;
2. Alternative hypothesis: The neutrino arrival time is connected to a major radio flare.

Simulation: To compute the p-value, Monte Carlo simulations under the null hypothesis are used. In order to simulate the observations using minimal assumptions, $N = 3$ light curves for random blazars are selected from the full CGRaBS sample. This way, every realization represents the most conservative scenario where the number of coincident blazars is always equal to the observed one.

At each of 10^6 simulation steps, the following procedure is repeated:

1. Draw $N = 3$ random blazars from the CGRaBS sample;
2. Compute TS for their light curves according to the TS definition below.

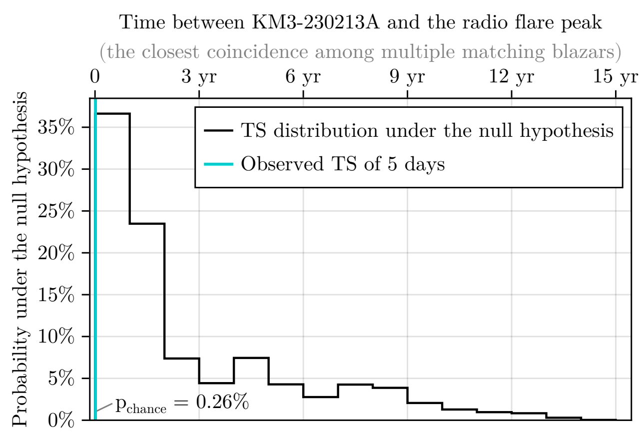

Figure B2. The illustration of the statistical test evaluating the temporal correlation between a radio flare and neutrino arrival for the PMN J0606-0724 blazar. As discussed in Section 5.1.2, it exhibits the strongest major flare exactly during the neutrino arrival time. The time delay between the neutrino and the flare peak is just 5 days, making the coincidence remarkable even given the 3° angular uncertainty of the neutrino event. Here, the observed value of the TS—the neutrino-radio flare delay—is shown in comparison with its distribution under the null hypothesis of no association.

In this procedure, the arrival time of the neutrino is fixed, and individual light curves are not modified in any way.

As a result, the distribution of the TS under the null hypothesis is obtained. Comparing the observed TS value with this distribution leads to the p-value.

TS. The TS adopted for the purpose of this test is the time difference between the neutrino arrival and the maximum in the radio light curve of a blazar. For multiple blazars, the shortest time difference is taken. Here, only the global all-time maximum of each light curve is considered. This is a conservative choice: there is always one flare selected for each blazar, and no minimum flux threshold. A corresponding benefit is that no free parameters need to be determined or set beforehand.

The full length of the available light curves, about 17 yr (Section A.1.2), is used for the TS calculation. It is to be noted that this approach makes the TS values dependent on the length of the radio monitoring program: the earlier the starting date, the more chances for the all-time maximum to coincide with more extreme historical flares instead of more recent ones closer to the neutrino arrival. This effect fundamentally influences both the observed and simulated coincidences in the same way, ensuring that the analysis is valid. A similar approach using the all-time normalized activity index was used for the same sample of blazars in P. M. Kouch et al. (2024). A potential alternative would be restricting the radio light curves to the operation time frame of KM3NeT. Such a restriction would involve more design choices, such as the proper accounting for the time-varying exposure of the detector. For the purpose of this work, a simple approach most similar to earlier studies was chosen in light of the a posteriori nature of the analysis.

The calculation of this TS goes as follows:

1. For a single blazar, TS_i = difference between the neutrino arrival time and the time of the maximum in the radio light curve;
2. for multiple blazars, $TS = \min(TS_i)$, where the index i runs over all the blazars.

Results: The performed analysis yields the following results:

1. Observed TS = 5 days, for the blazar PMN J0606-0724 (Figure 4(b));
2. The null distribution from the simulation is shown in Figure B2;
3. A p-value of $p = 0.26\%$ is obtained, indicating a 1 in 385 chance to observe a time difference of 5 days or less between the neutrino arrival time and the highest radio peak purely by random chance.

A discussion of the potential interpretation of this radio flare is given in Section 5.1.2. It should be noted that this analysis is fundamentally a posteriori and not trial-free; in particular, it focuses solely on flares in the radio band. The band choice is not completely arbitrary, but these considerations make determining the proper correction factor for the chance probability challenging, and this correction is not attempted here.

Appendix C
Multiwavelength Light Curves

In this section, the multiwavelength light curves for all sources listed in Table 3 are presented in Figures C1–C17.

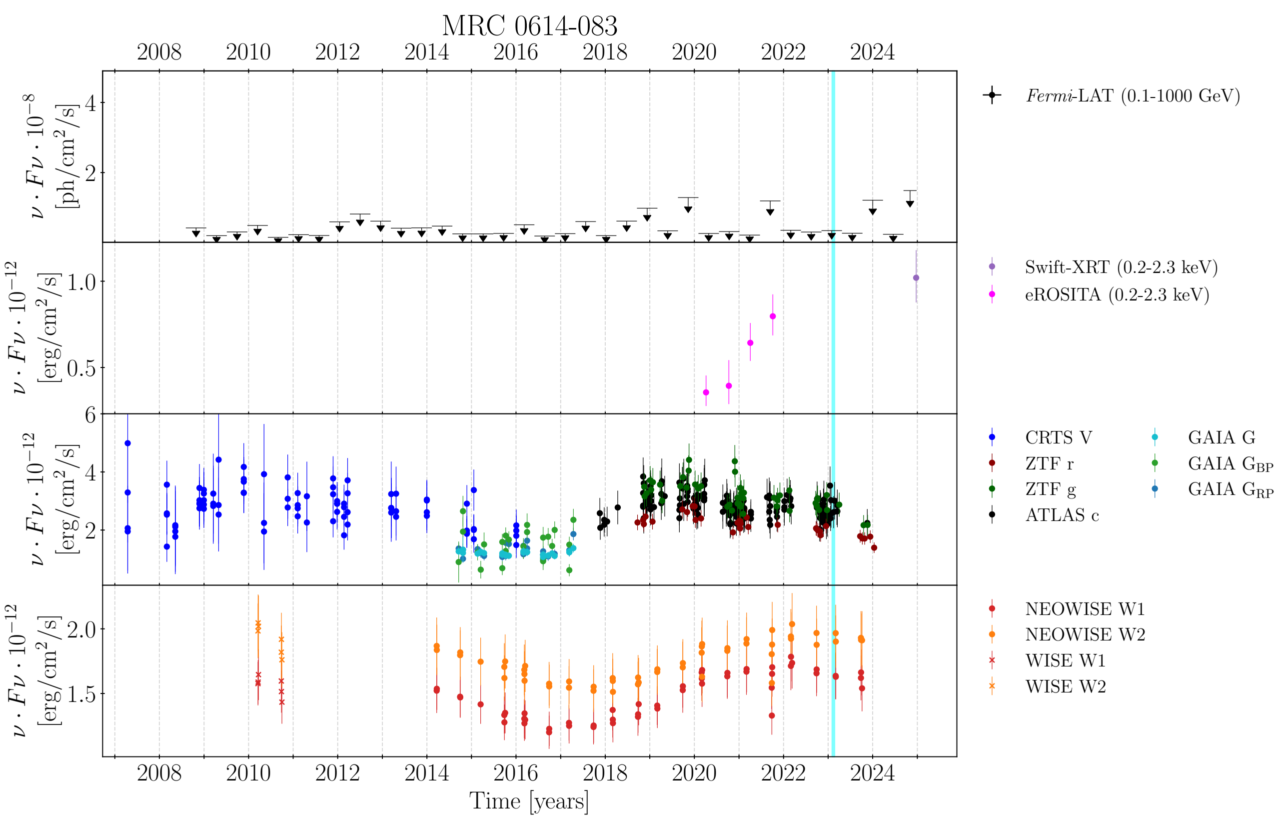

Figure C1. Multiwavelength light curves of MRC 0614-083 (#1). The panels display from top to bottom: Fermi-LAT gamma-ray light curves integrated over a 6 month time bin; X-ray data from Swift-XRT and eROSITA; optical data from CRTS, ZTF, ATLAS, and Gaia; IR data from WISE/NEOWISE. The cyan stripe highlights the arrival time of KM3-230213A.

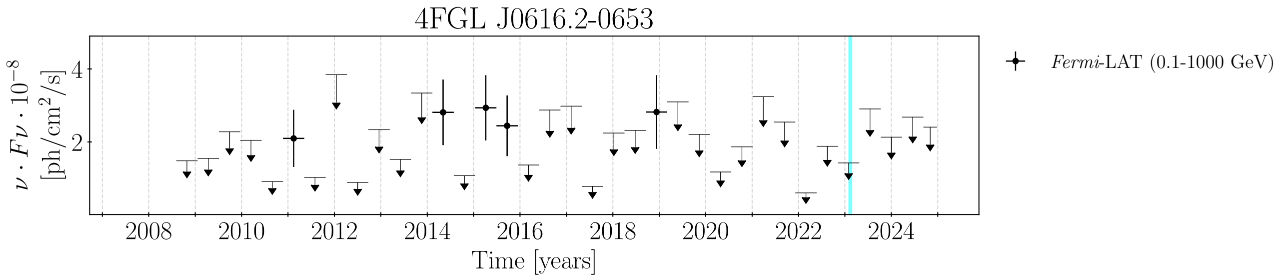

Figure C2. Fermi-LAT light curve of 4FGL J0616.2-0653 (#2), integrated over a 6 month time bin. The cyan stripe highlights the arrival time of KM3-230213A.

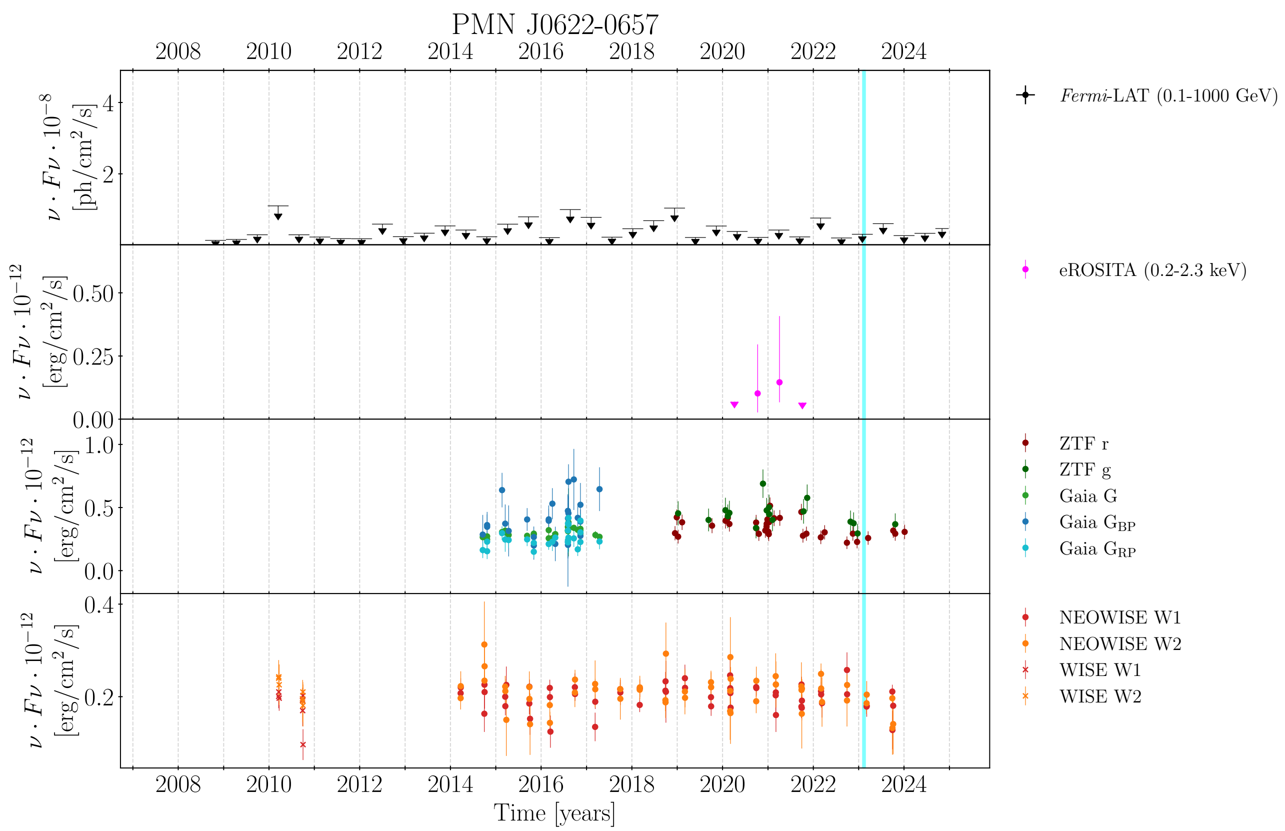

Figure C3. Multiwavelength light curves of PMN J0622-0657 (#3). The panels display from top to bottom: Fermi-LAT gamma-ray light curves integrated over 6 months; X-ray data from eROSITA; optical data from ZTF and Gaia; IR data from WISE/NEOWISE. The cyan stripe highlights the arrival time of KM3-230213A.

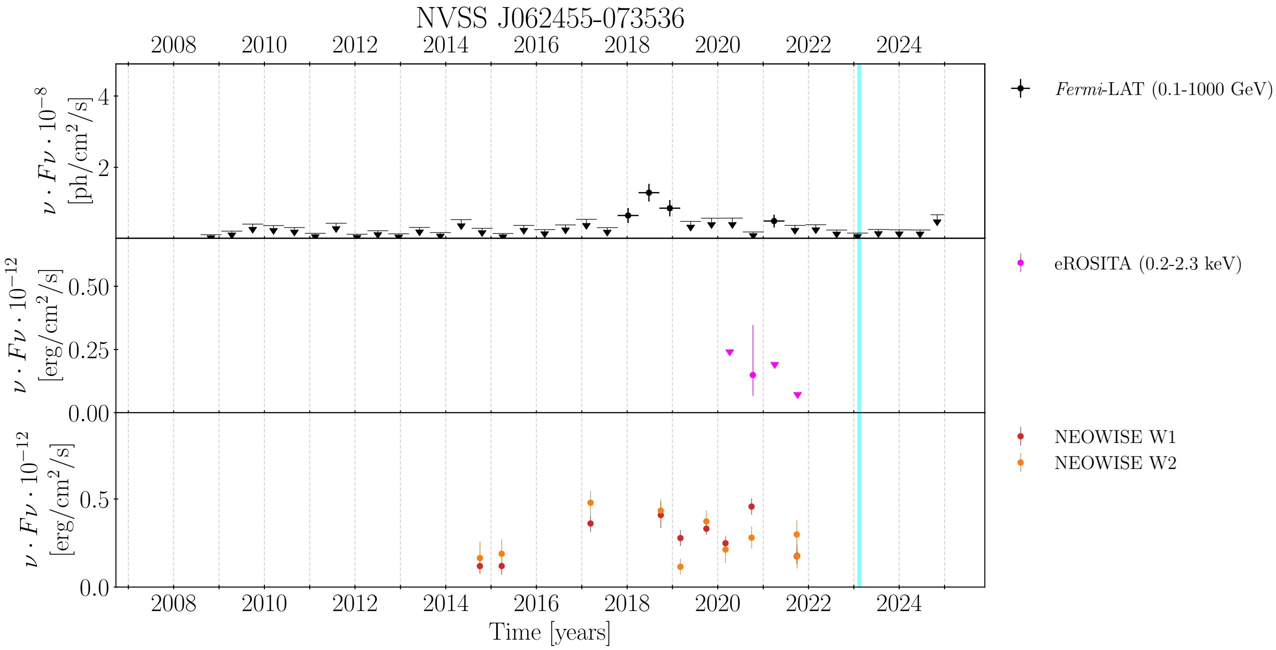

Figure C4. Multiwavelength light curves of NVSS J062455-073536 (#4). The panels display from top to bottom: Fermi-LAT gamma-ray light curves integrated over 6 months; X-ray data from eROSITA; IR data from WISE/NEOWISE. The cyan stripe highlights the arrival time of KM3-230213A.

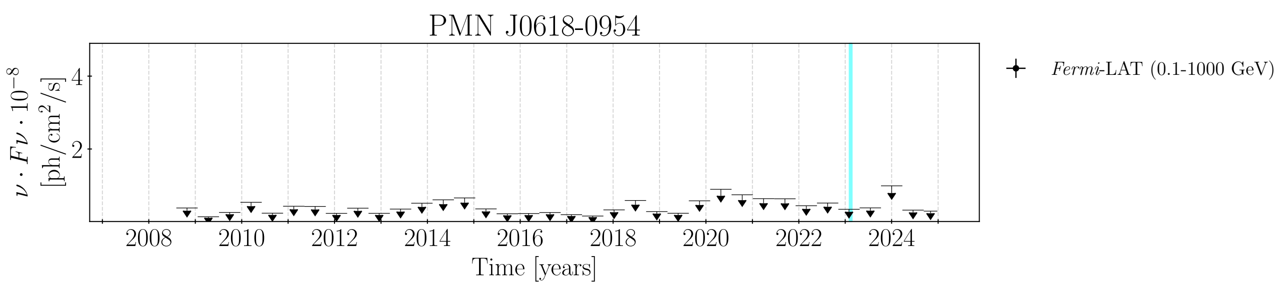

Figure C5. Fermi-LAT light curve of PMN J0618-0954 (#5), integrated over a 6 month time bin. The cyan stripe highlights the arrival time of KM3-230213A.

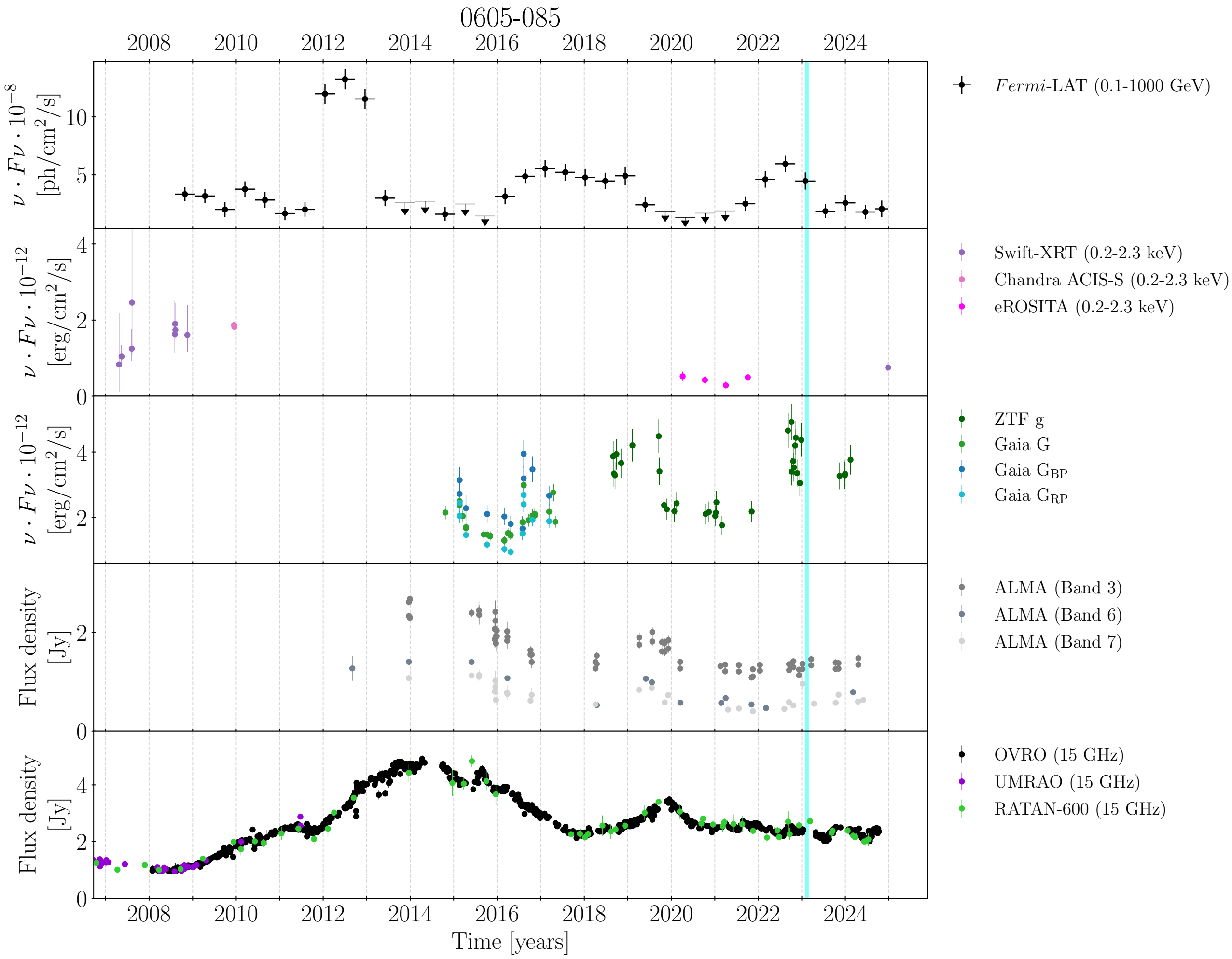

Figure C6. Multiwavelength light curves of 0605-085 (#6). The panels display from top to bottom: Fermi-LAT gamma-ray light curves integrated over 6 months; X-ray data from Swift-XRT, Chandra, and eROSITA; optical data from ZTF and Gaia; radio data from ALMA, OVRO, UMRAO, and RATAN-600. The cyan stripe highlights the arrival time of KM3-230213A.

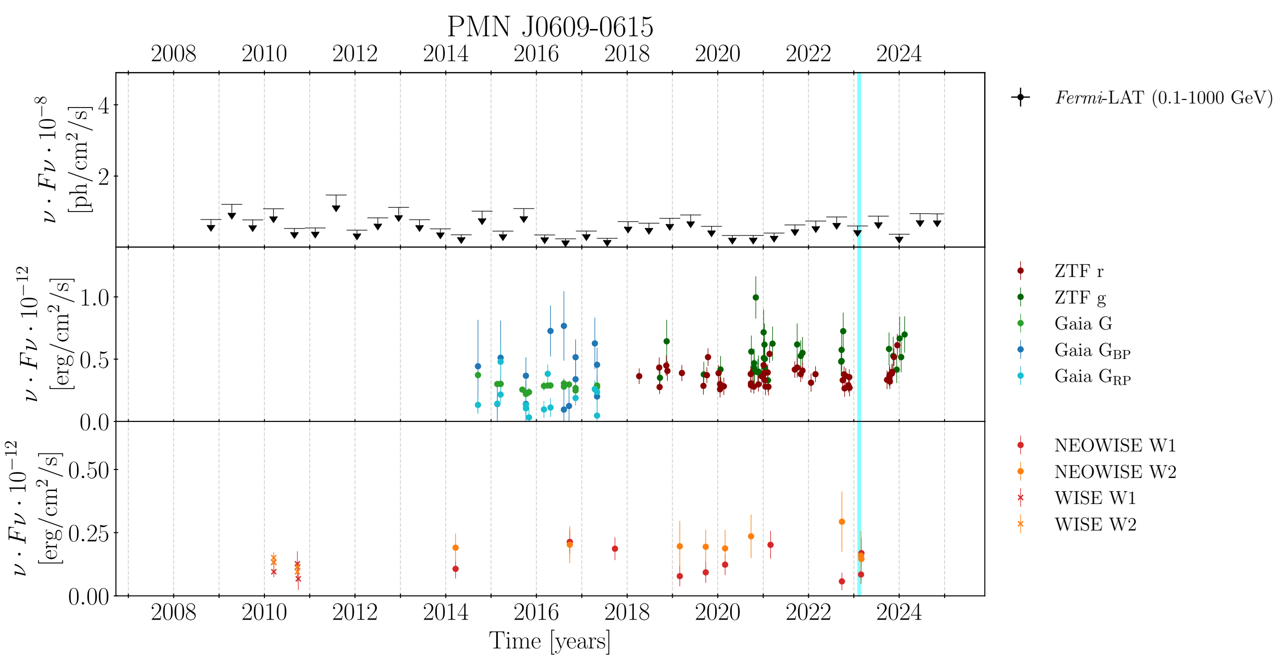

Figure C7. Multiwavelength light curves of PMN J0609-0615 (#7). The panels display from top to bottom: Fermi-LAT gamma-ray light curves integrated over 6 months; optical data from ZTF and Gaia; IR data from WISE/NEOWISE. The cyan stripe highlights the arrival time of KM3-230213A.

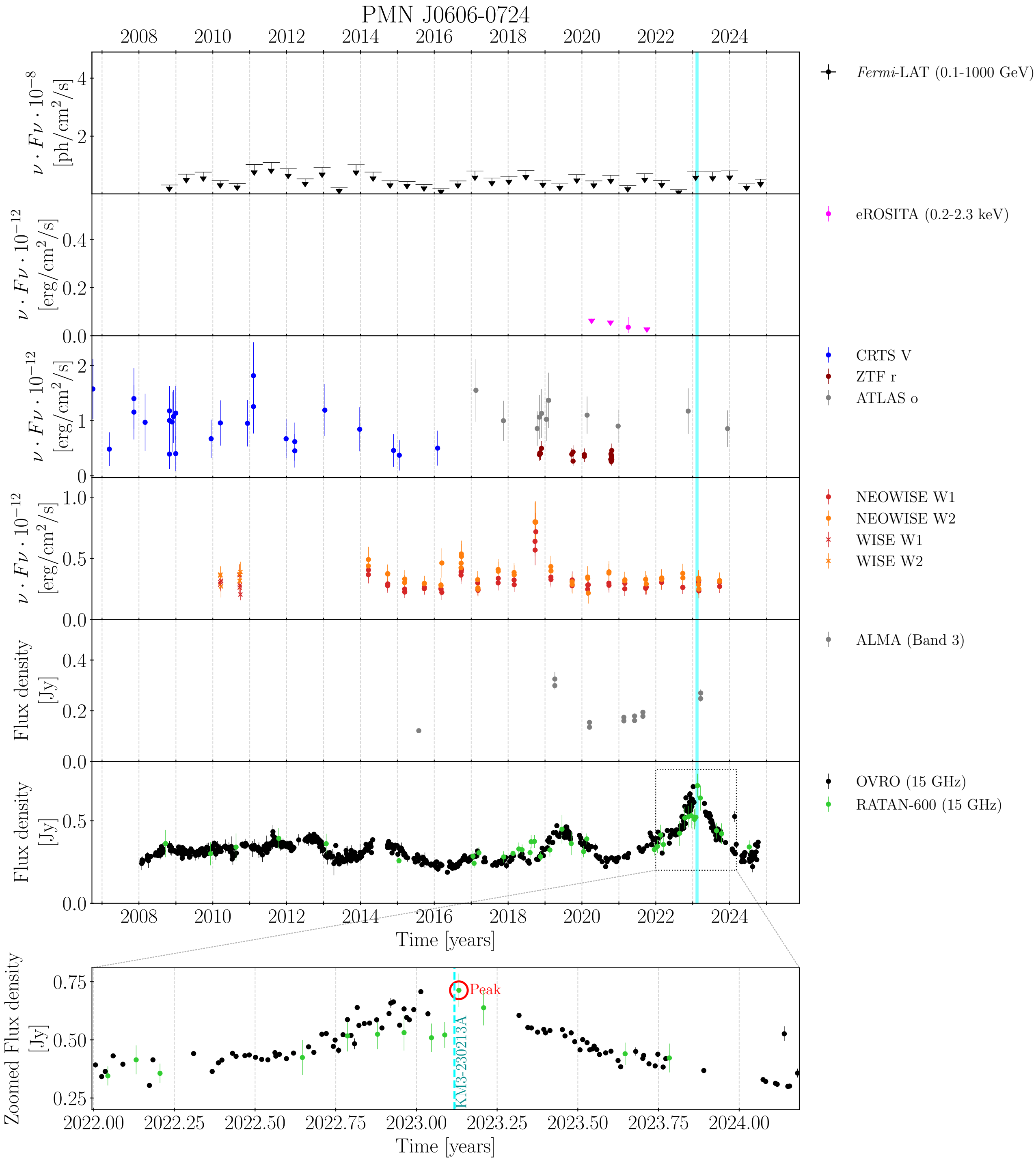

Figure C8. Multiwavelength light curves of PMN J0606-0724 (#8). The panels display from top to bottom: Fermi-LAT gamma-ray light curves integrated over 6 months; X-ray data from eROSITA; optical data from CRTS, ZTF, and ATLAS; IR data from WISE/NEOWISE; radio data from ALMA, OVRO, and RATAN-600. The last panel displays the zoomed radio light curve centered on the neutrino arrival time. The cyan stripe highlights the arrival time of KM3-230213A. The red circle indicates the all-time maximum peak of the radio light curve.

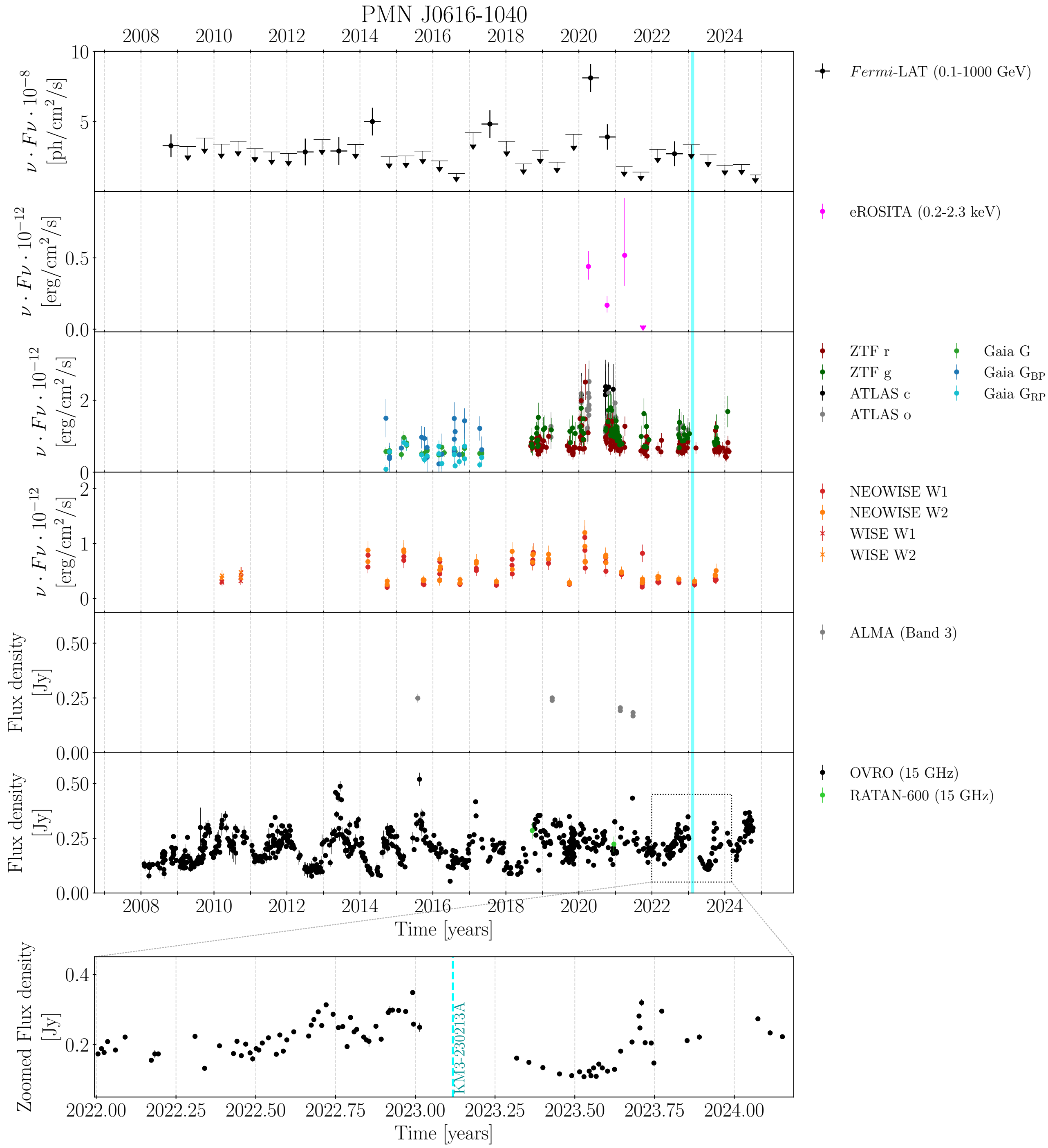

Figure C9. Multiwavelength light curves of PMN J0616-1040 (#9). The panels display from top to bottom: Fermi-LAT gamma-ray light curves integrated over 6 months; X-ray data from eROSITA; optical data from ZTF, ATLAS, and Gaia; IR data from WISE/NEOWISE; radio data from ALMA, OVRO, and RATAN-600. The last panel displays the zoomed radio light curve centered on the neutrino arrival time. The cyan stripe highlights the arrival time of KM3-230213A.

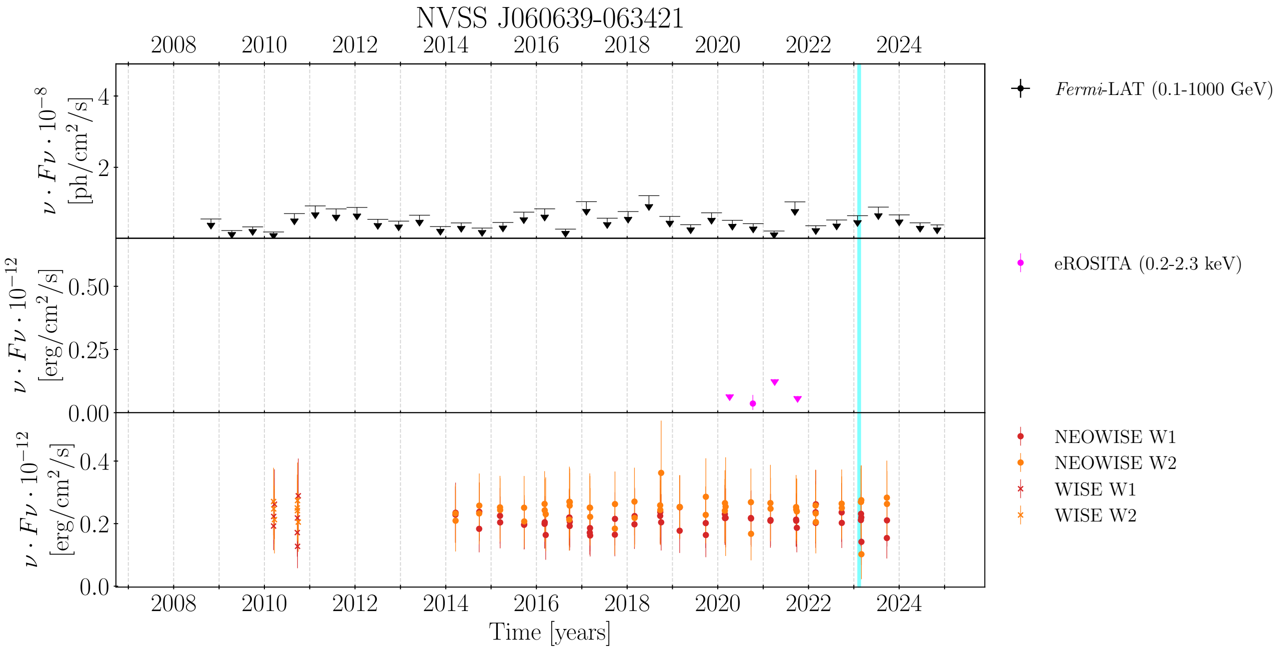

Figure C10. Multiwavelength light curves of NVSS J060639-063421 (#10). The panels display from top to bottom: Fermi-LAT gamma-ray light curves integrated over 6 months; X-ray data from eROSITA; IR data from WISE/NEOWISE. The cyan stripe highlights the arrival time of KM3-230213A.

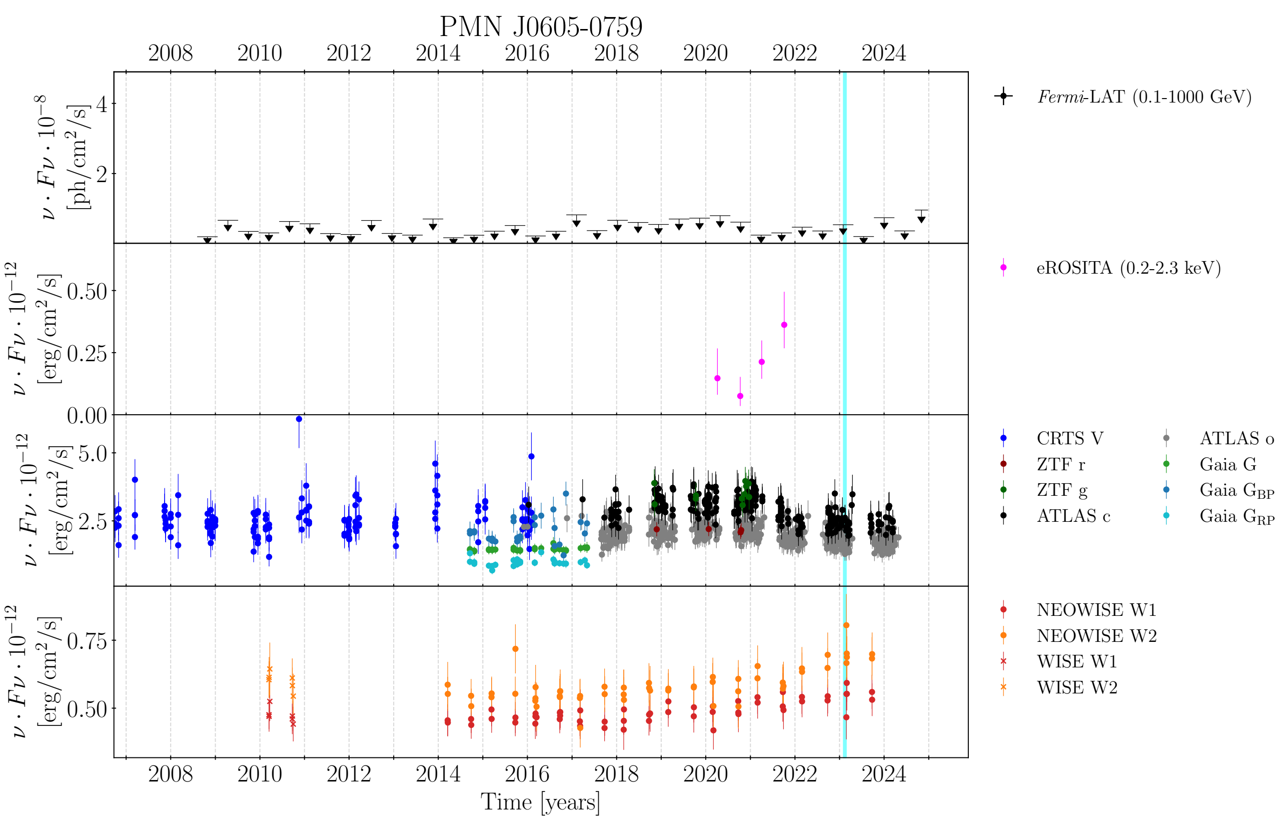

Figure C11. Multiwavelength light curves of PMN J0605-0759 (#11). The panels display from top to bottom: Fermi-LAT gamma-ray light curves integrated over 6 months; X-ray data from eROSITA; optical data from CRTS, ZTF, ATLAS, and Gaia; IR data from WISE/NEOWISE. The cyan stripe highlights the arrival time of KM3-230213A.

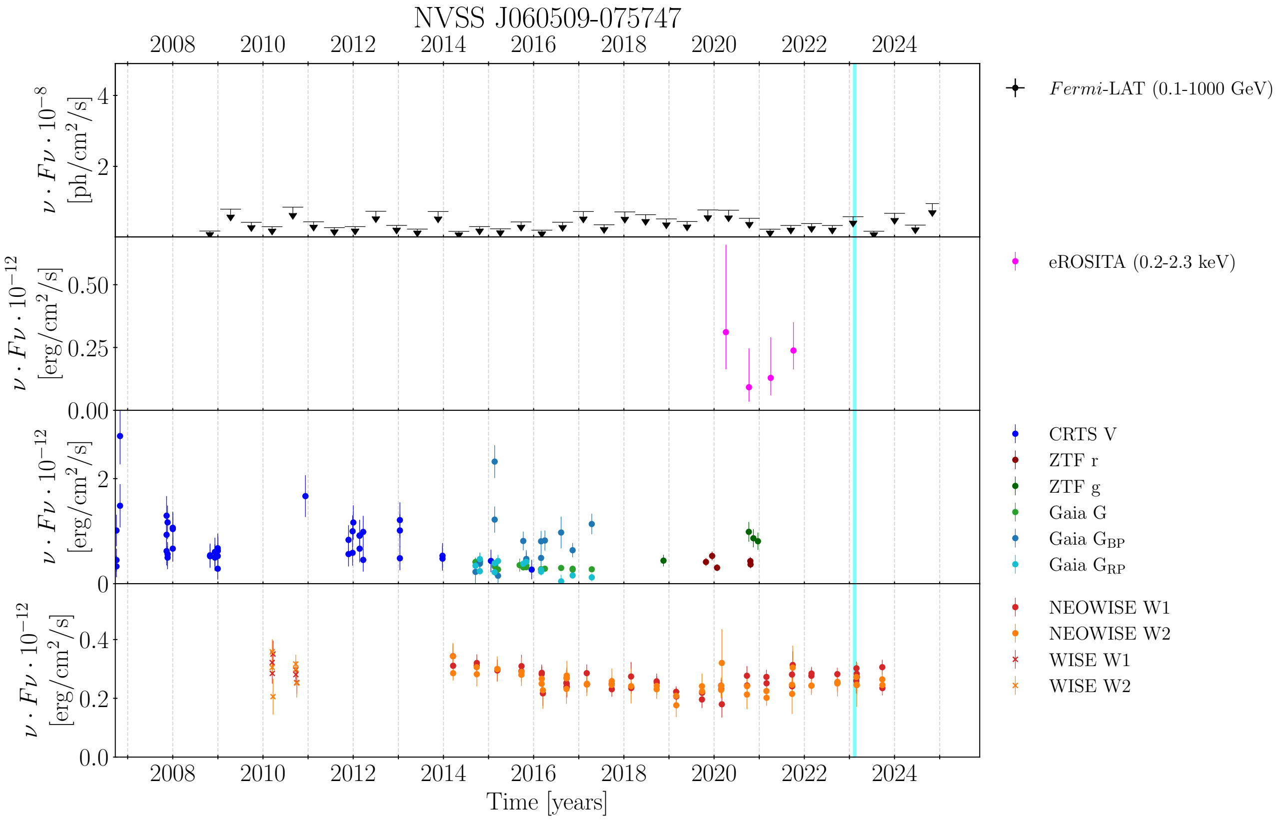

Figure C12. Multiwavelength light curves of NVSS J060509-075747 (#12). The panels display from top to bottom: Fermi-LAT gamma-ray light curves integrated over 6 months; X-ray data from eROSITA; optical data from CRTS, ZTF, and Gaia; IR data from WISE/NEOWISE. The cyan stripe highlights the arrival time of KM3-230213A.

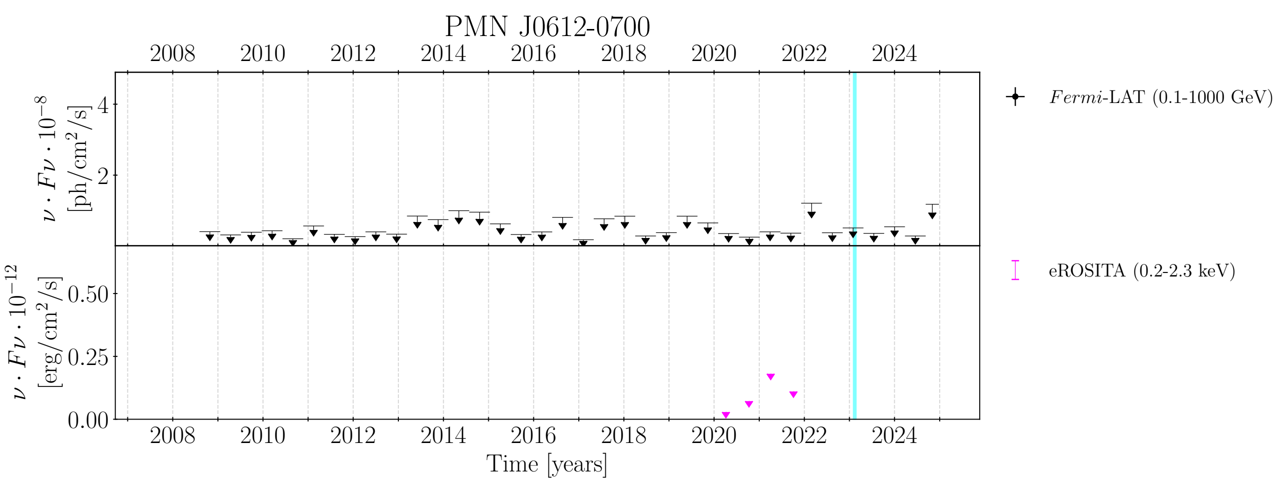

Figure C13. Multiwavelength light curves of PMN J0612-0700 (#13). The panels display from top to bottom: Fermi-LAT gamma-ray light curves integrated over 6 months; X-ray data from eROSITA. The cyan stripe highlights the arrival time of KM3-230213A.

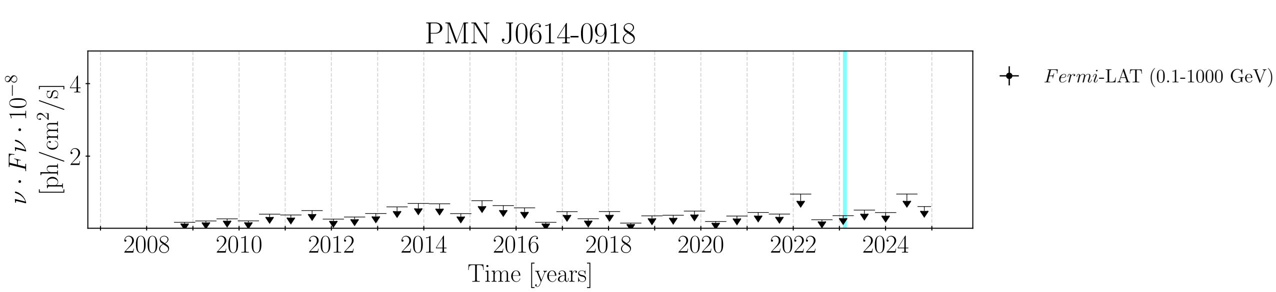

Figure C14. Fermi-LAT light curve of PMN J0614-0918 (#14), integrated over a 6 month time bin. The cyan stripe highlights the arrival time of KM3-230213A.

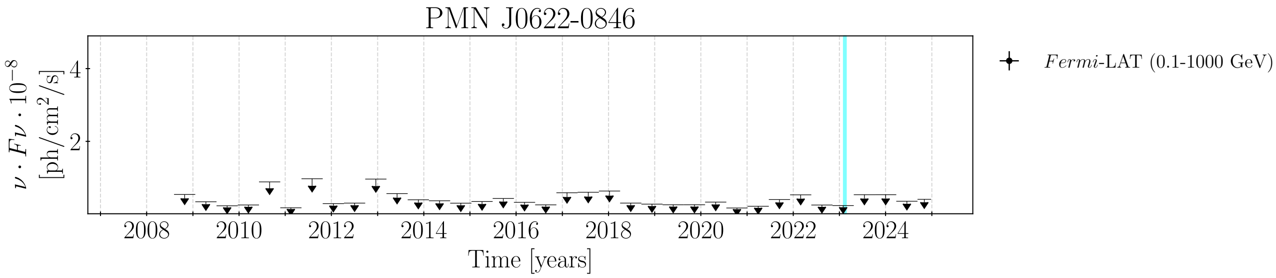

Figure C15. Fermi-LAT light curve of PMN J0622-0846 (#15), integrated over a 6 months time bin. The cyan stripe highlights the arrival time of KM3-230213A.

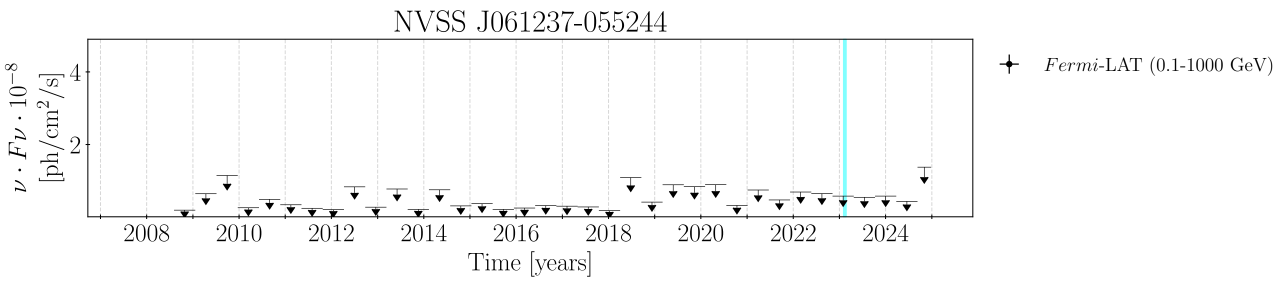

Figure C16. Fermi-LAT light curve of NVSS J061237-055244 (#16), integrated over a 6 month time bin. The cyan stripe highlights the arrival time of KM3-230213A.

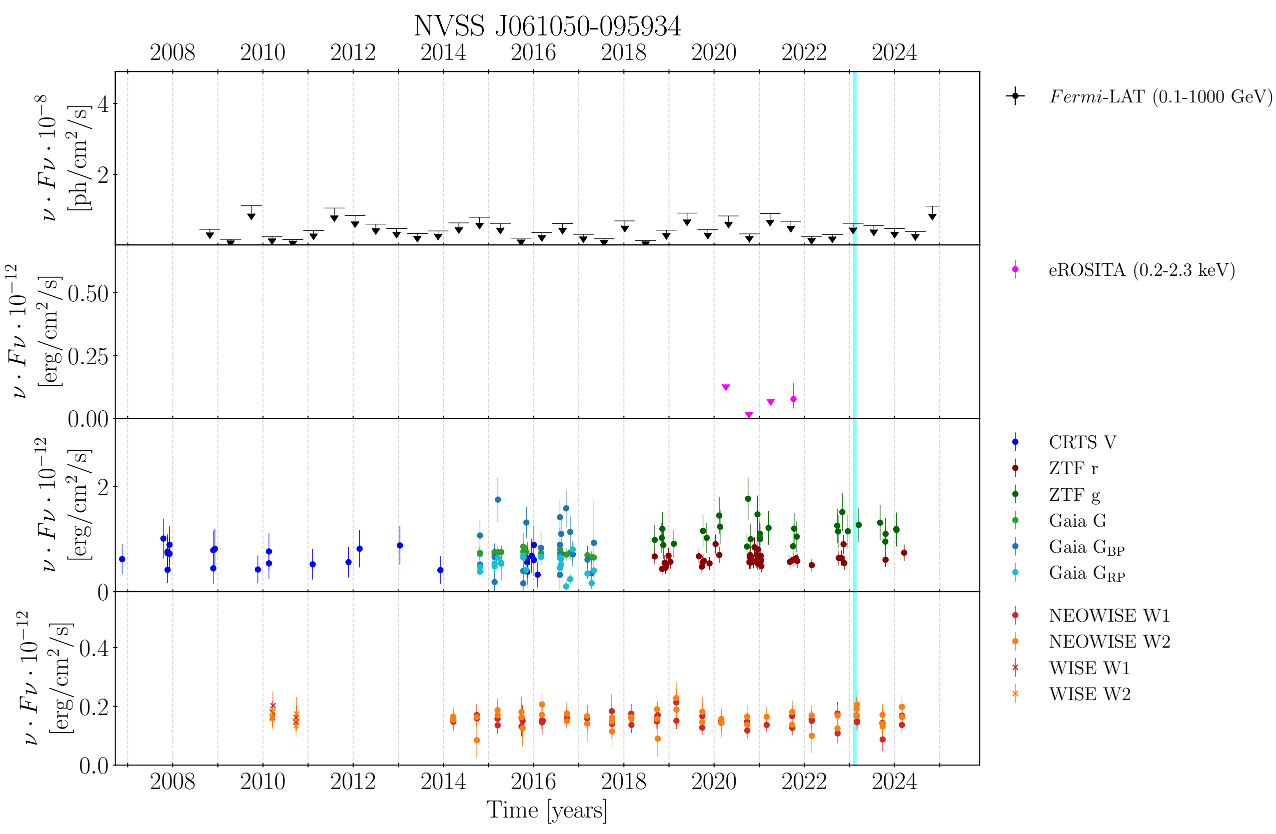

Figure C17. Multiwavelength light curves of NVSS J061050-095934 (#17). The panels display from top to bottom: Fermi-LAT gamma-ray light curves integrated over 6 months; X-ray data from eROSITA; optical data from CRTS, ZTF, and Gaia; IR data from WISE/NEOWISE. The cyan stripe highlights the arrival time of KM3-230213A.

ORCID iDs

M. Ardid https://orcid.org/0000-0002-3199-594X
M. Breuhaus https://orcid.org/0000-0003-0268-5122
S. Buson https://orcid.org/0000-0002-3308-324X
B. Guillon https://orcid.org/0000-0003-2622-0987
J. J. Hernández-Rey https://orcid.org/0000-0002-1527-7200
Yu. A. Kovalev https://orcid.org/0000-0002-8017-5665
Y. Y. Kovalev https://orcid.org/0000-0001-9303-3263
M. Lincetto https://orcid.org/0000-0002-1460-3369
L. Morales-Gallegos https://orcid.org/0000-0002-2241-4365
N. Mori https://orcid.org/0000-0003-2138-3787
S. Navas https://orcid.org/0000-0003-1688-5758
B. Ó Fearraigh https://orcid.org/0000-0002-1795-1617
L. Pfeiffer https://orcid.org/0000-0003-2497-6836
A. Plavin https://orcid.org/0000-0003-2914-8554
V. Popa https://orcid.org/0000-0001-6917-6600
E. Ros https://orcid.org/0000-0001-9503-4892
S. Sanfilippo https://orcid.org/0000-0001-5491-1705
M. Lincetto https://orcid.org/0000-0002-1460-3369
L. Pfeiffer https://orcid.org/0000-0003-2497-6836
S. Buson https://orcid.org/0000-0002-3308-324X
Jose Maria Sanchez Zaballa https://orcid.org/0009-0001-9486-1252
A. Azzollini https://orcid.org/0000-0002-2515-1353
A. Bremer https://orcid.org/0009-0002-6743-7808
A. Acharyya https://orcid.org/0000-0002-2028-9230
M. Ajello https://orcid.org/0000-0002-6584-1703
L. Baldini https://orcid.org/0000-0002-9785-7726
C. Bartolini https://orcid.org/0000-0001-7233-9546
J. Becerra Gonzalez https://orcid.org/0000-0002-6729-9022
R. Bellazzini https://orcid.org/0000-0002-2469-7063
E. Bissaldi https://orcid.org/0000-0001-9935-8106
R. D. Blandford https://orcid.org/0000-0002-1854-5506
R. Bonino https://orcid.org/0000-0002-4264-1215
P. Bruel https://orcid.org/0000-0002-9032-7941
R. A. Cameron https://orcid.org/0000-0003-0942-2747
R. Caputo https://orcid.org/0000-0002-9280-836X
P. A. Caraveo https://orcid.org/0000-0003-2478-8018
F. Casaburo https://orcid.org/0000-0002-2260-9322
E. Cavazzuti https://orcid.org/0000-0001-7150-9638
G. Chiaro https://orcid.org/0009-0004-4271-3153
N. Cibrario https://orcid.org/0000-0003-3842-4493
S. Ciprini https://orcid.org/0000-0002-0712-2479
G. Cozzolongo https://orcid.org/0009-0001-3324-0292
P. Cristarella Orestano https://orcid.org/0000-0003-3219-608X
S. Cutini https://orcid.org/0000-0002-1271-2924
F. D'Ammando https://orcid.org/0000-0001-7618-7527
N. Di Lalla https://orcid.org/0000-0002-7574-1298
L. Di Venere https://orcid.org/0000-0003-0703-824X
A. Domínguez https://orcid.org/0000-0002-3433-4610
S. J. Fegan https://orcid.org/0000-0002-9978-2510
A. Franckowiak https://orcid.org/0000-0002-5605-2219
Y. Fukazawa https://orcid.org/0000-0002-0921-8837
P. Fusco https://orcid.org/0000-0002-9383-2425
F. Gargano https://orcid.org/0000-0002-5055-6395
S. Garrappa https://orcid.org/0000-0003-2403-4582
C. Gasbarra https://orcid.org/0000-0001-8335-9614
D. Gasparrini https://orcid.org/0000-0002-5064-9495
S. Germani https://orcid.org/0000-0002-2233-6811
F. Giacchino https://orcid.org/0000-0002-0247-6884
N. Giglietto https://orcid.org/0000-0002-9021-2888
M. Giliberti https://orcid.org/0009-0007-2835-2963
F. Giordano https://orcid.org/0000-0002-8651-2394
M. Giroletti https://orcid.org/0000-0002-8657-8852
I. A. Grenier https://orcid.org/0000-0003-3274-674X
S. Guiriec https://orcid.org/0000-0001-5780-8770
R. Gupta https://orcid.org/0000-0003-4905-7801
M. Hashizume https://orcid.org/0009-0003-4534-9361
E. Hays https://orcid.org/0000-0002-8172-593X
J.W. Hewitt https://orcid.org/0000-0002-4064-6346
D. Horan https://orcid.org/0000-0001-5574-2579
X. Hou https://orcid.org/0000-0003-0933-6101
T. Kayanoki https://orcid.org/0000-0002-6960-9274
M. Kuss https://orcid.org/0000-0003-1212-9998
S. Larsson https://orcid.org/0000-0003-0716-107X
A. Laviron https://orcid.org/0000-0003-1521-7950
T. Lewis https://orcid.org/0000-0002-9854-1432
A. Liguori https://orcid.org/0009-0001-4240-6362
J. Li https://orcid.org/0000-0003-1720-9727
P. Loizzo https://orcid.org/0000-0002-2404-760X
F. Longo https://orcid.org/0000-0003-2501-2270
F. Loparco https://orcid.org/0000-0002-1173-5673
L. Lorusso https://orcid.org/0000-0002-2549-4401
M. N. Lovellette https://orcid.org/0000-0002-0332-5113
P. Lubrano https://orcid.org/0000-0003-0221-4806
S. Maldera https://orcid.org/0000-0002-0698-4421
D. Malyshev https://orcid.org/0000-0002-9102-4854
L. Marcotulli https://orcid.org/0000-0002-8472-3649
G. Martí-Devesa https://orcid.org/0000-0003-0766-6473
R. Martinelli https://orcid.org/0009-0004-0133-7227
M. N. Mazziotta https://orcid.org/0000-0001-9325-4672
I. Mereu https://orcid.org/0000-0003-0219-4534
M. Meyer https://orcid.org/0000-0002-0738-7581
M. Michailidis https://orcid.org/0009-0008-3653-1109
P. F. Michelson https://orcid.org/0000-0002-1321-5620
T. Mizuno https://orcid.org/0000-0001-7263-0296
P. Monti-Guarnieri https://orcid.org/0000-0002-1434-1282
M. E. Monzani https://orcid.org/0000-0002-8254-5308
A. Morselli https://orcid.org/0000-0002-7704-9553
I. V. Moskalenko https://orcid.org/0000-0001-6141-458X
M. Negro https://orcid.org/0000-0002-6548-5622
N. Omodei https://orcid.org/0000-0002-5448-7577
M. Orienti https://orcid.org/0000-0003-4470-7094
E. Orlando https://orcid.org/0000-0001-6406-9910
J. F. Ormes https://orcid.org/0000-0002-7220-6409
D. Paneque https://orcid.org/0000-0002-2830-0502
G. Panzarini https://orcid.org/0000-0002-2586-1021
M. Persic https://orcid.org/0000-0003-1853-4900
M. Pesce-Rollins https://orcid.org/0000-0003-1790-8018
L. Pfeiffer https://orcid.org/0000-0003-2497-6836
R. Pillera https://orcid.org/0000-0003-3808-963X
T. A. Porter https://orcid.org/0000-0002-2621-4440
G. Principe https://orcid.org/0000-0003-0406-7387
J. L. Racusin https://orcid.org/0000-0002-4744-9898
S. Rainò https://orcid.org/0000-0002-9181-0345
R. Rando https://orcid.org/0000-0001-6992-818X
B. Rani https://orcid.org/0000-0001-5711-084X
S. Rani https://orcid.org/0009-0009-6717-5706
M. Razzano https://orcid.org/0000-0003-4825-1629
A. Reimer https://orcid.org/0000-0001-8604-7077
O. Reimer https://orcid.org/0000-0001-6953-1385
M. Sánchez-Conde https://orcid.org/0000-0002-3849-9164
P. M. Saz Parkinson https://orcid.org/0000-0001-6566-1246

D. Serini https://orcid.org/0000-0002-9754-6530
C. Sgrò https://orcid.org/0000-0001-5676-6214
V. Sharma https://orcid.org/0000-0002-4394-4138
E. J. Siskind https://orcid.org/0000-0002-2872-2553
P. Spinelli https://orcid.org/0000-0001-6688-8864
D. J. Suson https://orcid.org/0000-0003-2911-2025
H. Tajima https://orcid.org/0000-0002-1721-7252
D. F. Torres https://orcid.org/0000-0002-1522-9065
J. Valverde https://orcid.org/0000-0002-8090-6528
K. Wood https://orcid.org/0000-0002-7376-3151
G. Zaharijas https://orcid.org/0000-0001-8484-7791
H. Zhang https://orcid.org/0000-0001-9826-1759
A. C. S. Readhead https://orcid.org/0000-0001-9152-961X
V. Pavlidou https://orcid.org/0000-0002-0870-1368
J. A. Zensus https://orcid.org/0000-0001-7470-3321
M.F. Aller https://orcid.org/0000-0003-2483-2103
P. V. de la Parra https://orcid.org/0000-0001-5957-1412
T. Hovatta https://orcid.org/0000-0002-2024-8199
S. Kiehlmann https://orcid.org/0000-0001-6314-9177
I. Liodakis https://orcid.org/0000-0001-9200-4006
W. Max-Moerbeck https://orcid.org/0000-0002-5491-5244
B. Molina https://orcid.org/0009-0000-9963-6874
T. J. Pearson https://orcid.org/0000-0001-5213-6231
V. Ravi https://orcid.org/0000-0002-7252-5485
R.A. Reeves https://orcid.org/0000-0001-5704-271X
A. Synani https://orcid.org/0009-0004-2614-830X
K. Tassis https://orcid.org/0000-0002-8831-2038
J. Buchner https://orcid.org/0000-0003-0426-6634
A. K. Erkenov https://orcid.org/0000-0002-0739-700X
N. Globus https://orcid.org/0000-0001-9011-0737
A. Merloni https://orcid.org/0000-0002-0761-0130
D. Porquet https://orcid.org/0000-0001-9731-0352
M. Salvato https://orcid.org/0000-0001-7116-9303
Y. V. Sotnikova https://orcid.org/0000-0001-9172-7237
P. A. Voitsik https://orcid.org/0000-0002-1290-1629Independent researcher.

References

Aartsen, M. G., Ackermann, M., Adams, J., et al. 2018, Sci, 361, 147
Abbasi, R., Ackermann, M., Adams, J., et al. 2022, ApJ, 928, 50
Abbasi, R., Ackermann, M., Adams, J., et al. 2023, ApJ, 954, 75
Abbasi, R., Ackermann, M., Adams, J., et al. 2025, ApJ, 981, 131
Abdollahi, S., Acero, F., Ackermann, M., et al. 2020, ApJS, 247, 33
Ackermann, M., Ajello, M., Allafort, A., et al. 2012, ApJ, 756, 4
Adrian-Martinez, S., Ageron, M., Aharonian, F., et al. 2016, JPhG, 43, 084001
Adriani, O., Albert, A., Alhebsi, A. R., et al. 2026, A&A, 710, A168
Adriani, O., Aiello, S., Albert, A., et al. 2025a, ApJL, 984, L41
Adriani, O., Aiello, S., Albert, A., et al. 2025b, CmPhy, 8, 457
Adriani, O., Albert, A., Alhebsi, A. R., et al. 2026a, ApJ, 1003, 157
Adriani, O., Alhebsi, A. R., Alshalloudi, S., et al. 2026b, JCAP, 2026, 033
Aiello, S., Albert, A., Alshamsi, M., et al. 2022, JINST, 17, P07038
Aiello, S., Albert, A., Alshamsi, M., et al. 2024, EPJC, 84, 885
Aiello, S., Albert, A., Alhebsi, A. R., et al. 2025a, Nature, 638, 376–382
Aiello, S., Albert, A., Alhebsi, A. R., et al. 2025b, JInst, 20, P07054
Albert, A., Alves, S., André, M., et al. 2024, ApJ, 964, 3
Aliakberov, K. D., Mingaliev, M. G., Naugolnaya, M. N., et al. 1985, AISAO, 19, 60
Allakhverdyan, V. A., Avrorin, A. D., Avrorin, A. V., et al. 2024, MNRAS, 527, 8784
Aller, H. D., Aller, M. F., Latimer, G. E., & Hodge, P. E. 1985, ApJS, 59, 513
Aller, M. F., Hughes, P. A., Aller, H. D., Latimer, G. E., & Hovatta, T. 2014, ApJ, 791, 53
Atwood, W., Albert, A., Baldini, L., et al. 2013, arXiv:1303.3514
Atwood, W. B., et al. 2009, ApJ, 697, 1071
Baars, J. W. M., Genzel, R., Pauliny-Toth, I. I. K., & Witzel, A. 1977, A&A, 500, 135
Babusiaux, C., Fabricius, C., Khanna, S., et al. 2023, A&A, 674, A32
Baldini, L., Ballet, J., Bastieri, D., et al. 2021, ApJS, 256, 13
Ballet, J., Bruel, P., Burnett, T. H., Lott, B. & The Fermi-LAT Collaboration 2023, arXiv:2307.12546
Bellenghi, C., Padovani, P., Resconi, E., & Giommi, P. 2023, ApJL, 955, L32
Berezinsky, V. S., & Zatsepin, G. T. 1969, PhLB, 28, 423
Bird, D. J., Corbato, S. C., Dai, H. Y., et al. 1995, ApJ, 441, 144
Blackburn, J. K. 1995, ASPC, 77, 367
Blandford, R., Meier, D., & Readhead, A. 2019, ARA&A, 57, 467
Blandford, R. D. 2000, PhST, 85, 191
Boller, T., Freyberg, M. J., Trümper, J., et al. 2016, A&A, 588, A103
Böttcher, M. 2019, Galax, 7, 20
Bruel, P., Burnett, T. H., Digel, S. W., et al. 2018, arXiv:1810.11394
Buchner, J. 2019, PASP, 131, 108005
Buchner, J. 2021, JOSS, 6, 3001
Buchner, J., Georgakakis, A., Nandra, K., et al. 2014, A&A, 564, A125
Burrows, D. N., Hill, J. E., Nousek, J. A., et al. 2005, SSRv, 120, 165
Buson, S., Tramacere, A., Pfeiffer, L., et al. 2022a, ApJL, 934, L38
Buson, S., et al. 2022b, ApJL, 933, L43
Buson, S., Tramacere, A., Oswald, L., et al. 2023, arXiv:2305.11263
Casandjian, J. M., & Grenier, I. A. 2008, A&A, 489, 849
Cash, W. 1979, ApJ, 228, 939
Chlebowski, T., Hughes, J. P., & Siemiginowska, A. 1991, PoAst, 39, 15
Condon, J. J., Cotton, W. D., Greisen, E. W., et al. 1998, AJ, 115, 1693
Cutri, R. M., Wright, E. L., Conrow, T., et al. 2021, yCat, II, 328
D'Abrusco, R., Massaro, F., Paggi, A., et al. 2014, ApJS, 215, 14
Das, S., Razzaque, S., & Gupta, N. 2022, A&A, 658, L6
Deller, A. T., Brisken, W. F., Phillips, C. J., et al. 2011, PASP, 123, 275
Dey, A., Schlegel, D. J., Lang, D., et al. 2019, AJ, 157, 168
Drake, A. J., Djorgovski, S. G., Mahabal, A., et al. 2009, ApJ, 696, 870
Fan, X., Zou, G., Wei, J., et al. 2020, SPIE, 11443, 114430Q
Fichet de Clairfontaine, G., Buson, S., Pfeiffer, L., et al. 2023, ApJL, 958, L2
Filipović, M. D., Smeaton, Z. J., Bradley, A. C., et al. 2025, ApJL, 984, L52
Fitzpatrick, E. L. 1999, PASP, 111, 63
Franckowiak, A., Garrappa, S., Paliya, V., et al. 2020, ApJ, 893, 162
Fruscione, A., McDowell, J. C., Allen, G. E., et al. 2006, SPIE, 6270, 62701V
Gaia Collaboration, Prusti, T., de Bruijne, J. H. J., et al. 2016, A&A, 595, A1
Gaia Collaboration, Vallenari, A., Brown, A. G. A., et al. 2023, A&A, 674, A1
Garrappa, S., Buson, S., Franckowiak, A., et al. 2019, ApJ, 880, 103
Garrappa, S., Buson, S., Sinapius, J., et al. 2024, A&A, 687, A59
Gehrels, N., Chincarini, G., Giommi, P., et al. 2004, ApJ, 611, 1005
Giommi, P., Glauch, T., Padovani, P., et al. 2020, MNRAS, 497, 865
Godet, O., Nasser, G., Atteia, J., et al. 2014, SPIE, 9144, 914424
Gottlieb, O., & Globus, N. 2021, ApJL, 915, L4
Götz, D., Boutelier, M., Burwitz, V., et al. 2023, ExA, 55, 487
Greisen, E. W. 2003, ASSL, 285, 109
Hartman, R. C., Bertsch, D. L., Bloom, S. D., et al. 1999, ApJS, 123, 79
Healey, S. E., Romani, R. W., Cotter, G., et al. 2008, ApJS, 175, 97
Heinze, A. N., Tonry, J. L., Denneau, L., et al. 2018, AJ, 156, 241
HI4PI Collaboration, Ben Bekhti, N., Flöer, L., et al. 2016, A&A, 594, A116
Hovatta, T., & Lindfors, E. 2019, NewAR, 87, 101541
Hovatta, T., Lindfors, E., Kiehlmann, S., et al. 2021, A&A, 650, A83
Janssen, M., Goddi, C., van Bemmel, I. M., et al. 2019, arXiv:1902.01749
Jarrett, T. H., Cohen, M., Masci, F., et al. 2011, ApJ, 735, 112
Jormanainen, J., Hovatta, T., Christie, I. M., et al. 2023, A&A, 678, A140
Kivokurtseva, P., & Troitsky, S. 2025, arXiv:2509.10352
KM3NeT Collaboration, Adriani, O., Aiello, S., et al. 2025, PhRvX, 15, 031016
Koay, J. Y., Jauncey, D. L., Hovatta, T., et al. 2019, MNRAS, 489, 5365
Kouch, P. M., Lindfors, E., Hovatta, T., et al. 2024, A&A, 690, A111
Kovalev, Y. Y., Nizhelsky, N. A., Kovalev, Y. A., et al. 1999, A&A, 139, 545
Kraft, R. P., Burrows, D. N., & Nousek, J. A. 1991, ApJ, 374, 344
Krauß, F., Kadler, M., Mannheim, K., et al. 2014, A&A, 566, L7
Kun, E., Bartos, I., Tjus, J. B., et al. 2024, PhRvD, 110, 123014
Lacy, M., Baum, S. A., Chandler, C. J., et al. 2020, PASP, 132, 035001
Lister, M. L., Aller, M. F., Aller, H. D., et al. 2018, ApJS, 234, 12
Lister, M. L., Homan, D. C., Hovatta, T., et al. 2019, ApJ, 874, 43
Mainzer, A., Bauer, J., Grav, T., et al. 2011, ApJ, 731, 53
Mannheim, K., & Biermann, P. L. 1989, A&A, 221, 211
Mannheim, K., Stanev, T., & Biermann, P. L. 1992, A&A, 260, L1
Masci, F. J., Laher, R. R., Rusholme, B., et al. 2018, PASP, 131, 018003
Massaro, E., Maselli, A., Leto, C., et al. 2015, Ap&SS, 357, 75
Massaro, F., D'Abrusco, R., Tosti, G., et al. 2012, ApJ, 750, 138
Mattox, J. R., Bertsch, D. L., Chiang, J., et al. 1996, ApJ, 461, 396
Merloni, A., Lamer, G., Liu, T., et al. 2024, A&A, 682, A34
Ott, M., Witzel, A., Quirrenbach, A., et al. 1994, A&A, 284, 331

Padovani, P., Oikonomou, F., Petropoulou, M., Giommi, P., & Resconi, E. 2019, MNRAS, 484, L104
Paliya, V. S., Böttcher, M., Olmo-García, A., et al. 2020, ApJ, 902, 29
Parijskij, Y. N. 1993, IAPM, 35, 7
Pearson, T. J., & Readhead, A. C. S. 1984, ARA&A, 22, 97
Perley, R. A., & Butler, B. J. 2013, ApJS, 204, 19
Perley, R. A., & Butler, B. J. 2017, ApJS, 230, 7
Petropoulou, M., Murase, K., Santander, M., et al. 2020, ApJ, 891, 115
Petrov, L., Kovalev, Y. Y., Fomalont, E. B., & Gordon, D. 2011, AJ, 142, 35
Petrov, L. Y., & Kovalev, Y. Y. 2025, ApJS, 276, 38
Plavin, A., Kovalev, Y. Y., Kovalev, Y. A., & Troitsky, S. 2020, ApJ, 894, 101
Plavin, A. V., Burenin, R. A., Kovalev, Y. Y., et al. 2024, JCAP, 2024, 133
Plavin, A. V., Kovalev, Y. Y., Kovalev, Y. A., & Troitsky, S. V. 2023, MNRAS, 523, 1799
Popkov, A. V., Kovalev, Y. Y., Petrov, L. Y., & Kovalev, Y. A. 2021, AJ, 161, 88
Predehl, P., Andritschke, R., Arefiev, V., et al. 2021, A&A, 647, A1
Readhead, A. C. S., Lawrence, C. R., Myers, S. T., et al. 1989, ApJ, 346, 566
Richards, J. L., Max-Moerbeck, W., Pavlidou, V., et al. 2011, ApJS, 194, 29
Rieger, F. M. 2022, Univ, 8, 607
Riello, M., De Angeli, F., Evans, D. W., et al. 2021, A&A, 649, A3
Rodrigo, C., & Solano, E. 2020, in XIV.0 Scientific Meeting (virtual) of the Spanish Astronomical Society, 182, (SEA) https://www.sea-astronomia.es/reunion-cientifica-2020
Rodrigo, C., Solano, E., & Bayo, A. 2012, SVO Filter Profile Service v1.0 1015, IVOA
Rodrigues, X., Rieger, F., Bohdan, A., & Padovani, P. 2026, A&A, 706, A351
Roulet, E., & Vissani, F. 2021, JCAP, 2021, 050
Salvato, M., Buchner, J., Budavari, T., et al. 2018, MNRAS, 473, 4937
Salvato, M., Wolf, J., Dwelly, T., et al. 2022, A&A, 661, A3
Schlafly, E. F., & Finkbeiner, D. P. 2011, ApJ, 737, 103
Schmitt, J. H. M. M., Fleming, T. A., & Giampapa, M. S. 1995, ApJ, 450, 392
Shaw, M. S., Romani, R. W., Cotter, G., et al. 2012, ApJ, 748, 49
Shepherd, M. C. 1997, ASPC, 125, 77
Sherman, A., Mirabal, N., Guevel, D., et al. 2026, ApJ, 1005, 194
Simmonds, C., Buchner, J., Salvato, M., Hsu, L. T., & Bauer, F. E. 2018, A&A, 618, A66
Smith, K. W., Smartt, S. J., Young, D. R., et al. 2020, PASP, 132, 085002
Sotnikova, Y. V. 2020, in Ground-Based Astronomy in Russia. 21st Century, Proc. of the All-Russian Conf., ed. I. I. Romanyuk et al. (SAO), 32
Spitzer Science Center (SSC)Infrared Science Archive (IRSA) 2021, yCat, II, 38
Sunyaev, R., Arefiev, V., Babyshkin, V., et al. 2021, A&A, 656, A132
Telescope Array Collaboration, Abbasi, R. U., Allen, M. G., et al. 2023, Sci, 382, 903
Tonry, J. L., Denneau, L., Heinze, A. N., et al. 2018, PASP, 130, 064505
Tsybulev, P. G. 2011, AstBu, 66, 109
Tsybulev, P. G., Nizhelskii, N. A., Dugin, M. V., et al. 2018, AstBu, 73, 494
Tubín-Arenas, D., Krumpe, M., Lamer, G., et al. 2024, A&A, 682, A35
Udovitskiy, R. Y., Sotnikova, Y. V., Mingaliev, M. G., et al. 2016, AstBu, 71, 496
Voges, W., Aschenbach, B., Boller, T., et al. 1999, A&A, 349, 389
Voges, W., Aschenbach, B., Boller, T., et al. 2000, IAU Circ. No., 7432, 3
Wei, J., Cordier, B., Antier, S., et al. 2016, arXiv:1610.06892
Weisskopf, M. C., Tananbaum, H. D., van Speybroeck, L. P., & O'Dell, S. L. 2000, SPIE, 4012, 2
White, N. E., Giommi, P., Angelini, L., et al. 2000, yCat, IX, 31
Winter, W., Gao, S., Rodrigues, X., et al. 2020, PoS, 358, 1032
Wood, M., Caputo, R., Charles, E., et al. 2017, ICRC, 301, 824
Wright, E. L., Eisenhardt, P. R. M., Mainzer, A. K., et al. 2010, AJ, 140, 1868
Yuan, C., Pfeiffer, L., Winter, W., et al. 2026, ApJL, 998, L1